Problem description

This project considers obstacle collision avoidance (COLAV) algorithms for two unmanned surface vessels (USVs) Odin and Frigg from The Norwegian Defence Research Establishment (Forsvarets Forskningsinstitutt - FFI). The problem is to develop a collision avoidance algorithm suited for formation driving of two USVs while dragging a mine sweep system after them. This would limit the maneuverability drastically in order for the sweeps not to be damaged. The algorithm should therefore be designed to be easy to integrate to a guidance scheme to combine the collision avoidance task with path following in formation driving. The USVs will be treated as if they were underactuated, such that surge and yaw will be controlled while we will not leverage the possibility to control the sway direction directly. The two following scenarios are of particular interest:

- COLREGs compliant collision avoidance where the USVs have a predetermined path that should be followed.
- Collision avoidance when the two USVs are driving in formation while dragging a mine sweep system. This limits the maneuverability of the vessels in order not to damage the sweep system.

This following tasks are suggested:

- Perform a literature study on collision avoidance and control of underactuated USVs.

- Do a qualitative evaluation of COLAV methods within the areas of usage of the USVs.
- Choose one collision avoidance algorithm and adapt it to the operational scenarios of interest.
- Implement and perform a simulation study of one COLAV method integrated with a formation control system
- Combine one COLAV method with a guidance scheme to obtain fully autonomous driving in simulations and full-scale experiments.

Abstract

This thesis considers obstacle collision avoidance for the two unmanned underactuated surface vessels (USVs) Frigg and Odin. The USVs are dragging a mine sweep system after themselves, which restricts the USVs to drive in a desired formation with maneuvering limitations. The constant avoidance angle method is chosen and extended with COLREGs compliance, closest point of approach based hysteresis and conversion of safety margins from heading space to absolute distances. The collision avoidance task is integrated into the null-space-based (NSB) behavioral control scheme by embedding it into a barycenter path following task. This task has the lowest priority after inter-vessel collision avoidance and formation tasks. The collision avoidance algorithm is calculated from the barycenter of the two USVs, and a new trajectory is generated to make the barycenter follow the constant avoidance angle when the collision avoidance mode is active. To account for maneuvering limitations, a fixed-radius inscribed circles approach is proposed in the trajectory generation to ensure that the USVs are able to track the reference path. This also ensures a smooth path and a continuous heading reference. A mathematical analysis is performed for one USV to guarantee collision avoidance with one obstacle. A simulation study with all the selected COLREGs scenarios is performed together with real-world experiments with the USVs to validate the method.

Sammendrag

Denne oppgaven omhandler kollisjonsunngåelse med hindringer for de to ubemannede underaktuerte overflatefartøyene (USV) Frigg og Odin. USV-ene drar et minesveipsystem etter seg, som begrenser USV-ene til å kjøre i en ønsket formasjon med manøvreringsbegrensninger. Metoden kalt konstant unngåelsesvinkel (CAA) er valgt og utvidet til å følge COLREGs, bruke en hysterese basert på nærmeste tilnærmingspunkt (CPA) og å konvertere sikkerhetsmargin fra heading-rom til absolutte distanser. Kollisjonsunngåelsesoppgaven er integrert i nullromsbasert (NSB) oppførselsstyring ved å legge det inn i en barysenter banefølgingsoppgave. Denne oppgaven har lavest prioritet etter oppgavene om kollisjonsunngåelse mellom fartøyene og formasjonskjøring. Kollisjonsunngåelsesalgoritmen er kalkulert fra barysenter av de to USV-ene, og en ny bane er generert for å få barysenter til å følge konstant unngåelsesvinkel når kollisjonsunngåelse er aktivert. Innskrevne sirkler med konstant radius i banegenereringen er foreslått for å ta høyde for manøvreringsbegrensninger, og for å sikre at USV-ene følger referansebanen. Dette sikrer også en glatt bane og en kontinuerlig heading-referanse. En matematisk analyse er gjort for én USV for å garantere kollisjonsunngåelse med én hindring. Et simulasjonsstudie med alle de valgte COLREGs-scenariene er gjennomført i tillegg til eksperimenter fra det virkelige systemet med USV-er for å validere metoden.

Contents

List of Figures

Preface

This master's thesis is submitted as a part of the requirements for the master degree at the Department of Engineering Cybernetics at the Norwegian University of Science and Technology. The work presented in this thesis has been carried out under the supervision of Prof. Kristin Y. Pettersen at the Department of Engineering Cybernetics, NTNU, and Else-Line Malene Ruud and Dr. Glenn Ivan Bitar, both from FFI.

This master's thesis is a continuation of a specialization project I conducted during the autumn of 2022. As is customary, the specialization project is not published. This means that important background theory and methods from the project report will be restated in full throughout this report to provide the best reading experience. All restated material has been revised and corrected when necessary. Below, a complete list of the material included from the specialization project is listed.

- Chapter 1 - Introduction (parts of section 1.1, 1.2 and 1.3)
- Chapter 2 - Literature review (all sections with modifications)
- Chapter 3 - Dynamic vessel modeling (specifically sections 3.1, and 3.3 with modifications and corrections)
- Chapter 4 - Control of the USV (specifically parts of section 4.1 and 4.3)
- Chapter 5 Collision avoidance: Constant avoidance angle (specifically sections 5.1, 5.2, 5.3 and 5.4 with modifications and corrections)

Unless otherwise stated, all figures and illustrations have been created by the author.

During the project, I have been provided simulation tools through Else-Line Malene Ruud, who gave me access to a Python wrapped C++ simulator of the USV from FFI. There, I implemented a complete collision avoidance algorithm in order to control the USV from static and dynamic obstacles, where COLREGs are considered for the dynamic obstacles. Furthermore, this is extended to barycenter collision avoidance by integrating it to the path following task in the null-space-based behavioral control scheme. Heading, surge and yaw rate controllers for the USV were also implemented. Furthermore, I have been provided a high-fidelity ROS simulator through FFI, where the mentioned control scheme was implemented. This was also made to prepare for experiments on the real USVs at the FFI test station in Horten.

I would like to thank Prof. Kristin Y. Pettersen, Else-Line Malene Ruud and Dr. Glenn Ivan Bitar for help and supervision. In particular, I would like to express my appreciation to Ruud for a thorough revision of the whole thesis. I would also like to thank Jarle Sandrib and Marius Rundhovde for their valuable contributions in planning and completing the experiments in Horten. Finally, a special thanks to PhD candidates Bjørn Kåre Sæbø and Markus Iversflaten for useful curricular discussions and guidance throughout the project.

Harald Minde Hansen
Trondheim, June 2023

List of Acronyms

APF Artificial Potential Field

CAA Constant Avoidance Angle

CBF Control Barrirer Functions

CC Collision Cone

CLIK Closed Loop Inverse Kinematics

COLAV Collision Avoidance

COLREG Convention on the International Regulations for Preventing Collisions at Sea

CPA Closest Point of Approach

DOF Degrees of Freedom

DW Dynamic Window

FFI Norwegian Defence Research Establishment (Forsvarets Forskningsinstitutt)

GPS Global Positioning System

IMU Inertial Measurement Unit

LOS Line-of-Sight

MPC Model Predictive Control

NED North-East-Down

NSB Null-space-based

PD Proportional Derivative

PID Proportional Integral Derivative

ROS Robot Operating System

RPM Revolutions Per Minute

UGAS Uniformly Global Asymptotically Stable

UGES Uniformly Global Exponential Stable

USGES Uniformly Semi-Global Exponential Stable

USV Underactuated Surface Vessel

VO Velocity obstacles

Chapter 1

Introduction

This chapter will motivate the project and explain the high level control hierarchy of each vessel. The first part of Section 1.1 is taken from the specialization project. Section 1.2 is also based on the specialization project, but modified to concern two vessels driving in formation. Section 1.3 will present some assumptions, which are unchanged from the specialization project. Finally, contributions of the project will be presented in Section 1.4 before the outline of the report is listed in Section 1.5.

1.1 Motivation

Marine navigation has been of significant importance for centuries in order to explore and commute between different parts of the world. Navigation performed by human beings is complicated and requires a deep understanding of behavior and interaction with other marine vehicles as well as experience with operating marine vehicles. As history has proven, accidents are inevitable when human operators are required to cooperate and obey with rules and regulations at sea. A recent example in Norway is the collision of Helge Ingstad with the tanker Sola TS (see (VG: Einar Otto Stangvik, Oda Leraan Skjetne, Tom Byermoen, Endre Alsaker-Nøstdahl, Harald Vikøyr; 2022)), which motivates the potential reward in assisting the error prone human operator. With the

Figure 1.1: Odin and Frigg. Courtesy of FFI.

increasing focus on autonomy for vehicles, reliable collision avoidance systems would be the crucial.

The usage of sea mines directed against military objectives is not prohibited according to the last updated commentary of the Geneva Convention in ICRC (2016). Additionally, increased commercial traffic at sea in combination with a reduced number of military vessels provided by NATO and EU has motivated The Norwegian Defence Research Establishment (FFI) to do research on unmanned systems for stand off underwater mine hunting as described in (Midtgaard, Øivind and Nakjem, Morten; 2016). Operating in areas where sea mines might be located would imply a risk for human life. Hence, the usage of unmanned surface vessels is considered to be of significant importance in the future naval mine countermeasures capabilities of the Royal Norwegian Navy, removing personnel from the mine danger area. Investments on this technology has recently been made, e.g. the autonomous underwater vehicles Hugin by Forsvarsmateriell (2017). Other examples are the mine sweep tests performed

by FFI (2020) and the investments in the Patria Sonac ACS acoustic mine sweeping systems mentioned in Naval News Staff (2021). Extensive work on unmanned and autonomous mine sweeping has also been made by the Royal Navy in the UK (Royal Navy (2021)). With the ongoing threat against NATO and EU during the Russian invasion of Ukraine, preparations for this type of warfare could potentially be crucial for the Western society. For the unmanned surface vehicles to operate autonomously, a collision avoidance algorithm is necessary for ensuring safe operations.

Odin and Frigg (Figure 1.1) are two 10.5 meters long surface vessels used for research and development by FFI. These investments were made to demonstrate and test the performance of technology in the maritime mine countermeasures. They are driven by a dual Hamilton jet system for actuation. These jets are linked together for each vessels in this project for a simpler and more energy efficient maneuvering interface. Thus, actuation works only for thrust and nozzle angle for the motor. With a 3 degrees of freedom (3-DOF) model for the vessels, they are underactuated due to the lack of direct control force in the sideways direction of the water jets. The vessels are equipped with sensors to facilitate fully autonomous driving. This enables them to be unmanned for potential future mine sweeping operations.

The maritime mine countermeasures consists of a closed-loop mine sweep system which is to be dragged behind the two USVs while driving in formation. For this reason, the USVs are required to keep a desired formation autonomously in order not to damage the sweep system. Contributions to this topic have been made in the implementation of the null-space-based behavioral control scheme Eek et al. (2020), where the USVs could combine the tasks inter-vessel collision avoidance, formation driving and path following in a hierarchical task priority system. However, this was in the absence of obstacles and only included inter-vessel collision avoidance. Arrichiello et al. (2006) included collision avoidance with obstacles as a dedicated task in the control scheme. Each obstacle got assigned a weight representing their priority based on distance from the barycenter and whether the obstacles were dynamic. This weighting was tuned numerically without any mathematical foundation. Thus, the scheme would be too simple to obtain safe interaction with other boats at sea. Hence, a thorough collision avoidance integration to a hierarchical task control scheme for surface vessels would

contribute developing the topic of autonomous formation driving further.

The objective of this project is to develop a well suited collision avoidance algorithm to be implemented into a control scheme to ensure autonomous formation driving of two USVs while following a predefined path in the presence of obstacles.

1.2 High level control architecture

An autonomous system typically consists of several modules of sensors, models and controllers coupled together. Figure 1.2 shows an overview of the system architecture that is implemented in this project. This ties together all the parts which will be introduced in the subsequent chapters. At each time step, the full state of both USVs is fed into the control scheme of our choice together with the velocity and position of all obstacles nearby. We will use the null-space based (NSB) behavioral scheme studied in (Eek et al.; 2020), (Matouš et al.; 2021) and (Matouš et al.; 2023). Here, the USVs will drive in formation along a predefined path. If the vehicle is on collision course with some obstacle and the distance between them is sufficiently small, the collision avoidance mode will be activated. The collision avoidance algorithm will output a desired heading for the USVs to follow. This will overwrite the original path until obstacles are out of collision danger. To generate a continuous trajectory for tracking, the desired heading will pass through a reference model. Then, the continuous desired heading signal will be the input of a heading controller. This will output a desired yaw rate for the USV, which can be controlled. The desired yaw rate and the desired surge from the NSB framework are passed through the velocity reference model to provide a continuous, piecewise smooth trajectory of the desired surge and yaw rate. These signals are fed into a PD or PID controller, such that desired force and torque are provided for surge and yaw, respectively. Now, the force and torque need to be converted to throttle and steering demands within the actuator limits of the water jet motors of the USVs. Finally, these demands are sent to the water jet motor. This will in turn affect the dynamics of the USV in the next time step.

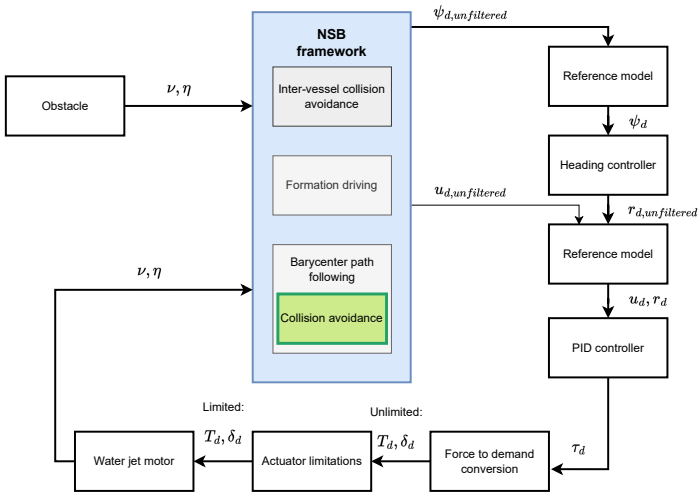

Figure 1.2: High level control architecture.

1.3 Assumptions

For this project, we will use the following general assumptions. Other assumptions will be stated when they are revelant.

Assumption 1.1: Measurements of the vehicles and obstacle states are perfect, and without any bias or noise.

Remark: This is a rather unrealistic assumption as there is no such thing as a perfect measurement. That being said, the situational awareness module that is part of FFIs autonomy software on Odin and Frigg provides a satisfactory representation of the environment, based on radar and lidar measurements of obstacles as well as IMU and GPS for vehicle state determination. Moreover, having a fully deterministic model simplifies all calculations drastically. The focus of the project is not on the measurements, but rather on the planning and control of the vehicle. Considerations around measurements are therefore left as a possible extension to the project in the future.

Assumption 1.2: Motion is restricted to three degrees of freedom (3-DOF) in the horizontal water plane.

Remark: This is a common simplification for surface vehicles (Fossen (2011)). All perturbations in roll, pitch and heave of the vehicles are assumed to be negligible as they will remain small during normal operation of the vehicles.
Assumption 1.3: No obstacles or other vehicles are close to the USVs during initialization.
Remark: This is a necessary assumption to prevent unavoidable collisions when leaving the control from a human operator.

1.4 Contributions

The main contributions of the work presented in this report are as follows:

- Literature study of some well known collision avoidance algorithms with considerations around the best suited algorithms for our particular vehicles, scenario and requirements.
- Integration of the constant avoidance angle algorithm into the null-space-based behavioral control scheme for two USVs driving in formation.
- Further development of the algorithm presented in (Wiig et al.; 2020) ensuring COLREGs compliance during encounters with one obstacle.
- A simulation study evaluating the performance of the proposed algorithm in scenarios with dynamic and uncooperative obstacles.
- Full-scale experiments of the collision avoidance algorithm with dynamic obstacles.
- Mathematical analysis of the collision avoidance task for two USVs.

1.5 Outline

The report is organized as follows. In Chapter 2 we will present and compare some well known collision avoidance algorithms. In Chapter 3 a mathematical model is

presented to describe the USV, water jet and obstacle dynamics. In Chapter 4 we present necessary controllers for fully autonomous operation of the USV given heading and surge references from a control scheme. In Chapter 5 we present the constant avoidance algorithm together with our extensions. The NSB control scheme is presented in Chapter 6 together with our integration suggestion of the collision avoidance algorithm. A simulation study of our solution is presented in Chapter 8 before experimental results of testing on the real USVs are presented in Chapter 9. Mathematical analysis of the collision avoidance task is performed in Chapter 7. The conclusion and suggestions for further work are presented in Chapter 10.

Chapter 2

Literature review

Collision avoidance algorithms are often split into two groups: Reactive and deliberate algorithms, where the latter is also known as motion planning. Motion planning typically plans for a longer time horizon, providing a full reference trajectory for the controllers. This would normally result in more optimal choices, though at a higher computational cost than the reactive algorithms, especially for more complex and dense environments. The reactive algorithms are characterized by optimizing based on information over a shorter time span. This implies finding local minimums and therefore often a suboptimal solution for the collision avoidance. Also, the short time frame could cause the trajectory of a vehicle to become non-smooth as many optimization problems over short time spans are solved frequently. Despite these drawbacks, reactive algorithms are widely used due to their low computational cost. They are also able to react to sudden changes in the environment, such as rapid unexpected turns from other boats or late detection of obstacles. Hence, they would serve well as a redundancy for a high level motion planning algorithms when the optimization problems become sufficiently complex.

Implementations of the most popular algorithms could contain some type of planning, and one could therefore argue that the distinction between deliberate and reactive algorithms is of less importance. A more precise distinction between the algorithms

could be short term and long term, where the collision avoidance algorithm is classified based on the time horizon. A combination could consist of a planning algorithm as the default to follow, while a short term collision avoidance algorithm will be applied whenever needed. That is, when the vehicle is sufficiently close and on collision course with some obstacle. Otherwise, the collision avoidance control law would be disabled.

In this chapter, a selection of the most popular collision avoidance algorithms will be discussed and compared. Reactive algorithms are given most attention, as they provide more flexibility for combination with guidance laws. In this project, the term obstacles would be used as a generic term describing all objects which we cannot control, but would have to keep away from in order to avoid collisions. This means that other surface vehicles, land and objects at sea will all be referred to as obstacles, regardless of their dynamics. The vehicle we are operating will be referred to as the USV or vehicle. The chapter is taken from the specialization project with some modifications.

2.1 Vision cone approaches

2.1.1 Collision cone and velocity obstacles

Velocity obstacles (VO, (Fiorini and Shiller; 1998)) and the collision cone concept (CC, (Chakravarthy and Ghose; 1998)) are widely used reactive algorithms, leveraging the so-called vision cone from the driver's perspective. Both of them define a cone from the vehicle to a circle around the obstacle indicating courses the vehicle should avoid to prevent collisions. The main difference between the two algorithms is that the velocity obstacles algorithm operates in the velocity space such that the relative velocity between the vehicle and the obstacle is accounted for. However, it is straightforward to add compensation to the collision cone by the addition of extra angles, such that the collision cone and the velocity obstacles approaches are conceptually very similar.

Each cone corresponding to an obstacle has its geometrical top at the origin of the vehicle's body coordinate frame and tangents the obstacle's extremes on each side. In other words, the cone tangents the points from the obstacle's center which are farthest

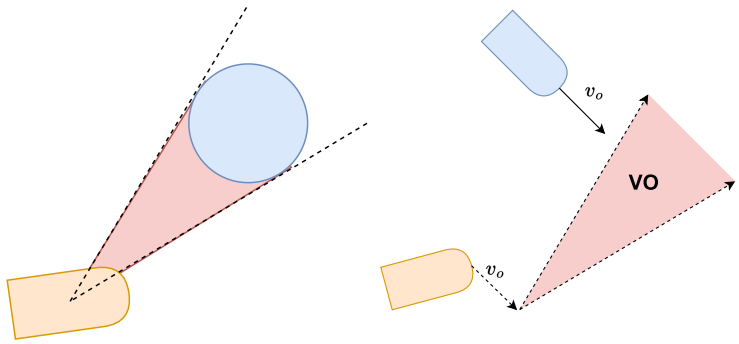

(a) Collision cone (CC) (b) Velocity obstacles (VO)

Figure 2.1: The orange objects represent the USVs while the blue objects are the obstacles. The red spaces define the set of velocities which would cause a collision.

away but still define a collision if a part of the vehicle would coincide with this point. See Figure 2.1 for a graphical illustration. The course rate reference is set to lead the vehicle outside of the cone such that a collision is prevented for both the velocity obstacles and the collision cone.

The collision cone approach, first suggested in (Chakravarthy and Ghose; 1998), starts with the collision cone and adds an additional angle on each side of the cone which compensates for the relative velocity between the vehicle and the obstacle. For this reason, the collision cone representation with relative velocity compensation between the vehicle and the obstacle has a similar nature to velocity obstacles. For USVs, (Haraldsen et al.; 2021) managed to mathematically guarantee collision avoidance with one obstacle. This was done by adding an extra safety angle on the extended cone to account for unexpected turns from the obstacle while it is inside a safety radius. However, the algorithm requires heading measurements of the obstacle and this is not available in this project, though it could be assumed to be similar to the course of the obstacle.

The velocity obstacles algorithm was first introduced in (Fiorini and Shiller; 1998). (Kuwata et al.; 2011) later used the algorithm for maritime surface vehicles, where

several additional features are implemented. Most relevant to this project is that the algorithm is obeying COLREGs such that expected maritime behavior is followed. When an obstacle is inside the vision cone of the vehicle, the vehicle could either go out by turning to the left or the right of the cone. The method they developed chooses the COLREGs compliant option, depending on the relative velocity and bearing of the obstacle to the vehicle. When the vehicle is out of the cone, an extra hysteresis parameter is added. This is the minimum time the vehicle would stay in the mode of avoiding collision with a given obstacle from entering collision avoidance mode with the same obstacle. It is added to refuse the vehicle from going straight back to the collision cone of an obstacle after exiting it, potentially causing the vehicle to have a chattering behavior by entering and exiting the cone. They also implemented a pre-collision check for all obstacles in the environment to check if any of them would reach a point close enough to be classified as in danger of collision.

2.1.2 Constant avoidance angle

The final vision cone based approach considered in this project is the constant avoidance angle (CAA). Starting with the same collision cone with an extra angle to account for relative velocity, a constant course reference is set to tangent the cone. And this is where the constant avoidance angle differs from the two previous: It does not provide a course rate reference which is kept until the vehicle course is out of the cone, but rather a specific course reference such that it tangents the cone with some extra margin. By doing this, the vehicle will drive around the obstacle on a safe distance and can eventually go back to follow some guidance law. This was done in Wiig et al. (2020), where the authors managed to mathematically prove collision avoidance for one obstacle.

A major advantage with the cone based algorithms is that only a yaw rate or course reference is set for each time step, allowing us to independently control the speed (this would require some extra adjustments for the velocity obstacles algorithm). This flexibility could be exploited when integrating maneuvering limitations, also because the vehicle speed should be kept as constant as possible in order not to damage the mine

sweep system. Moreover, the approaches are easy to define as tasks in a hierarchical motion planning system. Another benefit is that we easily can make the vehicle keep the initial turning direction throughout the whole avoidance maneuver to prevent oscillating behavior. This also imitates the expected behavior at sea very well, by making clear maneuvers before keeping constant course and speed. Finally, the cone methods are conceptually tangible and hence easy to illustrate.

2.2 Dynamic window

The dynamic window (DW, (Fox et al.; 1997)) approach reduces the velocity search space to reachable velocities within a short time interval. It chooses translational and rotational velocities by maximizing an objective function. In (Fox et al.; 1997), this cost function consists of terms for progress towards the goal location, forward velocity of a robot and distance to the next obstacle on the trajectory inside the dynamic constraints. The area within these constraints is called the dynamic window, and the constraints are maximum limits for acceleration in translation and rotation.

This method naturally accounts for maneuvering limitations, which is particularly relevant for the scenario with mine sweeps in this project. It is also well suited for vehicles operating in high speed and this is beneficial for the other scenario with high speed formation driving. However, this algorithm provides references for a constant turn rate of the vehicle for some time in order to avoid obstacles. This does not rhyme very well with expected behavior at sea, where one would make a clear turn and potentially change of speed before keeping a constant velocity throughout the whole maneuver. However, efforts have been made to improve the algorithm for marine applications in (Eriksen et al.; 2016), which also makes the algorithm more modular by setting desired surge and yaw rates as inputs instead of a desired heading. This would ease the work of integrating the algorithm to a complete planning algorithm.

2.3 Control barrier functions

Control barrier functions (CBFs) are continuously differentiable functions defining safe sets as super-zero level sets. This means that the CBF remains non-negative for state values at the whole given time domain when the initial value also is non-negative. It is then said to be forward invariant. This can be applied to optimization-based control allocation as an inequality constraint, where the CBF being non-negative implies staying away from collisions. The references for the speed and course controller will be the ones that minimizes the objective function. (Ames et al.; 2019) provided a summary on the recent theoretical work and applications of the approach. (Thyri et al.; 2020) used the method for autonomous surface vehicles, where they separated the water plane into two; one half where the vehicle could move, and one half where the obstacle is located. They also extended this to be COLREGs compliant. A drawback with the algorithm is that it is less intuitive and harder to illustrate, though the optimization problem is well-defined. Since we end up with an optimization problem for finding references for course and speed, it could be hard to put constraints on these since the optimal references may then be outside of the constraints.

2.4 Artificial potential field

The artificial potential field method, first proposed by (Khatib; 1986), is known to be intuitive and easily implementable. The trajectory of the vehicle is determined by repulsive and attractive potential fields around obstacles and targets, respectively. Hence, the vehicle is pushed away from obstacles and dragged towards targets. This approach has great real-time capabilities since no heavy calculations have to be performed for each iteration. Also, it scales very well to multiple obstacles scenarios. Figure 2.2 illustrates how the vehicle will be pushed away from obstacles and dragged towards the target. A more complete picture would include denser vector field indicating which direction and with which amplitude the vehicle is pushed.

Although the method is model independent, intuitive and easy to illustrate, it is known to suffer from local optima. These local minima can trap the vehicle before

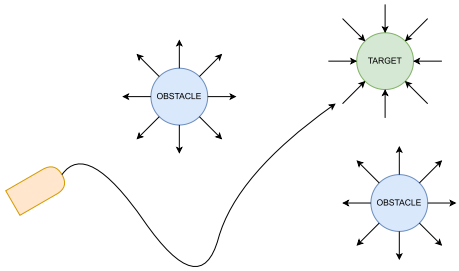

Figure 2.2: Simplified illustration of artificial potential field.

reaching its goal, as illustrated in Figure 2.3. Here, the attractive forces of the target would trap the vehicle between the obstacles, given some specific amplitude configuration on the repelling and attractive forces. The problem of local optima has been an active area of research, and finding a robust solution would make the algorithm more complicated. Furthermore, the method is not particularly modular since it is based on potential field planning. This is not desirable for this project as we want the collision avoidance algorithm to be integrated into a motion planning system, without being dependent on potential fields on all levels. Also, (Singletary et al.; 2020) show that APF is a special case of CBF, and their comparative analysis for quadrotors shows that its path is more stable and predictable with CBF, where the APF made more rapid turns close to the obstacles.

2.5 Model Predictive Control

The model predictive control (MPC) algorithm finds an optimal input for the next time step of the system while taking future time step into account. Hence, for our scenarios with a vehicle on sea, the vehicle can act accordingly to future potential collisions with obstacles. (Eriksen et al.; 2019) developed a variant of this while accounting for dynamic constraints in a discretized search-space, introducing the branching-course MPC (BC-MPC). Here, the search-space of feasible trajectories is restricted by the dynamic constraints. Then, the optimal trajectory is found by finding the trajectory

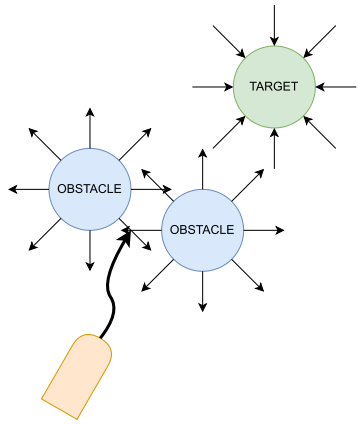

Figure 2.3: Artificial potential field finding a local optima. A better solution would be to navigate around both of the obstacles instead of seeking the narrow corridor between them.

which has the lowest objective function value. This is put into a cost function with a corresponding weight with other terms for following a path. The BC-MPC algorithm is well tested in maritime environments with COLREGs, and it naturally accounts for dynamic constraints. It would therefore serve as a nice candidate for this project, although the guidance is integrated in the algorithm, which requires some adjustments for motion planning integration.

2.6 Choice of collision avoidance algorithm

After presenting and evaluating many popular methods for collision avoidance, a short comparison of the algorithms is presented to find out which of them are better suited. APF is not desirable due to its local minima weakness, as well as it has been argued that CBF has better stability capabilities in (Singletary et al.; 2020). For future mathematical analysis together with lack of modularity this method is eliminated from the list. CBF is also not chosen, as it is less intuitive with several tuning variables with little mathematical analysis. DW is not chosen since it is needs modifications for

imitating maritime behavior, although we have seen work on this in (Eriksen et al.; 2016). MPC, where BC-MPC in (Eriksen et al.; 2019) was considered to be most relevant, was not chosen since we favored modularity and even more intuitive approaches.

Hence, we are left with the cone based approaches. The CAA algorithm was chosen due to some solid and quite recent contributions in Wiig et al. (2020). The performed mathematical analysis, independence from surge speed control and potential for further extensions made us choose this algorithm over the others. Note that there could be strong arguments for choosing any of the other algorithms which we excluded, but the mentioned aspects sums up the justification for our choice.

Chapter 3

Vessel modeling

A dynamic model describes the motion of the vehicle as a result of forces acting on it. Such a model can be used in simulations and vehicle control design. The vehicle will be treated as underactuated for this project, meaning that the vessels are not able to follow arbitrary trajectories in the water plane. Possibilities for sideways actuation will not be exploited.

In this chapter, the motion model of the two USVs will be presented. The USVs are named Odin and Frigg and they are modeled equally with a water jet used for actuation. This water jet model will be presented for explaining the relationship between forces and actuation. Lastly, a motion model of the dynamic obstacles we consider is presented.

3.1 USV equations of motion

The displacement model from Fossen (2011) in 3 degrees of freedom (3-DOF) is used:

$$\dot{\boldsymbol{\eta}} = \boldsymbol{R}(\psi)\boldsymbol{\nu} \tag{3.1a}$$

$$\boldsymbol{M}\dot{\boldsymbol{\nu}} + \boldsymbol{C}(\boldsymbol{\nu})\boldsymbol{\nu} + \boldsymbol{D}(\boldsymbol{\nu})\boldsymbol{\nu} = \boldsymbol{\tau} \tag{3.1b}$$

$\boldsymbol{\eta} = \boldsymbol{\eta}_b^n = [x, y, \psi]^T$, where x and y are the positions of the USV body frame origin in the north and the east direction in the North East Down (NED) reference frame. North and East form a plane tangent to the surface of the Earth with the orthogonal Down direction completing the coordinate frame. The origin is located at a fixed latitude and longitude. ψ is the heading of the the USV in the horizontal plane, also referred to as the yaw angle in NED. $\boldsymbol{\nu} = \boldsymbol{\nu}_{nb}^b = [u, v, r]^T$, where u and v are the velocities in surge and sway, and r is the yaw rate. As the notation indicates, these are the velocities of the USV body relative to NED expressed in the body reference frame. Subscripts and superscripts are omitted in the matrix equations for brevity. Wave forces, ocean currents and wind forces are set to be zero for simplicity. $\boldsymbol{\tau}$ is the forces from the water jet and will be elaborated in Section 3.2. The rotation matrix $\boldsymbol{R}(\psi) \in SO(2)$ represents the rotation about the z-axis, which is a rotation from the body reference frame to the NED reference frame:

$$\boldsymbol{R}(\psi) = \boldsymbol{R}_{z,\psi} = \begin{bmatrix} \boldsymbol{R}_b^n(\psi_b^n) & \boldsymbol{0}_{2\times 1} \\ \boldsymbol{0}_{1\times 2} & 1 \end{bmatrix} \tag{3.2}$$

The matrix $\boldsymbol{M}$ is the inertia matrix, $\boldsymbol{C}(\boldsymbol{\nu})$ is the Coriolis and centripetal matrix and $\boldsymbol{D}(\boldsymbol{\nu})$ is the hydrodynamic damping matrix. For the structure of these matrices, the following assumption is made:

Assumption 3.1: The origin of the body reference frame is located in $[0, 0]^T$ along the centerline of the USV and is the pivot point of the USV.

Remark: If the pivot point located as defined, one does not need to translate the origin to the pivot point through a coordinate transformation. This is described in (Fossen; 2011).

The inertia matrix is given as

$$\boldsymbol{M} = \boldsymbol{M}_{RB} + \boldsymbol{M}_A \tag{3.3a}$$

$$\boldsymbol{M}_{RB} = \begin{bmatrix} m & 0 & 0 \\ 0 & m & 0 \\ 0 & 0 & I_z \end{bmatrix}, \boldsymbol{M}_A = -\begin{bmatrix} X_{\dot{u}} & 0 & 0 \\ 0 & Y_{\dot{v}} & Y_{\dot{r}} \\ 0 & N_{\dot{v}} & N_{\dot{r}} \end{bmatrix} = 0 \tag{3.3b}$$

$\boldsymbol{M}_{RB}$ is the rigid body mass, with element m being the mass of the USV and I_z being the moment of inertia about the z-axis. The off-diagonal elements in $\boldsymbol{M}_{RB}$ are set to zero due to Assumption 3.1 and the following:

Assumption 3.2: The USV is port-starboard symmetric.

Remark: This implies that surge is decoupled from sway and yaw.

$\boldsymbol{M}_A$ is the hydrodynamic added mass and is dependent of the natural periods in seakeeping analysis. It can be complicated to find accurate estimates of the coeffiecients in this matrix, and the matrix is therefore set to be zero in the simulator for simplicity.

The Coriolis and centripetal matrix is given as

$$\boldsymbol{C}(\boldsymbol{\nu}) = \boldsymbol{C}_{RB}(\boldsymbol{\nu}) + \boldsymbol{C}_A(\boldsymbol{\nu}) \tag{3.4a}$$

$$\boldsymbol{C}_{RB}(\boldsymbol{\nu}) = \begin{bmatrix} 0 & 0 & -mv \\ 0 & 0 & mu \\ mv & -mu & 0 \end{bmatrix}, \boldsymbol{C}_A(\boldsymbol{\nu}) = \begin{bmatrix} 0 & 0 & Y_{\dot{v}}v + Y_{\dot{r}}r \\ 0 & 0 & -X_{\dot{u}}u \\ -Y_{\dot{v}}v - Y_{\dot{r}}r & X_{\dot{u}}u & 0 \end{bmatrix} = 0 \tag{3.4b}$$

$\boldsymbol{C}_{RB}$ is the rigid body Coriolis and centripetal matrix. $\boldsymbol{C}_A$ is the hydrodynamic added mass Coriolis and centripetal matrix. The structure comes out from Assumption 3.1. Note that also here the hydrodynamic added mass matrix $\boldsymbol{C}_A$ is set to zero for the same reason as with $\boldsymbol{M}_A$, such that

$$\boldsymbol{M} = \boldsymbol{M}_{RB} \tag{3.5a}$$

$$\boldsymbol{C}(\boldsymbol{\nu}) = \boldsymbol{C}_{RB}(\boldsymbol{\nu}) \tag{3.5b}$$

The hydrodynamic damping matrix is given as

$$\boldsymbol{D}(\boldsymbol{\nu}) = \boldsymbol{D}_L + \boldsymbol{D}_{NL}(\boldsymbol{\nu}) \tag{3.6a}$$

$$
\begin{aligned}
\boldsymbol{D}_L &= -\begin{bmatrix} X_u & 0 & 0 \\ 0 & Y_v & Y_r \\ 0 & N_v & N_r \end{bmatrix}, \\
\boldsymbol{D}_{NL}(\boldsymbol{\nu}) &= -\begin{bmatrix} X_{|u|u}|u| + X_{uuu}u^2 & 0 & 0 \\ 0 & Y_{|v|v}|v| + Y_{vvv}v^2 & 0 \\ 0 & 0 & N_{|r|r}|r| + N_{rrr}r^2 \end{bmatrix}
\end{aligned} \tag{3.6b}
$$

$\boldsymbol{D}_L$ and $\boldsymbol{D}_{NL}(\boldsymbol{\nu})$ are the linear and the nonlinear part of the hydrodynamic damping matrix, respectively.

This model is only valid for displacement vessels. Because Odin and Frigg are planing vessels, this is disadvantageous. Finding a model which captures Odin and Frigg's dynamics at high speeds is a difficult and time consuming task. However, Odin and Frigg can be considered displacement vessels at lower speeds. Thus, for simplicity, we use the model described above in our simulator. It still covers many of our simulating needs, as long as the tests do not require simulation of accurate motion in high speed. Also, for the scenario with mine sweeps the vessels are not operating in high speed, making this model better suited.

The following assumption was also made for the displacement model:

Assumption 3.3: The surge speed u_b lies in the interval

$$
u_b \in \left[u_{b,min}, u_{b,max}\right], \tag{3.7}
$$

where $u_{b,max} > u_{b,min} \geq 0$ are constants.

Remark: The limitation in surge speed exists to make sure that the USV operates at a speed where the displacement model is valid. The USV will hence not be able to reverse since the minimum thrust is positive in surge direction and the nozzle angle can not exceed 27 degrees. Furthermore, reversing is not of particular relevance for this project.

Formulating the vehicle dynamics component wise yields

$$
\dot{x} = u\cos\psi - v\sin\psi \tag{3.8a}
$$

$$\dot{y} = u \sin\psi + v \cos\psi \tag{3.8b}$$

$$\dot{\psi} = r \tag{3.8c}$$

$$\dot{u} = F_u(u, v, r) + \frac{\tau_u}{m} \tag{3.8d}$$

$$\dot{v} = F_v(u, v, r) + \frac{\tau_v}{m} \tag{3.8e}$$

$$\dot{r} = F_r(v, r) + \frac{\tau_r}{I_z} \tag{3.8f}$$

The functions in the last three equations are the terms from inertia, Coriolis and damping matrices. They are defined as

$$F_u(u, v, r) = vr + \frac{X_u u + X_{|u|u}|u|u + X_{uuu}u^3}{m} \tag{3.9a}$$

$$F_v(u, v, r) = -ur + \frac{Y_r r + Y_v v + Y_{|v|v}|v|v + Y_{vvv}v^3}{m} \tag{3.9b}$$

$$F_r(v, r) = \frac{N_v v + N_r r + N_{|r|r}|r|r + N_{rrr}r^3}{I_z} \tag{3.9c}$$

The numerical parameter values for matrix elements were provided by FFI and can be found in Appendix A.

Numerical integration is used to calculate the vessel pose and velocity in each time step during simulation. Manipulating the matrix from the system dynamics in (3.1) and using the first order Euler method yields

$$\boldsymbol{\nu}[n+1] = \boldsymbol{\nu}[n] + \Delta t \boldsymbol{M}^{-1}(\boldsymbol{\tau} - \boldsymbol{C}(\boldsymbol{\nu}[n])\boldsymbol{\nu}[n] - \boldsymbol{D}(\boldsymbol{\nu}[n])\boldsymbol{\nu}[n]) \tag{3.10a}$$

$$\boldsymbol{\eta}[n+1] = \boldsymbol{\eta}[n] + \Delta t \boldsymbol{R}(\psi)\boldsymbol{\nu}[n+1] \tag{3.10b}$$

where Δt is the time step corresponding to the update rate of the simulator.

3.2 Water jet model

Both Frigg and Odin have two water jets for actuation, placed symmetrically about the centerline. A model of the water jet is necessary for setting the correct motor demands when the later presented surge and yaw rate controllers provide desired forces to follow their respective references. The water jet consists of a nozzle, a reverse bucket and an engine. The water jet model is provided by FFI, and the results from the simplifications with equal actuation on both water jets are derived by us.

The water jet thrust is calculated from the throttle level which is set by either the helmsman or a controller. This throttle command is converted to the desired shaft revolutions per minute (RPM), which lies in the interval $[400, 2000]$. The reverse bucket is a deflector which can be lowered in front of the water jet nozzle to deflect the jet stream, splitting it into three components: One aft jet and two directed forward and to the sides. The reverse bucket position is given as a value between -100 and 100, where -100 is fully lowered with all thrust directed forward and to the sides, 0 is in neutral position where the net resulting force is zero, 100 is fully raised and all thrust is directed to the aft of the vessel. In this project the reverse bucket features will not be exploited, and hence the bucket will be fully raised. The nozzle is used to steer the direction of thrust in the horizontal plane, and has a value in the range $[-27^o, 27^o]$. Both water jets will at all times be provided with equal demands on the nozzle angle and the engine in this project. This will result in an underactuated USV where the nozzle angle of the water jet will serve as a rudder. Figure 3.1 illustrates a system overview of the water jet.

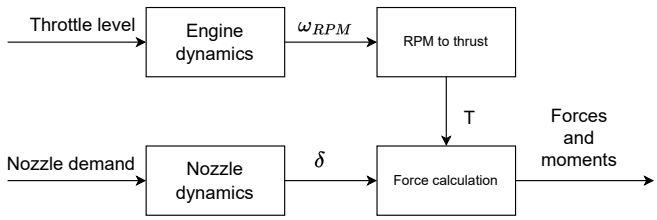

Figure 3.1: Water jet overview.

Maximum and minimum value as well as a maximum rate of change imposes the following constraints to the RPM:

$$\omega_{rpm,d} = \omega_{min} + u_{throttle}(\omega_{max} - \omega_{min}) \tag{3.11}$$

$$\omega_k = \begin{cases} \omega_{k-1} + \dot{\omega}_{max}\frac{a}{b}, & ||\omega_{rpm,d} - \omega_{k-1}|| > \dot{\omega}_{max} \\ \omega_{rpm,d}, & ||\omega_{rpm,d} - \omega_{k-1}|| \leq \dot{\omega}_{max} \end{cases} \tag{3.12}$$

ω_{max} and ω_{min} are the minimum and maximum RPM, respectively. $\dot{\omega}_{max}$ is the maximum RPM rate of change per iteration. ω_k and ω_{k-1} are the RPM values for the current and the previous time step in a discrete update scheme.

The thrust model is developed by performing curve fitting of a second order polynomial function to experimental data. Here, thrust is given for various shaft RPMs and relative water speeds. For this model, fluid dynamic effects caused by pitching, rolling, yaw rate and sway motion of the vessel during high-speed maneuvers are omitted. The resulting thrust is given by

$$T = 0.5\alpha_{rpm(\omega_{rpm})}(a_0 + a_1 u_{knots} + a_2 u_{knots}^2) \tag{3.13}$$

u_{knots} is the water relative speed of the vessel given in knots. α_{rpm} expresses the relation between RPM and thrust:

$$\alpha_{rpm}(\omega_{rpm}) = b_0 + b_1\omega_{rpm} + b_2\omega_{rpm}^2 \tag{3.14}$$

a_i and b_i are constants estimated by the curve fitting algorithm. Their numerical values are not given on request by FFI. The curves were fit to data when driving in 10 knots with 1096 RPM. Consequently, the model fits best while operating around this range.

The nozzle angle dynamics has a similar structure to the engine RPM:

$$\delta = \delta_{min} + u_{nozzle}(\delta_{max} - \delta_{min}) \tag{3.15}$$

$$\delta_k = \begin{cases} \delta_{k-1} + \dot{\delta}_{max}\frac{a}{b}, & ||\delta - \delta_{k-1}|| > \dot{\delta}_{max} \\ \delta, & ||\delta - \delta_{k-1}|| \leq \dot{\delta}_{max} \end{cases} \tag{3.16}$$

δ_{min} and δ_{max} are the minimum and maximum allowed nozzle angles, $\dot{\delta}_{max}$ is the maximum nozzle angle change rate. δ_k and δ_{k-1} are the nozzle angular values for the current and the previous time step in a discrete update scheme.

Since the two water jets are given equal input and the reverse buckets are kept fully raised, the forces and moments from the water jets for the 3DOF system is simplified to be

$$\tau_u = 2T\cos(\delta) \tag{3.17a}$$

$$\tau_v = 2T\sin(\delta) \tag{3.17b}$$

$$\tau_r = -l_{y,port}\frac{\tau_u}{2} + l_{x,port}\frac{\tau_v}{2} - l_{y,starboard}\frac{\tau_u}{2} + l_{x,starboard}\frac{\tau_v}{2} \tag{3.17c}$$

where δ is the nozzle angle, and $l_{x,starboard} = l_{x,port} = L_x$ and $l_{y,starboard} = -l_{y,port}$ are the x and y components of the starboard and port lever arms decomposed in the body frame. The symmetry of the lever arms and the equal input on the two water jets simplifies the last expression:

$$\tau_r = l_x\tau_v \tag{3.18}$$

We have now obtained the complete generalized control force vector

$$\boldsymbol{\tau} = \begin{bmatrix} \tau_u \\ \tau_v \\ \tau_r \end{bmatrix} \tag{3.19}$$

3.3 Obstacle model

Obstacles are generalized as any surface vehicle, reef or land. They are modeled as moving circular domains with a given radius. Any obstacle with a given center and

radius will be described by the following kinematic equations:

$$\dot{x}_o^n = u_o \cos(\psi_o^n), \tag{3.20a}$$

$$\dot{y}_o^n = u_o \sin(\psi_o^n), \tag{3.20b}$$

$$\dot{\psi}_o^n = r_o, \tag{3.20c}$$

$$\dot{u_o} = a_o, \tag{3.20d}$$

where $\dot{x}_o^n$ and $\dot{y}_o^n$ are the Cartesian coordinates of the obstacle center, u_o and a_o are the forward speed and acceleration and ψ_o^n and r_o are the obstacle heading and heading rate. Note that the heading will not be available for measurement.

Assumption 3.4: The heading rate, r_o, and forward acceleration, a_o, are bounded by

$$r_o \in \left[-r_{o,max}, r_{o,max}\right], \tag{3.21}$$

$$a_o \in \left[-a_{o,max}, a_{a,max}\right], \tag{3.22}$$

where $r_{o,max} \geq 0$ and $r_{o,max} \geq 0$ are constants.

Assumption 3.5: The forward speed, u_o, is bounded by

$$u_o \in \left[0, u_{o,max}\right], \tag{3.23}$$

where $u_{o,max} < u_b$ is constant. This implies that the forward speed of the vehicle is lower bounded by the maximum speed of the obstacle. This will be necessary for guaranteeing collision avoidance of dynamic, uncooperative vehicles. Obviously, we cannot provide any guarantees if the speed of an obstacle would be higher, since the obstacle could then simply chase the vehicle and would eventually collide with it due to its higher speed.

Chapter 4

Control of the USV

The proposed control scheme in this project provide a desired speed and heading for each USV. For this, surge velocity and heading controllers are used. Unlike the surge velocity controller, the heading cannot be controlled directly, but through a heading to yaw rate reference conversion. Hence, a yaw rate controller is also required to obtain the desired heading. In this chapter, all the mentioned controllers will be presented together with a reference model in order to ensure continuous references. Lastly, we will derive the equations needed to convert the desired forces and moments to actuator inputs. All these parts are components of the diagram in Figure 1.2, presenting the high level structure of our control scheme.

4.1 Surge and yaw rate controllers

Let $u_{bd} > 0$ denote desired surge and r_{bd} denote desired yaw rate. In order to make the error dynamics exponentially stable, we implement the following feedback controllers:

$$\tau_u = m(\dot{u}_d - F_u(u, v, r) - k_{p,u}\tilde{u}) \tag{4.1a}$$

$$\tau_r = I_z(\dot{r}_d - F_r(u, v, r) - k_{p,r}\tilde{r}) \tag{4.1b}$$

$\tilde{u} = u - u_d$ and $\tilde{r} = r - r_d$. $k_{p,u} > 0$ and $k_{p,r} > 0$ are the control gains for surge and yaw rate, respectively. Note that we have canceled the terms from (3.8d) and (3.8f) to be left with

$$\dot{\tilde{u}} = -k_{p,u}\tilde{u} \tag{4.2a}$$

$$\dot{\tilde{r}} = -k_{p,r}\tilde{r} \tag{4.2b}$$

Using the C^1 Lyapunov Function Candidates (LFC) $V(e) = \frac{1}{2}e^2$ for $e = \tilde{u}$ and $e = \tilde{r}$ and differentiating the LFC along the trajectories of (4.2a) and (4.2b) yields

$$\dot{V}(\tilde{u}) = \dot{\tilde{u}}\tilde{u} = -k_{p,u}\tilde{u}^2 \tag{4.3a}$$

$$\dot{V}(\tilde{r}) = \dot{\tilde{r}}\tilde{r} = -k_{p,r}\tilde{r}^2 \tag{4.3b}$$

$\dot{V}$ is negative for positive $k_{p,u}$ and $k_{p,r}$. Hence, by Theorem 4.10 in Khalil (2013), they are both uniformly global exponential stable (UGES).

Due to inevitable imperfections in the dynamic system model, real time applications of the controllers are likely to yield stationary deviations. Consequently, integral terms are added to the controllers to be activated during real experiments:

$$\tau_u = m(\dot{u}_d - F_u(u, v, r) - k_{p,u}\tilde{u} - k_{i,u}\int_0^t \tilde{u}(\tau)\, d\tau) \tag{4.4a}$$

$$\tau_r = I_z(\dot{r}_d - F_r(u, v, r) - k_{p,r}\tilde{r} - k_{i,r}\int_0^t \tilde{r}(\tau)\, d\tau) \tag{4.4b}$$

$k_{i,u}, k_{i,r} > 0$ add weight to the term counteracting the integrated error from the beginning of the time series to the current time step.

4.2 Heading controller

The control scheme will provide a desired heading angle to follow, whereas the actuator control for the yaw rate is in the velocity space. Therefore, a heading controller would be desirable for reaching the reference additionally to converting the reference heading

to a desired yaw rate. Since the system dynamics and consequently the yaw rate controller are described relative to the body frame, a heading controller is desirable. Thus, a conversion from course to heading reference is needed.

The flow frame is presented in (Fossen; 2011). It is related to the body frame through a rotation with an angle around the z axis called the crab angle. The crab angle is defined as $\beta_c = \arctan(\frac{v}{u})$, where u and v are the velocities in surge and sway, respectively. Converting a course reference to a heading reference is therefore achievable by

$$\psi_{bd}^n = \chi_d^n - \beta_c = \chi_d^n - \arctan(\frac{v}{u}) \tag{4.5}$$

where ψ_{bd}^n is the desired heading of the body and χ_d is its desired course.

Now, we modify the course controller from (Wiig et al.; 2020) to become a heading controller. Then, the controller will convert the desired heading of the USV to a desired yaw rate which in turn can be tracked by the yaw rate controller. The desired yaw rate is defined as

$$r_d^n = \dot{\psi}_{bd}^n - \text{sat}(k_f \tilde{\psi}_b^n) \tag{4.6}$$

where $\tilde{\psi}_b^n = \psi_{bd}^n - \psi_b^n$ is the deviation from the desired heading and $k_f > 0$ is a proportional gain for the heading deviation. Saturation is added to limit the turning rate and hence the induced sway motion. The saturation function is defined as follows:

$$\text{sat}(k_f \tilde{\psi}_b^n) = \begin{cases} r_{fp}, & k_f \tilde{\psi}_b^n > r_{fp} \\ k_f \tilde{\psi}_b^n, & k_f \tilde{\psi}_b^n \in [-r_{fp}, r_{fp}] \\ -r_{fp}, & k_f \tilde{\psi}_b^n < -r_{fp} \end{cases} \tag{4.7}$$

where $r_{fp} > 0$ is the saturation limit and is chosen by design. We impose a constraint on this value relative to k_f since we want the course deviation to be in the interval $\tilde{\psi}_b^n \in (-\pi, \pi]$:

Assumption 4.1:

$$r_{fp} \leq k_f \pi \tag{4.8}$$

4.3 Reference model

The reference model is implemented to ensure continuous references for the surge velocity, yaw rate and the heading.

4.3.1 Surge and yaw rate

A second-order velocity reference model is chosen for providing continuously differentiable references for the yaw rate and surge. This assures piecewise smooth references for surge and yaw rates and their derivatives, while the jerk will be non-smooth. A second-order low-pass filter from (Fossen; 2011) is used:

$$\frac{v_{d_i}}{r_i^b}(s) = \frac{\omega_{n_i}^2}{s^2 + 2\zeta_i\omega_{n_i}s + \omega_{n_i}^2} \tag{4.9}$$

for $\boldsymbol{\nu_d} = \left[v_{d_1}, v_{d_2}\right]^T = \left[u_{bd}, r_{bd}\right]^T$, $i = \{1, 2\}$. r_i^b is the reference vector from a higher order control law. ζ_i are the relative damping ratios and ω_i are the natural frequencies. Rewriting the expression above in vector form in the time domain yields

$$\ddot{\boldsymbol{\nu}}_d + 2\boldsymbol{\Delta\Omega}\dot{\boldsymbol{\nu}}_d + \boldsymbol{\Omega}^2\boldsymbol{\nu}_d = \boldsymbol{\Omega}^2\boldsymbol{r}^b \tag{4.10}$$

Since $\boldsymbol{\nu_d}$ is the vector of desired velocities of the USV, $\dot{\boldsymbol{\nu}}_{\boldsymbol{d}}$ and $\ddot{\boldsymbol{\nu}}_{\boldsymbol{d}}$ will necessarily be the desired acceleration and jerk, respectively. Furthermore, the matrices $\boldsymbol{\Delta}$ and $\boldsymbol{\Omega}$ represent

$$\boldsymbol{\Delta} = \begin{bmatrix} \zeta_1 & 0 \\ 0 & \zeta_2 \end{bmatrix}, \boldsymbol{\Omega} = \begin{bmatrix} \omega_{n_1} & 0 \\ 0 & \omega_{n_2} \end{bmatrix} \tag{4.11}$$

A state-space representation is

$$\dot{\boldsymbol{x}}_d = \boldsymbol{A}_d\boldsymbol{x}_d + \boldsymbol{B}_d\boldsymbol{r}^b \tag{4.12}$$

with $\boldsymbol{x}_d = \left[\boldsymbol{\nu}_d^T, \dot{\boldsymbol{\nu}}_d^T\right]^T \in \mathbb{R}^4$ and

$$\boldsymbol{A}_d = \begin{bmatrix} \boldsymbol{0}_{2\times 2} & \boldsymbol{I}_n \\ -\Omega^2 & -2\Delta\Omega \end{bmatrix}, \boldsymbol{B}_d = \begin{bmatrix} \boldsymbol{0}_{2\times 2} \\ \Omega^2 \end{bmatrix} \tag{4.13}$$

This representation is used for the implementation in the simulator. Finding $\dot{\boldsymbol{x}}_d$ from the state-space model for each time step and using forward Euler to approximate the next $\boldsymbol{x}_d$:

$$\dot{\boldsymbol{x}}_d[n] = \boldsymbol{A}_d \boldsymbol{x}_d[n] + \boldsymbol{B}_d \boldsymbol{r}^b[n] \tag{4.14a}$$

$$\boldsymbol{x}_d[n+1] = \boldsymbol{x}_d[n] + h\dot{\boldsymbol{x}}_d[n] \tag{4.14b}$$

where h is the time step between each sample of the discretization. With sufficiently small time steps, this approximation should be sufficiently accurate.

4.3.2 Heading

The desired heading is inserted to a reduced equivalent of the system (4.14) with $\boldsymbol{x}_d = \left[\psi_{fd}^n, \dot{\psi}_{fd}^n\right]^T \in \mathbb{R}^2$. The reduced number of states will change the matrices to be

$$\boldsymbol{A}_d = \begin{bmatrix} 0 & 1 \\ -\omega^2 & -2\zeta\omega \end{bmatrix}, \boldsymbol{B}_d = \begin{bmatrix} 0 \\ \omega^2 \end{bmatrix} \tag{4.15}$$

where ζ is the relative damping ratio and ω is the natural frequency. This filtering is done to find the time differentiated desired course angle as well as ensuring that we always have a continuous reference.

4.4 Water jet control

Forces and moments can not be controlled directly, but through the control input. The control input consists of the thrust and the nozzle angle of the water jet. These can be computed by rearranging (3.17) and (3.18) and exploiting trigonometric identities such that

$$T = \frac{\sqrt{\tau_u^2 + \left(\frac{\tau_r}{l_{x,starboard}}\right)^2}}{2} \tag{4.16a}$$

$$\delta = \begin{cases} \arccos\left(\frac{\tau_u}{2T}\right), & \tau_r \geq 0 \\ -\arccos\left(\frac{\tau_u}{2T}\right), & \tau_r < 0 \end{cases} \tag{4.16b}$$

The arccos() function does not distinguish between a positive and a negative value. Thus, the sign of δ is determined by the sign of the desired moment about the z axis.

The desired thrust now needs to be converted to a desired jet shaft RPM. (3.13) and (3.14) are rearranged to get an expression for a desired RPM given a desired thrust:

$$\omega_{rpm,d} = \frac{-b_1 + \sqrt{b_1^2 - 4b_2\left(b_0 - \frac{T}{a_0 + a_1 u_{knots} + a_2 u_{knots}^2}\right)}}{2b_2} \tag{4.17}$$

u_{knots} can be found by measuring the surge velocity in $\frac{m}{s}$ and then converting it to knots. Then, the RPM for the next time step is found using (3.11) and (3.12), where the physical limits of the engine are accounted for. Lastly, the RPM value is converted to its desired throttle demand, respecting the constraints in (3.11) and (3.12). Similarly for the conversion of the nozzle angle to the steering demand in (3.15) and (3.16).

Chapter 5

Collision avoidance: Constant avoidance angle

The main task in this project is to implement a collision avoidance algorithm for two USVs driving in formation. The constant avoidance angle (CAA) algorithm from Wiig et al. (2020) was developed in the specialization project, where COLREGs compliance was added as an extension. The algorithm from the specialization project will be used here, but modified to be used on two USVs driving in formation. Section 5.1 to 5.4 are restated from the specialization project with some modifications and corrections. The extension to multiple obstacles, hysteresis and minimum distance dependent safety angles are new additions to the previous work.

5.1 The vision cone

The constant avoidance angle (CAA) algorithm is based on the vision cone illustrated in Figure 5.1a. The approach is based on finding a constant course reference for the controller system to track such that the USV course follows the angle of the vision cone with an extra safety margin and obstacle velocity compensation.

By treating every obstacle as static circular domains, the vision cone has its geometrical top at the origin of the body reference frame, and tangents the circular obstacle on each side as illustrated in Figure 5.1a. Avoiding course angles between $\alpha^{n(1)}$ and $\alpha^{n(2)}$ relative to NED would prevent the body center of the USV to coincide the circular obstacle domain. However, some safety margin would be preferable in order to add a margin between the USV and the obstacle. This motivates the extended vision cone shown in Figure 5.1b, with an extra safety angle α_o added on each side of the vision cone. Hence we go from $\alpha^{n(1)}$ and $\alpha^{n(2)}$ for the vision cone to $\psi_{\alpha_o}^{(1)}$ and $\psi_{\alpha_o}^{(2)}$ for the extended vision cone.

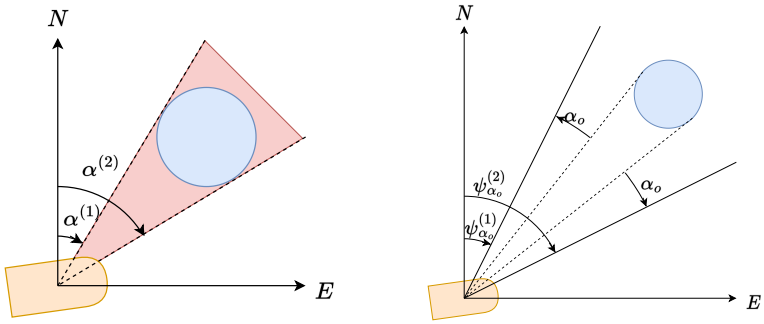

(a) The vision cone

(b) The extended vision cone

Figure 5.1: The orange object represents the USV while the blue circular domain represents an obstacle. In the left figure, the red shaded area between the angles $\alpha^{n(1)}$ and $\alpha^{n(2)}$ is the set of course angles which would cause a collision with the obstacle (given zero obstacle velocity and non-zero USV velocity).

The vision cone introduction above does not account for moving obstacles. Therefore, two velocity vectors are defined along the edges of the extended vision cone:

$$\boldsymbol{v}_{\alpha_o}^{n(j)} = u_{\alpha_o} \begin{bmatrix} \cos\left(\psi_{\alpha_o}^{n(j)}\right) \\ \sin\left(\psi_{\alpha_o}^{n(j)}\right) \end{bmatrix}, j = \{1, 2\} \tag{5.1}$$

$u_{\alpha_o} > 0$ would be the speed of the USV if the obstacle was static. Hence, $\boldsymbol{\nu}_{\alpha_o}^{n(j)}$ represents the velocity of the USV if it drives along edge j of the extended vision cone of a static obstacle. Now, to account for a dynamic obstacle, let the obstacle velocity $\boldsymbol{\nu}_o^n$ be non-zero. Adding this velocity to the USV velocity while driving along one of the edges yields

$$\boldsymbol{\nu}_{ca}^{n(j)} = \boldsymbol{\nu}_{\alpha_o}^{n(j)} + \boldsymbol{\nu}_o^n, j = \{1, 2\} \tag{5.2}$$

Hence, compensation for the relative velocity between the USV and the obstacle is included. This is illustrated in Figure 5.2. The speed of $\boldsymbol{\nu}_{ca}^{n(j)}$ is defined to be

$$||\boldsymbol{\nu}_{ca}^{n(j)}|| = U_b = \sqrt{u_b^2 + v_b^2}, j = \{1, 2\} \tag{5.3}$$

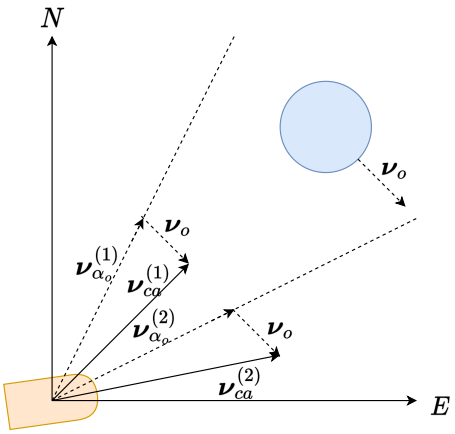

Figure 5.2: The obstacle velocity compensated extended vision cone. $\boldsymbol{\nu}_o^n$ denotes the obstacle reference, which is added to the USV velocity $\boldsymbol{\nu}_{\alpha_o}^{n(j)}$ when driving along edge j of the extended vision cone to create the new reference $\boldsymbol{\nu}_{ca}^{n(j)}$.

i.e. the total speed of the USV. With these new velocity references, the extra angle to add to $\psi_{\alpha_o}^{n(j)}$ to obtain the desired reference angle is required. Consider Figure 5.3, illustrated with edge number 2. Some previously introduced vectors and angles are

omitted in this figure for the purpose of focusing on the relevant vectors and angles for this part. The sine rule is applied to obtain

$$\begin{aligned} \frac{\sin\left(\gamma_{ca}^{n(j)}\right)}{||\boldsymbol{\nu}_o^n||} &= \frac{\sin\left(\gamma_{vo}^{n(j)}\right)}{||\boldsymbol{\nu}_{ca}^{n(j)}||} = \frac{\sin\left(\gamma_{vo}^{n(j)}\right)}{\sqrt{u_b^2 + v_b^2}} \\ \implies \gamma_{ca}^{n(j)} &= \arcsin\left(\frac{||\boldsymbol{\nu}_o^n|| \sin\left(\gamma_{vo}^{n(j)}\right)}{\sqrt{u_b^2 + v_b^2}}\right), j = \{1, 2\} \end{aligned} \tag{5.4}$$

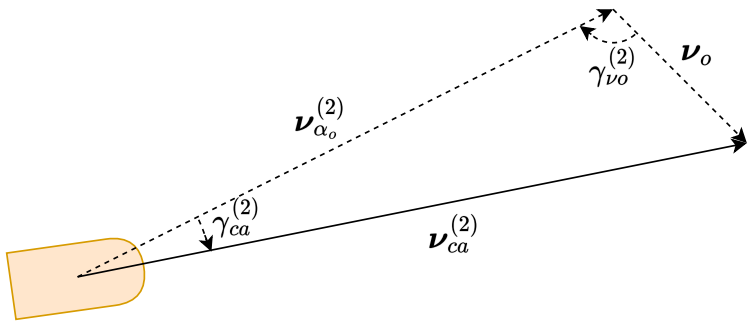

Figure 5.3: The triangle composed of the USV velocity $\boldsymbol{\nu}_{\alpha_o}^{(2)}$ when driving along edge 2, the obstacle velocity $\boldsymbol{\nu}_o^n$ and the new velocity $\boldsymbol{\nu}_{ca}^{(2)}$. Angles $\gamma_{ca}^{(2)}$ and $\gamma_{vo}^{(2)}$ in the triangle are introduced.

Since $y = \arcsin(x) \implies |x| \leq 1$, the following constraint is imposed for (5.7) to be well-posed:

Assumption 5.1:

$$U_b \geq ||\boldsymbol{\nu}_o^n|| \left|\sin\left(\gamma_{vo}^{n(j)}\right)\right| \tag{5.5}$$

Also, note the following:

$$\gamma_{vo}^{n(j)} > \pi \implies \gamma_{ca}^{n(j)} < 0 \tag{5.6}$$

Which modifies (5.4) to

$$\gamma_{ca}^{n(j)} = \text{sgn}(\pi - \gamma_{vo}^{n(j)}) \arcsin\left(\frac{||\boldsymbol{\nu}_o^n|| \sin\left(\gamma_{vo}^{n(j)}\right)}{\sqrt{u_b^2 + v_b^2}}\right), j = \{1, 2\} \tag{5.7}$$

From the measurement system in the USVs, the obstacle speed $||\boldsymbol{\nu}_o^n||$ is available as well as the USV speed $\sqrt{u_b^2 + v_b^2}$. The only factor which is yet to be found is therefore $\gamma_{vo}^{n(j)}$. This can be found geometrically (see Figure 5.4 for validation on edge 2) by

$$\gamma_{vo}^{n(j)} = \pi + \psi_{\alpha_o}^{n(j)} - \psi_o^n = \pi - \left(\psi_o^n - \psi_{\alpha_o}^{n(j)}\right), j = \{1, 2\} \tag{5.8}$$

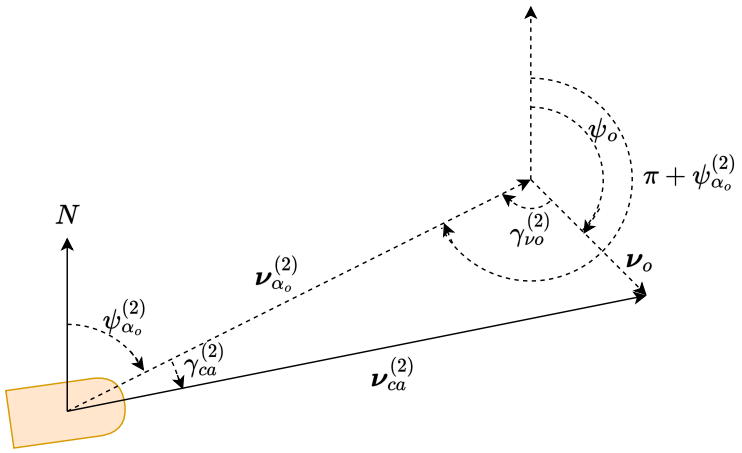

Figure 5.4: Triangle of $\boldsymbol{\nu}_{\alpha_o}^{(2)}$, $\boldsymbol{\nu}_o^n$ and $\boldsymbol{\nu}_{ca}^{(2)}$. Angles $\psi_{\alpha_o}^{n(j)}$, ψ_o^n and $\pi + \psi_{\alpha_o}^{n(j)}$ are added for illustrating how $\gamma_{vo}^{(2)}$ is found.

The obstacle heading is not available for measurement with the sensors on the

USVs, but the obstacle course χ_o^n is. Therefore, the following assumption is made:

Assumption 5.1: The obstacle heading is equal to its course, i.e. $\psi_o^n = \chi_o^n$.

Remark: When the obstacle velocity is zero and hence the course is undefined, this assumption is not needed as there is no obstacle velocity to compensate for. Therefore, the extended vision cone is sufficient. For non-zero obstacle velocities the assumption will be true when the obstacle drives in a straight line in the absence of ocean currents. If the obstacle makes turns, it will provide a non-zero crab angle which will not be considered. This angle is normally small for small turns, and will therefore be neglected in this project.

By following this assumption, (5.8) is modified to be

$$\gamma_{vo}^{n(j)} = \pi - \left(\chi_o^n - \psi_{\alpha_o}^{n(j)}\right), j = \{1, 2\} \tag{5.9}$$

Now, all derived angles can be obtained given the measurement input. Thus, the two edges of the extended vision cone with obstacle velocity compensation can be defined:

$$\chi_{dca}^{n(j)} = \psi_{\alpha_o}^{n(j)} + \gamma_{ca}^{n(j)}, j = \{1, 2\} \tag{5.10}$$

where $\gamma_{ca}^{n(j)}$ can be found from (5.7) with $\gamma_{vo}^{n(j)}$ found from (5.9). Note that $\chi_{dca}^{n(j)}$ is defined as a course angle since the length of $\boldsymbol{\nu}_{ca}^{n(j)}$ is set to be equal to the total speed of the vehicle in the positive surge direction of the flow frame. This will define the angle of the reference velocity in the NSB framework in Chapter 6.

$\psi_{\alpha_o}^{n(j)}$ is obtained by first finding the angle of the vector from the USV and the obstacle in NED. This is achievable using $\arctan\left(\frac{y_o^n - y_b^n}{x_o^n - x_b^n}\right)$. Their respective positions are available for measurement. Then, $\alpha^{n(j)}$ is obtained by adding or subtracting the radius times the orthogonal unit vector of the vector between the USV and the obstacle. The angle of the orthogonal unit vector is denoted $\alpha_{R_o}^{n(j)}$. Finally, some safety margin α_o is added or subtracted to obtain the expression for $\psi_{\alpha_o}^{n(j)}$:

$$\gamma_o^n = \arctan\left(\frac{y_o^n - y_b^n}{x_o^n - x_b^n}\right) \tag{5.11a}$$

$$\alpha_{R_o}^{n(j)} = \begin{cases} \gamma_o^n - \frac{\pi}{2}, & j = 1 \\ \gamma_o^n + \frac{\pi}{2}, & j = 2 \end{cases} \tag{5.11b}$$

$$\psi_{\alpha_o}^{n(j)} = \begin{cases} \gamma_t - \alpha_o, & j = 1 \\ \gamma_t + \alpha_o, & j = 2 \end{cases} \tag{5.11c}$$

$$\gamma_t = \arctan\left(\frac{y_o^n - y_b^n + R_o \sin\left(\alpha_{R_o}^{n(j)}\right)}{x_o^n - x_b^n + R_o \cos\left(\alpha_{R_o}^{n(j)}\right)}\right) \tag{5.11d}$$

$$\alpha^{n(j)} = \gamma_o^n + \gamma_t \tag{5.11e}$$

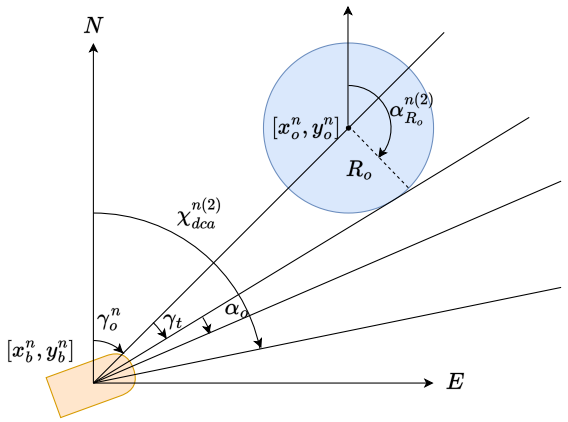

Figure 5.5: Overview of angles in (5.11).

See Figure 5.5 for a visualization of the angles. Since the angles might vary between $(-\pi, \pi]$, the arctan 2() function is required to exploit the information from the signs of the numerator and the denominator individually. α_o is the safety margin discussed

in this section and is chosen by design.

5.2 Collision avoidance mode

In the absence of obstacles, the USVs will have freedom to follow a predefined path and maintain a desired formation. For this reason, an entrance rule for the collision avoidance mode is introduced. We denote the obstacle velocity compensated extended vision cone V_c. A distance d_{ca} between the USV and any obstacle defines the maximum distance for when action should be taken to avoid collisions. The requirements for entering collision avoidance mode are therefore

$$\chi_d^n(t) \in V_c(t) \tag{5.12a}$$

$$d_{bo}(t) \leq d_{ca} \tag{5.12b}$$

$\chi_d^n(t)$ is the desired course of the vehicle, provided by the control scheme, and $d_{bo}(t)$ is the current distance between the USV center and the obstacle center. At time t, $\chi_d^n(t)$ cannot be within the vision cone for any given obstacle when the distance d_{bo} between them is less than d_{ca}. d_{ca} is chosen by design based on how early collision avoidance mode should be entered, and $\chi_d^n(t)$ would normally come from some guidance algorithm which is used when there are no obstacles nearby on collision course with the USV.

The USV is allowed to exit collision avoidance mode when the desired angle is not within the obstacle velocity compensated extended vision cone anymore:

$$\chi_d^n(t) \notin V_c(t) \tag{5.13}$$

This implies that no action needs to be taken to prevent an obstacle even if it is closer than d_{ca}. The reason is that the USV is already about to circumvent it. However, one aspect has to be considered: If the desired course of the vehicle outside collision avoidance mode $\chi_d^n(t)$ would make it cross V_c, the maneuver cannot be performed. This is because it would bring the vehicle back on collision course with the obstacle.

Since the distance between the vehicle and the obstacle outside collision avoidance mode is not respected, they may be arbitrarily close in case of rapid turns. Hence, crossing V_c could lead the USV straight into collision with the obstacle. Therefore, actions outside collision avoidance mode is refused if it would bring the vehicle back to the cone. Then, the desired course angle has to pass the following criteria with respect to the edges of the cone:

$$\begin{aligned} \chi_d^n(t) - \chi_{dca}^{n(1)} &\leq 0 \\ \chi_d^n(t) - \chi_{dca}^{n(2)} &\geq 0 \end{aligned} \tag{5.14}$$

If these conditions are not fulfilled, the USV stays in collision avoidance mode and follows the constant avoidance angle.

To make sure that the vehicle performs the shortest turn, the angular difference is mapped to the interval

$$\left(\chi_d^n(t) - \chi_{dca}^{n(j)}\right) \in (-\pi, \pi], j = 1, 2 \tag{5.15}$$

5.3 Turning direction for static obstacles

The constant avoidance algorithm provides two alternatives for which course reference to set; either $j = 1$ or $j = 2$, i.e. a clockwise or a counterclockwise turning direction. Only one of them can be chosen, and it will be distinguished between whether the obstacle has a zero or a non-zero velocity.

When the obstacle has zero velocity, it will be avoided by choosing the reference course which is closest to the current course of the USV:

$$j = \arg\min_{j=1,2} |\chi_{dca}^{n(j)} - \chi_b^n| = \arg\min_{j=1,2} |\chi_{dca}^{n(j)} - \arctan\left(\frac{\dot{y}_b^n}{\dot{x}_b^n}\right)| \tag{5.16}$$

The USV simply chooses the avoidance angle which is easiest to reach. This is particularly beneficial in the case of late obstacle detection, such that it chooses the shortest way out of collision course. When obstacles have non-zero velocity, they are treated like marine vehicles which are required to obey COLREGs. Consequently,

the correct turning direction is chosen after classifying the COLREGs scenario of the encounter.

5.4 COLREGs

The International Regulations for Preventing Collisions at Sea (COLREGs) describe how marine vehicles should behave in order to safely navigate at sea when there is a risk of collision (Cockcroft and Lameijer (2011)). There are 38 rules, but most of them are written for human interpretation rather than quantitative rules for machine decision making. Therefore, attention is only given to a subset of the rules which are quantitative. This has also been done several of the maritime collision avoidance research efforts, e.g. (Kuwata et al.; 2011), (Johansen et al.; 2016) and (Eriksen et al.; 2019). Hence, we are focusing on decision making based on Rules 8 and 13-17 from Cockcroft and Lameijer (2011):

8. Vehicles should take action in order to avoid collisions as early as possible. The convention is to take early action and clearly change speed and course before keeping them constant.

13. Overtaking: When one vehicle is about to overtake another, it should keep out of the way of the other. A vehicle is considered as overtaking another when coming up to more than 22.5° abaft the beam of the overtaken vehicle. It is preferred to overtake a vehicle on her port side in case of an upcoming crossing situation for the overtaken vehicle which could force her to perform a starboard turn. However, the vehicle is allowed to pass on either side.

14. Head-on: When two vehicles are meeting on almost reciprocal courses, often defined to be within an angle of ±6° from the head of the ship. The vehicles are obliged to perform a starboard turn such that they pass on each other's port side.

15. Crossing: When two vehicles are on crossing course where there is a risk of collision, the vehicle which has the other at her starboard side should give way

and, if possible, avoid to cross ahead of the other vehicle.

16. Action by give-way vehicle: The vehicle should perform early and substantial action to avoid collision with the stand-on vehicle.

17. Action by stand-on vehicle: This vehicle shall keep the course and speed. However, if the other vehicle is not taking appropriate action to keep out of the way and avoiding collision cannot be done by the give-way vehicle alone, the stand-on vehicle should take action to prevent a collision from happening.

Remark: The situation definitions above are given that the two vehicles considered are sufficiently close to each other, which will be marked with the distance limit of the collision avoidance mode. Taking early and substantial action will be interpreted as having a reasonably large distance limit.

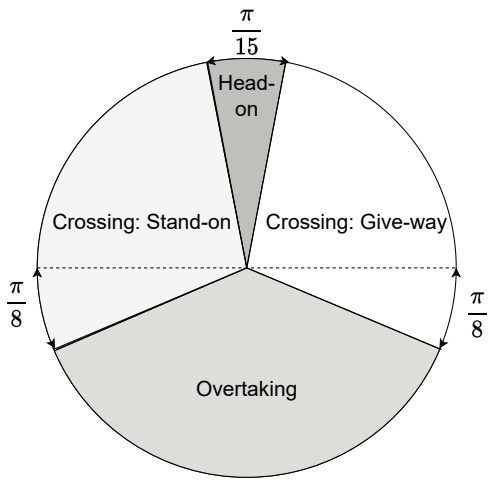

Figure 5.6: COLREGs classification figure.

5.4.1 COLREGs compliance

Based on the selection of rules, the USV might be classified in five possible scenarios when interacting with other vehicles; head-on, crossing from starboard, crossing from

port, overtaking and being overtaken. Classification of the COLREGs scenario and decision making based on the encounter classification will be covered in this part. See Figure 5.7 for an overview of the conventional behavior in each scenario. For classification of COLREGs scenarios, please have a look at Figure 5.6, which shows for which values of $\chi_b^n - \chi_o^n$ each situation is classified. Before delving into each scenario, the course difference should be mapped to the interval

$$\chi_b^n - \chi_o^n \in (-\pi, \pi] \tag{5.17}$$

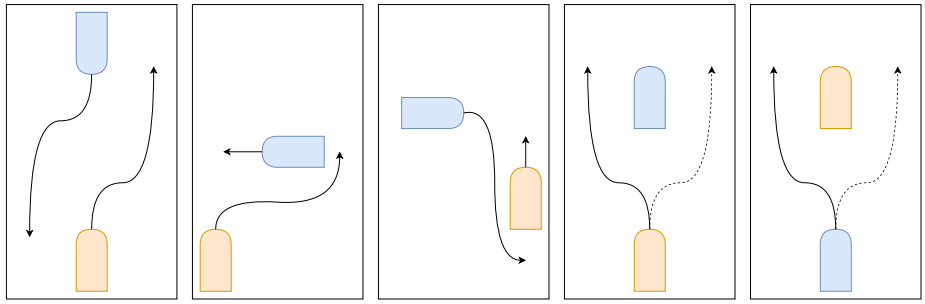

Figure 5.7: The required maneuvers for each COLREGs situation. From left to right: Head-on, crossing give-way, crossing stand-on overtaking and being overtaken. The solid arrows mark expected maneuvers, while the dashed arrows mark alternative, but not desirable maneuvers.

5.4.1.1 Head-on

Recall Figure 5.6. A head-on situation is identified when the USV and the obstacle are meeting on reciprocal courses, with a margin of $\frac{\pi}{30}$:

$$|\chi_b^n - \chi_o^n| = |\arctan\left(\frac{\dot{y}_b^n}{\dot{x}_b^n}\right) - \arctan\left(\frac{\dot{y}_o^n}{\dot{x}_o^n}\right)| \geq \frac{29\pi}{30} \tag{5.18}$$

Here, the starboard turn which tangents the compensated extended vision cone is always chosen. I.e. the USV always turns in the clockwise direction such that the vehicles cross on each other's port side:

$$j = 2 \tag{5.19}$$

5.4.1.2 Crossing: Give-way

In a crossing situation where the USV has the obstacle on its starboard side, the USV is required to take action by performing a starboard turn to cross behind the obstacle. This type of encounter is defined when the course difference between the USV and the obstacle is larger than the head-on situation, and less than when the obstacle comes $\frac{\pi}{8}$ abaft the beam of the USV from the starboard side:

$$\frac{3\pi}{8} \leq \chi_b^n - \chi_o^n \leq \frac{29\pi}{30} \tag{5.20}$$

Similar to the head-on scenario, a starboard maneuver is chosen to cross behind the obstacle:

$$j = 2 \tag{5.21}$$

5.4.1.3 Crossing: Stand on

In a crossing situation where the USV has the obstacle on its port side, the USV should keep a constant course and speed throughout the crossing, such that the obstacle can perform a starboard turn to cross behind the USV. This situation is recognized when the course difference between the USV and the obstacle is more negative than the head-on situation and larger than when the obstacle comes $\frac{\pi}{8}$ abaft the beam of the USV from the port side:

$$-\frac{29\pi}{30} \leq \chi_b^n - \chi_o^n \leq -\frac{3\pi}{8} \tag{5.22}$$

The required action from the USV is to keep constant course and speed. Therefore, no j is chosen, but rather the references

$$\psi_{fdca}^n = \chi_b^n(t_1) \tag{5.23a}$$

$$u_{bd} = u_b(t_1) \tag{5.23b}$$

where χ_b^n and u_b were the course and speed of the USV when entering the collision avoidance mode at time t_1.

5.4.1.4 Overtaking

The overtaking scenario is defined when the obstacle is coming from behind:

$$-\frac{3\pi}{8} \leq \chi_b^n - \chi_o^n \leq \frac{3\pi}{8} \tag{5.24}$$

For this interval of course differences, the USV might be in two different scenarios: Overtaking or being overtaken. Which of them can be determined by comparing the speed of the USV and the obstacle. If the USV speed is the highest, the USV is overtaking the obstacle. If the obstacle speed is the highest, the USV is being overtaken.

If the USV is being overtaken by the obstacle, it can continue normal operation without setting any course or speed references. If the USV is overtaking the obstacle, COLREGs rule 13 states that the USV can choose which side to pass the obstacle as long as it is not interfering the obstacle's operation. Therefore, there are no obligations on which turn to take for this scenario. However, since passing on the port side of the overtaken vehicle is preferred, a counterclockwise turn ($j = 1$) is desirable. On the other hand, it is undesirable to force a crossing of almost the whole cone if the USV rather could make a slight turn to stay away from danger. This reasoning leads to the following turning direction selection:

$$j = \begin{cases} 2, & \chi_{dca}^{n(2)} - \chi_b^n < \epsilon_{overtake} \\ 1, & otherwise \end{cases} \tag{5.25}$$

where $\epsilon_{overtake}$ is a small constant. The constant represents the greatest turn the USV can make to overtake the obstacle on the obstacle's port side. This extra condition was added in case the way out from the compensated extended vision cone is very short. Hence, the port turn is favored unless the turn is too large compared with the starboard turn

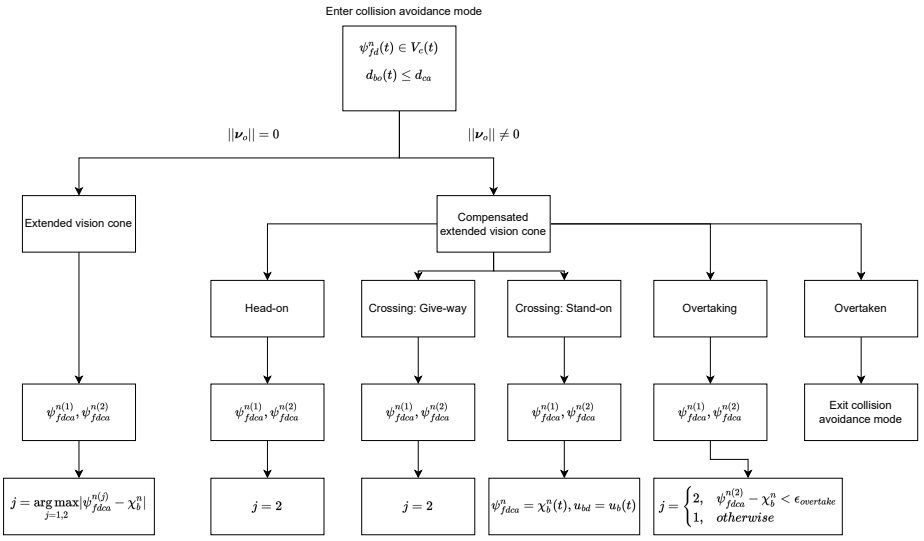

Figure 5.8: Flow chart of which action to perform in the different scenarios. Conditions for the scenarios are omitted for brevity, but can be found in their respective subsections in 5.4.1

Now, all our selected COLREGs situations are classified with their respective desired actions defined. Figure 5.8 shows an overview of the flow for which turning direction to perform based on the classification of the scenario.

5.4.2 Critical mode

The choice of turning direction is based on the assumption that the obstacle is also obeying COLREGs. Despite this being a reasonable assumption, an autonomous vehicle should manage situations when this is not the case. Although the fault is not on the USV's side, collisions should be prevented at all costs. Therefore, the principal of critical distance is introduced, a simplified version of the critical distance derivations in (Eriksen et al.; 2019). Instead of making constant velocity assumptions of the USV and the obstacle, the distance between the USV and the obstacle is used directly

to determine the entrance to the critical mode. When the USV course is inside the compensated extended vision cone and it is critically close to the obstacle, a rapid turn away from the obstacle will be made. The USV enters the critical mode when

$$\chi_d^n(t) \in V_c(t) \tag{5.26a}$$

$$d_{bo}(t) \leq d_{critical} \tag{5.26b}$$

These conditions are identical to (5.12), but with $d_{critical} < d_{ca}$ as the distance constraint. This limit should be larger than the radius of the obstacle, but how much larger depends on the turning capabilities of the USV. If the USV can make fast turns and the operating speed is not too high, the critical distance can be kept small, and it should be larger if the turning rate is low. In any case, it is desirable to keep the critical distance as low as possible given that the USV manages to escape the emergency. This is because the behavior of the USV should be as predictable as possible for others without doing unnecessary turns.

The turning direction during the critical mode is the shortest way out of the collision cone given the current course, just like for the static obstacle scenario:

$$j = \arg\min_{j=1,2} |\chi_{dca}^{n(j)} - \chi_b^n| \tag{5.27}$$

5.5 Minimum distance

Recall that α_o from Section 5.1 was set as a tuning parameter. The parameter determines the desired angular margin to the obstacle. For static obstacles, it can be expressed as a function of the distance to the obstacle and some desired minimum distance margin δ from the USV to the obstacle (see Figure 5.9):

$$\alpha_o = \arctan\left(\frac{\delta}{d_{ca}}\right) \tag{5.28}$$

δ indicates the shortest distance between the USV and the obstacle: This is when the USV tangents a circle with its centre in the USV position at the entrance of the

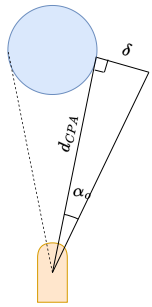

Figure 5.9: Relation between α_o and minimum distance between USV and obstacle

collision avoidance mode and a radius of d_{ca}, which is the distance between the USV and the obstacle at the collision avoidance mode entrance. For dynamic obstacles, the d_{ca} would need to be replaced by the distance to the closest point of approach. Inspired by (Kuwata et al.; 2011), the time until the closest time of approach is given as

$$t_{CPA} = \begin{cases} 0, & ||\boldsymbol{v}_o - \boldsymbol{v}_b|| < \epsilon \\ \frac{(\boldsymbol{p}_o - \boldsymbol{p}_b)^T (\boldsymbol{v}_o - \boldsymbol{v}_b)}{||\boldsymbol{v}_o - \boldsymbol{v}_b||}, & \text{otherwise} \end{cases} \tag{5.29}$$

$\boldsymbol{p}_b$, $\boldsymbol{p}_o$, $\boldsymbol{v}_b$ and $\boldsymbol{v}_o$ denote the position and velocity for the USV and the obstacle. t_{CPA} is the time when the USV and the obstacle are closest to each other, given that both maintain the current velocity. The corresponding distance is found to be

$$d_{CPA} = |(\boldsymbol{p}_o + t_{CPA}\boldsymbol{v}_o) - (\boldsymbol{p}_b + t_{CPA}\boldsymbol{v}_b)| \tag{5.30}$$

Then, α_o for dynamic obstacles is calculated to be

$$\alpha_o = \arctan\left(\frac{\delta}{d_{CPA}}\right) \tag{5.31}$$

Hence, a lower bound for the obstacle distance can be specified and α_o can be determined accordingly.

5.6 Multiple obstacles

In the case of the USV being on collision course with more than one obstacle at the same time, there are more than one collision cones to stay away from. The USV should have entered collision avoidance mode for all of these obstacles given that their respective distances to the USV are under the threshold value presented in (5.12). The cones for the different obstacles will in this case necessarily be overlapping, facilitating a merge of the respective cones. This was also suggested in Wiig et al. (2020).

When multiple obstacles are within the collision avoidance mode distance, but not necessarily on collision course with the USV, the USV might pass between the obstacles. In this scenario, attention must be paid to the distance between the obstacles such that it is sufficiently large for the size of the USV. Therefore, non-overlapping vision cones should be merged if the distance between them is smaller than the radius of the USV.

One problem arises when the collision avoidance algorithm is expanded to multiple obstacles. If two obstacles are classified in different COLREGs scenarios, they might lead to conflicting desired behavior from the USV. For example, one give-way and one stand-on scenario would tell the USV both to keep the current course and speed and to perform a starboard turn. Hence, there are two conflicting course references provided. Therefore, dynamic obstacles are assumed to be in the same COLREGs scenario, limiting the flexibility of the multiple obstacle case. A rigorous analysis of multiple obstacles is not performed in this project.

5.7 Hysteresis

It is desirable to enter and exit the collision avoidance mode as infrequent as possible, since the USV needs some time to adjust to a new path. Also, by exiting collision avoidance mode as soon as the USV is not on collision course with an obstacle, the USV might turn straight back to collision course, which could cause a chattering behavior in and out from collision avoidance mode. To alleviate this, a hysteresis condition is added. The hysteresis will determine the minimum time the USV will have to remain in

collision avoidance mode during an encounter. Therefore, the closest point of approach (CPA) is calculated. But instead of finding the CPA distance, we utilize the CPA time and set the hysteresis equal to this.

The CPA time was defined in (5.29). The assumption of constant velocities for the USV and the obstacle will in all cases be violated to some extent, as the USV makes a turn in the beginning of the maneuver. However, the USV speed will be kept constant throughout all encounters, such that a discrepancy will only be caused by the USV turn. A significant velocity change of the obstacle could also violate the assumption, with the consequence that the USVs exits and enters the collision avoidance mode, causing some frequent course changes. However, these course changes are necessary to adapt to the obstacle velocity changes.

The CPA time dependent hysteresis is particularly beneficial when running a control scheme distributed on the two USVs. Running it distributed implies that there might be small differences in when the USVs enter collision avoidance mode due to asynchronous measurements or delays from one USV to the other. But measuring the CPA time could compensate for this, making the USVs exit collision avoidance mode closer in time.

Chapter 6

Null-space-based behavioral control

The collision avoidance algorithm is aimed to be integrated into a control scheme ensuring fully autonomous driving. For the purpose of driving the two underactuated USVs in formation while following a given path, the null-space-based (NSB) behavioral control scheme from Eek et al. (2020) is chosen. This controller allows accomplishment of several tasks sorted by priority. The highest priority task will always provide references in order for it to be accomplished, while the lower priority tasks provide references given that they do not interfere with the references set by the higher priority tasks.

6.1 Mathematical foundation

The task variable is denoted $\boldsymbol{\sigma} \in \mathbb{R}^m$ and the system configuration is $\boldsymbol{p} = [x_1, y_1, x_2, y_2]$, where $[x_1, y_1]$ and $[x_2, y_2]$ are the positions of the two vehicles. m refers to the number of task parameters. The relationship between $\boldsymbol{\sigma}$ and $\boldsymbol{p}$ is

$$\boldsymbol{\sigma} = \boldsymbol{f}(\boldsymbol{p}) \tag{6.1}$$

where the time derivative is

$$\dot{\boldsymbol{\sigma}} = \frac{\partial \boldsymbol{f}(\boldsymbol{p})}{\partial \boldsymbol{p}} \frac{d\boldsymbol{p}}{dt} = \frac{\partial \boldsymbol{f}(\boldsymbol{p})}{\partial \boldsymbol{p}} \boldsymbol{v} = \boldsymbol{J}(\boldsymbol{p})\boldsymbol{v} \tag{6.2}$$

$\boldsymbol{J} \in m \times 4$ is the configuration dependent task Jacobian matrix and $\boldsymbol{v}$ is the system velocity, i.e. the 2D velocities of the two USVs. Generation of the motion references from the desired task values $\boldsymbol{\sigma}_d$ is done by inverting the locally linear mapping (6.2) (see Arrichiello et al. (2006) for details). Hence, velocity references are obtained inverting (6.2) using the Moore-Penrose pseudoinverse

$$\boldsymbol{v}_d = \boldsymbol{J}^{\dagger} \dot{\boldsymbol{\sigma}}_d \tag{6.3}$$

Time integration of the velocity reference would yield the desired position. However, discrete-time integration would cause numerical drift in the reconstructed position. This can be counteracted by instead using the Closed Loop Inverse Kinematics (CLIK) solution from Chiaverini (1997)

$$\boldsymbol{v}_d = \boldsymbol{J}^{\dagger}(\dot{\boldsymbol{\sigma}}_d + \boldsymbol{\Lambda}\tilde{\boldsymbol{\sigma}}) \tag{6.4}$$

$\boldsymbol{\Lambda}$ is a constant positive-definite proportional gain matrix and $\tilde{\boldsymbol{\sigma}} = \boldsymbol{\sigma}_d - \boldsymbol{\sigma}$.

Lemma 4.1 Eek et al. (2020)**:**

A task function is defined by (6.1) with the CLIK control law (6.4). Assume that each USV follows the task velocity references perfectly, i.e. $\boldsymbol{v} = \boldsymbol{v}_d$. The, the closed-loop system is UGES if the task Jacobian is of full row rank, i.e. $\boldsymbol{J}\boldsymbol{J}^T$ is invertible.

Proof. Assuming $\boldsymbol{v} = \boldsymbol{v}_d$, (6.4) can be inserted into (6.2):

$$\dot{\boldsymbol{\sigma}} = \boldsymbol{J}\boldsymbol{v}_d = \boldsymbol{J}\boldsymbol{J}^{\dagger}(\dot{\boldsymbol{\sigma}}_d + \boldsymbol{\Lambda}\tilde{\boldsymbol{\sigma}}) \tag{6.5}$$

When the task Jacobian is of full row rank, we obtain

$$\boldsymbol{J}\boldsymbol{J}^{\dagger}\left(\boldsymbol{J}\boldsymbol{J}^{\dagger}\right)^{-1} = \boldsymbol{I} \tag{6.6}$$

Hence, we are left with the following error dynamics

$$\dot{\tilde{\boldsymbol{\sigma}}} = -\boldsymbol{\Lambda}\tilde{\boldsymbol{\sigma}} \tag{6.7}$$

which is clearly UGES for a positive definite $\boldsymbol{\Lambda}$ and the Lyapunov function candidate $V(\tilde{\boldsymbol{\sigma}}) = \frac{1}{2}\tilde{\boldsymbol{\sigma}}^T\tilde{\boldsymbol{\sigma}}$ in Khalil (2013).

□

6.1.1 Task priority control

In the case of multiple tasks, a single task of (6.4) may be written

$$\boldsymbol{v}_i = \boldsymbol{J}_i^{\dagger}(\dot{\boldsymbol{\sigma}}_{i,d} + \boldsymbol{\Lambda}_i\tilde{\boldsymbol{\sigma}}_i), \tag{6.8}$$

where i denotes the i-th priority task. For three tasks, the CLIK solution is extended to be

$$\boldsymbol{v}_d = \boldsymbol{v}_1 + (\boldsymbol{I} - \boldsymbol{J}_1^{\dagger}\boldsymbol{J}_1)[\boldsymbol{v}_2 + (\boldsymbol{I} - \boldsymbol{J}_2^{\dagger}\boldsymbol{J}_2)\boldsymbol{v}_3] \tag{6.9}$$

I is the identity matrix of appropriate dimensions. The lower-priority task velocities are projected onto the null-space of the higher-priority task velocities. This causes velocity components conflicting with higher-priority references to be removed. Hence, given a non-singular configuration, the highest-priority task is always fulfilled, whereas the lower-priority tasks are fulfilled only in the subspace where they do not conflict with higher-priority tasks. Therefore, each task reaches a sub-optimal solution by respecting the constraints imposed by the higher-priority tasks.

6.1.2 Maneuvering control for USVs

The NSB algorithm provides a velocity reference vector in the inertial frame. In order to get a desired course and surge velocity we decompose the vector

$$U_{i,NSB} = ||\boldsymbol{v}^n_{i,NSB}||_2 \tag{6.10a}$$

$$\chi_{i,NSB} = \arctan\left(\frac{v^n_{i,NSB}}{u^n_{i,NSB}}\right) \tag{6.10b}$$

where $\boldsymbol{v}^n_{i,NSB} = [u^n_{i,NSB}, v^n_{i,NSB}]^T$ is the reference velocity vector obtained in (6.9) for vessel i. This is converted to a desired surge and heading by decreasing the speed ahead of large turns and compensating for crab angle:

$$u_{i,d} = U_{i,NSB}\frac{1 + \cos(\chi_{i,NSB} - \chi_i)}{2} \tag{6.11a}$$

$$\psi_{i,d} = \chi_{i,NSB} - \arctan\left(\frac{v^b}{u_d}\right) \tag{6.11b}$$

Note that the last term of (6.11b) is the desired crab angle, which is the angle between the surge velocity and the total speed when $u = u_d$. These references for surge velocity and heading can be directly fed into our autopilot controllers which set appropriate demands to the water jets.

6.2 Tasks

The following three tasks are defined in descending order of priority:

1. Inter-vessel collision avoidance.
2. Formation driving.
3. Barycenter path following with obstacle collision avoidance.

The inter-vessel collision avoidance has the highest priority due to the critical consequence of the task not being accomplished. The formation driving task aims to keep a specific relative position between the vehicles. The barycenter path following task makes the average position of the vehicles, called the barycenter, follow a predefined path. The three tasks with the barycenter path following method developed in

Eek et al. (2020) will be used, but with collision avoidance embedded in the reference trajectory generation. This is similar to the collision and depth-limiting integration in the NSB scheme for autonomous underwater vehicles in Matouš et al. (2023).

6.2.1 Inter-vessel collision avoidance

The inter-vessel collision avoidance task is defined as the Euclidean distance between the two vessels:

$$\sigma_o = ||\boldsymbol{p}_i - \boldsymbol{p}_o||_2 \tag{6.12}$$

$\boldsymbol{p}_i$ is the position of vessel i and $\boldsymbol{p}_o$ is the position of the other vessel. The inter-vessel collision avoidance is only activated when the vessels are closer to each other than a certain distance, denoted d_o. This threshold is equal to the desired distance between the vessels:

$$\sigma_{o,d} = d_o \tag{6.13}$$

This implies that $\dot{\sigma}_{o,d} = 0$ since the distance will remain fixed, which simplifies (6.4) to

$$\boldsymbol{v}_{o,d} = \boldsymbol{J}_o^{\dagger} \boldsymbol{\Lambda}_o \tilde{\boldsymbol{\sigma}}_o \tag{6.14}$$

The task Jacobian is derived to be

$$\begin{aligned} \boldsymbol{J}_o &= \frac{\partial \sigma_o}{\partial \boldsymbol{p}} = \frac{\partial}{\partial \boldsymbol{p}} ||\boldsymbol{p}_i - \boldsymbol{p}_o||_2 = \frac{\partial}{\partial \boldsymbol{p}} \sqrt{(x_i - x_o)^2 + (y_i - y_o)^2} \\ &= \frac{1}{\sqrt{(x_i - x_o)^2 + (y_i - y_o)^2}} \begin{bmatrix} x_1 - x_2, & y_1 - y_2, & x_2 - x_1, & y_2 - y_1 \end{bmatrix} \\ &= \frac{(\boldsymbol{p}_i - \boldsymbol{p}_o)^T}{||\boldsymbol{p}_i - \boldsymbol{p}_o||_2} \end{aligned} \tag{6.15}$$

6.2.2 Formation driving

The formation driving task is defined as the difference in position from vessel 1 to the barycenter position:

$$\boldsymbol{\sigma}_f = \boldsymbol{p}_1 - \boldsymbol{p}_b = \boldsymbol{p}_1 - \frac{1}{2}(\boldsymbol{p}_1 + \boldsymbol{p}_2) = \frac{1}{2}(\boldsymbol{p}_1 - \boldsymbol{p}_2) \tag{6.16}$$

For mine sweeping and formation dricing, it is desirable that the vessels keep a fixed cross-track distance tangential to the barycenter reference path. Hence, the desired distances between the vessels are defined in the path tangential frame p:

$$\boldsymbol{\sigma}^p_{f,d} = \begin{bmatrix} 0 & \pm d_f \end{bmatrix} \tag{6.17a}$$

$$\boldsymbol{\sigma}_{f,d} = \boldsymbol{R}(\gamma_p(\theta))\boldsymbol{\sigma}^p_{f,d} \tag{6.17b}$$

$\gamma_p(\theta)$ is the path-tangential angle. The gain coefficients are specified in the path frame before they are rotated to NED to penalize the along-track and cross-track distances directly:

$$\boldsymbol{\Lambda}_f = \boldsymbol{R}(\gamma_p(\theta))\boldsymbol{\Lambda}^p_f \tag{6.18}$$

Also here the desired task variables are constant such that $\dot{\sigma}_{f,d} = 0$. Following the rotations, the expression for finding a velocity reference becomes

$$\boldsymbol{v}_{f,d} = \boldsymbol{J}^\dagger_f \boldsymbol{R}(\gamma_p(\theta))\boldsymbol{\Lambda}^p_f \tilde{\boldsymbol{\sigma}}^p_f = \boldsymbol{J}^\dagger_f \boldsymbol{\Lambda}_f \tilde{\boldsymbol{\sigma}}^p_f \tag{6.19}$$

Note that $\boldsymbol{\sigma}^p_f$ is included in $\tilde{\boldsymbol{\sigma}}^p_f$ prior to rotation to NED:

$$\boldsymbol{\sigma}^p_f = \boldsymbol{R}(\gamma_p(\theta))^T \boldsymbol{\sigma}_f \tag{6.20}$$

The task Jacobian is

$$\boldsymbol{J}_f = \frac{1}{2}\begin{bmatrix} 1 & 0 & -1 & 0 \\ 0 & 1 & 0 & -1 \end{bmatrix} \tag{6.21}$$

Proposition 4.1 (Eek et al.; 2020) **:**

The task function (6.16) has the task Jacobian (6.21). Assume that each USV follows the task velocity references perfectly, i.e. $\boldsymbol{v} = \boldsymbol{v}_d$. Then, the conditions of Lemma 4.1 are fulfilled for the task Jacobian such that the formation task error dynamics is UGES.

Proof. The Jacobian (6.21) is of full row rank. Hence,

$$\boldsymbol{J}_f \boldsymbol{J}_f^T = \frac{1}{2}^2 \begin{bmatrix} 1 & 0 & -1 & 0 \\ 0 & 1 & 0 & -1 \end{bmatrix} \begin{bmatrix} 1 & 0 \\ 0 & 1 \\ -1 & 0 \\ 0 & -1 \end{bmatrix} = \frac{1}{2} \begin{bmatrix} 1 & 0 \\ 0 & 1 \end{bmatrix} = \frac{1}{2} \boldsymbol{I}_{2x2} \tag{6.22}$$

which is invertible. Hence the conditions of Lemma 4.1 are fulfilled and UGES is concluded.

□

6.2.3 Barycenter path following and obstacle collision avoidance

The barycenter path following task is based on the LOS path following done in Eek et al. (2020). The objective is to make the barycenter follow a desired path while maintaining a desired speed tangential to the path. The path P is parameterized using the path variable $\theta \in \mathbb{R}$ with respect to the inertia frame. The path following errors are then given as

$$\begin{bmatrix} x_{pb}^p \\ y_{pb}^p \end{bmatrix} = \boldsymbol{R}(\gamma_p(\theta))^T \begin{bmatrix} x_b^n - x_p^n(\theta) \\ y_b^n - y_p^n(\theta) \end{bmatrix} \tag{6.23}$$

$[x_b^n, y_b^n]$ denotes the barycenter position, and $[x_p^n(\theta), y_p^n(\theta)]$ is its desired position. These positions are defined in NED. By rotating this to the path tangential frame, we obtain the path following errors x_{pb}^p and y_{pb}^p given as along-track and cross-track errors, respectively. The objective is to make these errors converge to zero, as we want the barycenter to follow the desired path. Figure 6.1 shows an illustration of the coordinate frames and the path following errors.

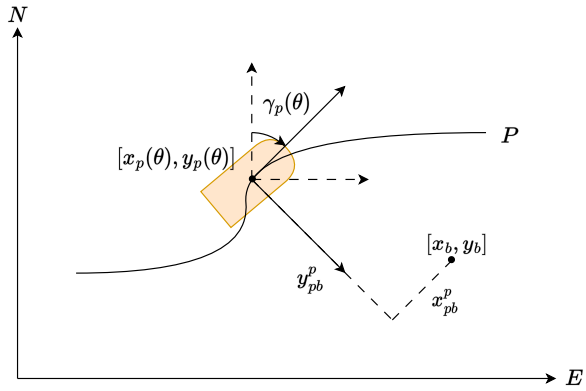

Figure 6.1: Barycenter path following errors.

The barycenter is defined as the average position of the vessels:

$$\boldsymbol{p}_b = \frac{1}{2}(\boldsymbol{p}_1 + \boldsymbol{p}_2) \tag{6.24}$$

Its derivative is given as

$$\dot{\boldsymbol{p}}_b = \frac{1}{2}(\dot{\boldsymbol{p}}_1 + \dot{\boldsymbol{p}}_2) \tag{6.25}$$

On component form, we get the following by inserting the kinematics from (3.8):

$$\dot{x}_b = \frac{1}{2}\left[u_1 \cos(\psi_1) - v_1 \sin(\psi_1) + u_2 \cos(\psi_2) - v_2 \sin(\psi_2)\right] \tag{6.26a}$$

$$\dot{y}_b = \frac{1}{2}\left[u_1 \sin(\psi_1) + v_1 \cos(\psi_1) + u_2 \sin(\psi_2) + v_2 \cos(\psi_2)\right] \tag{6.26b}$$

u_i, v_i and ψ_i are the surge velocity, sway velocity and the heading of vessel i.
The component form of the barycenter path following errors dynamic is

$$x^p_{pb} = (x^n_b - x_p(\theta))\cos(\gamma_p(\theta)) + (y^n_b - y_p(\theta))\sin(\gamma_p(\theta)) \tag{6.27a}$$

$$y^p_{pb} = -(x^n_b - x_p(\theta))\sin(\gamma_p(\theta)) + (y^n_b - y_p(\theta))\cos(\gamma_p(\theta)) \tag{6.27b}$$

Inserting (6.26) into the derivative of (6.27) and rearranging the terms yields

$$\dot{x}_{pb}^{p} = \frac{1}{2}U_1 \cos(\chi_1 - \gamma_p(\theta)) + \frac{1}{2}U_2 \cos(\chi_2 - \gamma_p(\theta)) - \dot{\theta}(1 - \kappa(\theta))y_{pb}^{p} \tag{6.28a}$$

$$\dot{y}_{pb}^{p} = \frac{1}{2}U_1 \sin(\chi_1 - \gamma_p(\theta)) + \frac{1}{2}U_2 \sin(\chi_2 - \gamma_p(\theta)) - \dot{\theta}\kappa(\theta)x_{pb}^{p} \tag{6.28b}$$

χ_i and U_i are the course and the speed of vessel i, and κ is the curvature of path P.

6.2.3.1 Path parametrization

The parametrization of the path provides an extra degree of freedom in choosing an update law for the path parameter. The update law is chosen to obtain fast convergence of the path following errors to zero. Cancellation of the undesired terms in (6.28a) is performed to ensure convergence of the along-track errors, as suggested in Belleter et al. (2019). The update law is

$$\dot{\theta} = \frac{1}{2}U_1 \cos(\chi_1 - \gamma_p(\theta)) + \frac{1}{2}U_2 \cos(\chi_2 - \gamma_p(\theta)) + k_\theta f_\theta \left(x_{pb}^{p}\right) \tag{6.29}$$

$k_\theta \in \mathbb{R}_{>0}$ and $f_\theta : \mathbb{R}^2 \to \mathbb{R}_{>0}$ is a control gain and a function of convergence of the along-track error x_{pb}^{p}. The function of convergence is

$$f_\theta \left(x_{pb}^{p}\right) = \frac{x_{pb}^{p}}{\sqrt{1 + \left(x_{pb}^{p}\right)^2}} \tag{6.30}$$

Hence, by inserting the update law into (6.28a), the following along-track error dynamics is obtained:

$$\dot{x}_{pb}^{p} = -k_\theta \frac{x_{pb}^{p}}{\sqrt{1 + \left(x_{pb}^{p}\right)^2}} + \dot{\theta}\kappa(\theta)y_{pb}^{p} \tag{6.31}$$

6.2.3.2 Guidance law

The velocity reference for the path following problem is given as

$$\boldsymbol{\nu}_{b,d} = \begin{bmatrix} U_d \cos(\chi_{b,d}) \\ U_d \sin(\chi_{b,d}) \end{bmatrix} \tag{6.32}$$

U_d is the desired along-track speed and can be chosen freely. $\chi_{b,d}$ is the desired course. This is set according to the LOS guidance law:

$$\chi_{b,d} = \gamma_p(\theta) - \arctan\left(\frac{y^p_{pb}}{\Delta\left(\boldsymbol{p}^p_{pb}\right)}\right) \tag{6.33}$$

The first term is the path-tangential angle which the barycenter aims to follow. The second term is the velocity-path relative angle used to steer the barycenter towards the point ahead on the path defined by the lookahead distance $\Delta(\boldsymbol{p}^p_{pb})$. This is defined to be

$$\Delta\left(\boldsymbol{p}^p_{pb}\right) = \sqrt{\mu + \left(x^p_{pb}\right)^2 + \left(y^p_{pb}\right)^2} \tag{6.34}$$

$\mu > 0$ is a constant parameter. When the barycenter is far from the desired point on the path, the lookahead distance is larger to ensure a smooth convergence. When the distance is shorter, the lookahead distance decreases accordingly such that the barycenter position converges faster to the point on the path. The intuition behind the tuning of μ is similar: Setting it large will ensure smooth convergence as the lookahead distance is always large. Setting it lower will allow faster convergence, at the cost of causing small oscillations of the barycenter around the path.

Now, when the desired LOS course is defined, the heading is found to be

$$\psi_{i,d} = \chi_{b,d} - \beta_{i,d} = \chi_{b,d} - \arctan\left(\frac{v^b_i}{u_{i,d}}\right) \tag{6.35}$$

$\beta_{i,d}$ is the desired crab angle for vessel i, given by the desired path following

surge velocity and the current sway velocity. Substituting (6.35) into (6.28b) yields the following dynamics for the cross-track error

$$\begin{aligned}\dot{y}^p_{pb} =& \frac{1}{2}U_{d,1}\sin\left(\psi_{d,1}+\tilde{\psi}_1+\beta_{d,1}-\gamma_p\right)\\ &+\frac{1}{2}U_{d,2}\sin\left(\psi_{d,2}+\tilde{\psi}_2+\beta_{d,2}-\gamma_p\right)\\ &-\kappa(\theta)\dot{\theta}x^p_{pb}\\ &+\frac{1}{2}(\tilde{u}_1\sin(\psi_1-\gamma_p)+\frac{1}{2}(\tilde{u}_2\sin(\psi_2-\gamma_p)\\ =&-\frac{1}{2}(U_{d,1}+U_{d,2})\frac{y^p_{pb}}{\sqrt{\Delta^2+\left(y^p_{pb}\right)^2}}\\ &-\kappa(\theta)\dot{\theta}x^p_{pb}+G_1\left(\tilde{\psi}_1,\tilde{u}_1,\psi_{d,1},U_{d,1},\tilde{\psi}_2,\tilde{u}_2,\psi_{d,2},U_{d,2},y^p_{pb}\right)\end{aligned} \tag{6.36}$$

$U_{d,i}=\sqrt{u^2_{d,i}+v^2_i}$ is the desired total speed of vessel i, while $\tilde{\psi}_i=\psi_i-\psi_{d,i}$ and $\tilde{u}_i=u_i-u_{d,i}$ are error states for the heading and the surge velocity. $G_1(\cdot)$ is a perturbing term:

$$G_1(\cdot)=\frac{1}{2}G_2\left(\tilde{\psi}_1,\tilde{u}_1,\psi_{d,1},U_{d,1},y^p_{pb}\right)+\frac{1}{2}G_2\left(\tilde{\psi}_2,\tilde{u}_2,\psi_{d,2},U_{d,2},y^p_{pb}\right) \tag{6.37}$$

where

$$\begin{aligned}G_2\left(\tilde{\psi},\tilde{u},\psi_d,U_d,y^p_{pb}\right)=&U_d(1-\cos(\tilde{\psi})\sin\left(\arctan\left(\frac{y^p_{pb}}{\Delta}\right)\right)+\tilde{u}\sin(\psi-\gamma_p)\\ &+U_d\cos\left(\arctan\left(\frac{y^p_{pb}}{\Delta}\right)\right)\sin(\tilde{\psi})\end{aligned} \tag{6.38}$$

$G_1(\cdot)$ satisfies

$$G_1\left(0,0,\psi_{d,1},U_{d,1},0,0,\psi_{d,2},U_{d,2},y^p_{pb}\right)=0 \tag{6.39a}$$

$$||G_1(\cdot)|| \leq \zeta_1(U_{d,1}, U_{d,2})|| \begin{bmatrix} \tilde{\psi}_1 & \tilde{u}_1 & \tilde{\psi}_2 & \tilde{u}_2 \end{bmatrix}^T || \tag{6.39b}$$

where $\zeta_1(U_{d,1}, U_{d,2}) > 0$. Hence, $G_1(\cdot) = 0$ when the perturbing variables are zero, and it has maximal linear growth in the perturbing states.

Proposition 4.2 (Eek et al.; 2020) **:**

A parameterized path $P(\theta) = [x_p(\theta), y_p(\theta)]$ has the θ update law (6.29) and a system consisting of two vessels with the barycenter kinematics in (6.26). Assume that both vessels track the guidance law reference in (6.33) perfectly, such that $\tilde{\psi}_i = \tilde{u}_i = 0$ for $i = \{1, 2\}$. Then, the origin of (6.31), (6.36) is a uniformly semi-global stable (USGES) equilibrium point.

Proof. This proof is taken from Eek et al. (2020), who used results for Lyapunov sufficient conditions for USGES from Pettersen (2017).

Using $\tilde{\psi}_i = \tilde{u}_i = 0$ together with (6.39a) for the perturbing term $G_1(\cdot)$, we obtain the following simplified cross-track error dynamics from (6.36):

$$\dot{y}^p_{pb} = -\frac{1}{2}(U_{d,1} + U_{d,1}) \frac{y^p_{pb}}{\sqrt{\Delta^2 + \left(y^p_{pb}\right)^2}} - \kappa(\theta)\dot{\theta}x^p_{pb} \tag{6.40}$$

Then, the following Lyapunov Function Candidate is chosen:

$$V_{p^p_{pb}} = \frac{1}{2}\left(x^p_{pb}\right)^2 + \frac{1}{2}\left(y^p_{pb}\right)^2 \tag{6.41}$$

Taking the derivative of this along the trajectories of (6.31) and (6.40) yields

$$
\begin{aligned}
\dot{V}_{p_{pb}^p} =& \dot{x}_{pb}^p x_{pb}^p + \dot{y}_{pb}^p y_{pb}^p \\
=& x_{pb}^p \left(-k_\theta \frac{x_{pb}^p}{\sqrt{1 + \left(x_{pb}^p\right)^2}} + \dot{\theta}\kappa(\theta) y_{pb}^p) \right) \\
&+ y_{pb}^p \left(-\frac{1}{2}(U_{d,1} + U_{d,1}) \frac{y_{pb}^p}{\sqrt{\Delta^2 + \left(y_{pb}^p\right)^2}} - \kappa(\theta)\dot{\theta} x_{pb}^p \right) \\
=& - k_\theta \frac{\left(x_{pb}^p\right)^2}{\sqrt{1 + \left(x_{pb}^p\right)^2}} - \frac{1}{2}(U_{d,1} + U_{d,2}) \frac{\left(y_{pb}^p\right)^2}{\sqrt{\Delta^2 + \left(y_{pb}^p\right)^2}}
\end{aligned}
\tag{6.42}
$$

This is negative definite, implying that a uniformly global asymptotically stable (UGAS) equilibrium in the error dynamics can be concluded from the definition in Khalil (2013).

Now, error variables are defined as

$$
\boldsymbol{e} = \begin{bmatrix} e_1 \\ e_2 \end{bmatrix} = \begin{bmatrix} x_{pb}^p \\ y_{pb}^p \end{bmatrix} \tag{6.43}
$$

Substituting the lookahead distance (6.34) and the error variables (6.43) in the LFC derivative in (6.42) with $V_{p_{pb}^p}$ denoted as V yields

$$
\begin{aligned}
\dot{V} &= -k_\theta \frac{e_1^2}{\sqrt{1 + e_1^2}} - \frac{1}{2}(U_{d,1} + U_{d,2}) \frac{e_2^2}{\sqrt{\mu + e_1^2 + 2e_2^2}} \\
&= \boldsymbol{e}^T \boldsymbol{Q} \boldsymbol{e}
\end{aligned}
\tag{6.44}
$$

with

$$\boldsymbol{Q} = \begin{bmatrix} \frac{k_\theta}{\sqrt{1+e_1^2}} & 0 \\ 0 & \frac{1}{2}\frac{U_{d,1}+U_{d,2}}{\sqrt{\mu+e_1^2+2e_2^2}} \end{bmatrix} \tag{6.45}$$

For $k_\theta, U_{d,1}, U_{d,2} > 0$, $\boldsymbol{Q}$ is positive definite. Consequently, the LFC derivative is upper bounded by

$$\dot{V} \leq -q_{min}||\boldsymbol{e}||^2, \forall \boldsymbol{e} \in \mathcal{B}_r \tag{6.46}$$

with

$$q_{min} \triangleq \lambda_{min}\left(\begin{bmatrix} \frac{k_\theta}{\sqrt{1+r^2}} & 0 \\ 0 & \frac{1}{2}\frac{U_{d,1}+U_{d,2}}{\sqrt{\mu+3r^2}} \end{bmatrix}\right) \tag{6.47}$$

for any ball

$$\mathcal{B}_r \triangleq \{\max\{|e_1|, |e_2|\} < r\}, r > 0 \tag{6.48}$$

and with $\lambda_{min}(\boldsymbol{A})$ defined as the minimum eigenvalue of a matrix $\boldsymbol{A}$. Thus, all the sufficient conditions in Theorem 5 of Pettersen (2017) are fulfilled with $k_1 = k_2 = \frac{1}{2}$, $a = 2$ and $k_3 = q_{min}$ such that USGES can be concluded for the origin of (6.31), (6.40), given the conditions in this proposition.

□

In addition to the USGES in the isolated barycenter path following task, the following proposition from Eek et al. (2020) regarding the combined formation and barycenter path following tasks is also of particular interest. But before stating it, the task Jacobian $\boldsymbol{J}_b$ of the barycenter path following task is found. As this is not defined as a CLIK task directly, we do not have a task variable to differentiate. However, by calculating the Jacobian of (6.24) and inverting (6.25) we can obtain the mapping of the barycenter to each vessel:

$$\boldsymbol{J}_b = \frac{1}{2}\begin{bmatrix} 1 & 0 & 1 & 0 \\ 0 & 1 & 0 & 1 \end{bmatrix} \tag{6.49}$$

Proposition 4.3 (Eek et al.; 2020) **:**

The formation and barycenter path following tasks from Section 6.2.2 and Section 6.2.3 are combined with the null-space projection in (6.9). Assume that the velocity references $\boldsymbol{v}_d$ are followed perfectly, i.e. $\boldsymbol{v} = \boldsymbol{v}_d$. Then, the system of these two tasks is UGAS and both tasks' errors converge asymptotically to zero.

Proof. According to the stability property analysis of combined task solutions in Antonelli et al. (2008), a two-task system must have orthogonal tasks to be asymptotically stable. The task Jacobians are given by (6.21) and (6.49), and orthogonality between them is proven:

$$\boldsymbol{J}_f \boldsymbol{J}_b^{\dagger} = \boldsymbol{J}_f (\boldsymbol{J}_b^T \boldsymbol{J}_b)^{-1} \boldsymbol{J}_b^T = \boldsymbol{0}_{2x2} \tag{6.50}$$

$\boldsymbol{0}_{2x2}$ is the $2x2$ null matrix. Thus, the task errors are asymptotically stable and the system is UGAS. This was also shown in Antonelli et al. (2008)

□

6.2.3.3 Obstacle collision avoidance

The collision avoidance task presented in Section 6.2.1 only concerns the inter-vessel case, meaning that there is still no dedicated task that aims to prevent collisions with observed obstacles or other vehicles at sea. For the mine sweep applications of FFI, the USVs will keep a distance above the activation limit of the inter-vessel collision avoidance module. Propositions 4.1-4.3 ensure that both the merged formation and barycenter path following task and the individual tasks themselves are at least UGAS and that the task errors converge to zero. Consequently for the FFI operations, task errors will converge to zero. This property is desirable to preserve for collision avoidance. Therefore, the collision avoidance algorithm presented in Chapter 5 is integrated into the path following task, where the reference path for the barycenter is

updated to follow the constant avoidance angle when the USVs are on collision course with an obstacle. For the obstacle collision avoidance, the two USVs are treated as one system to fit into the barycenter path following task: The center of the system is the barycenter position of the USVs, while the radius is the half of the distance between the USVs. Similarly, the velocity is the average of the USV velocities. The collision avoidance calculations concerning one USV in the body frame in Chapter 5 are converted to the the barycenter body frame, and the desired course angle to follow is tracked by updating the barycenter path to follow a straight line segment with this angle. The method also has the benefit of being extendable to arbitrary many boats by finding average positions and velocities and using them as system parameters.

An alternative approach could be to implement the obstacle collision avoidance as a dedicated task with the highest priority, as Arrichiello et al. (2006). However, NSB intrinsically requires a differentiable analytic expression of the tasks defined so that it is possible to compute the required Jacobians. A COLREGs compliant collision avoidance algorithm will have no such expression, such that instead a set based approach might be used for each COLREGs scenario. Hence, the transitions between course angle neighboring COLREGs scenarios also needs to be taken care of. Moreover, the collision avoidance task is dependent of both the positions and velocities of both the USVs and the obstacle. This approach also requires more task stability analysis as a new task is introduced. Here, care should be taken to ensure that the stability properties and the task error convergence of all tasks persist. However, due to the complexity and potential lack of stability preservation of the approach, this was not further considered.

Before explaining how the path is updated when obstacles are present, the trajectory generation method is introduced.

6.3 Trajectory generation

The trajectory generation is divided into two parts: Generation in the absence and presence of obstacles. Without obstacles, pure waypoint based trajectory generation is implemented. When the barycenter is on collision course with an obstacle, the waypoint trajectory generation is overridden by a trajectory following the constant

avoidance angle. Here, two different suggestions are presented.

6.3.1 Waypoint trajectory generation

The input to the guidance scheme is a route of desired locations for the barycenter to pass by. The barycenter LOS law presented above requires a parameterized path and the path angle given the parameter θ value.

A list of k waypoint positions in the inertial frame is given:

$$W = \left\{(x_0^n, y_0^n), (x_1^n, y_1^n), ..., (x_k^n, y_k^n)\right\} \tag{6.51}$$

One of the most used path generation methods is the straight-lines based circles of acceptance method (Fossen (2011)). This is computationally cheap and very intuitive. Consider point i in the list from (6.51). This is a location which was last reached by the barycenter ($(x_i, y_i) = (0, 0)$ is the initial position of the path). Hence, the path from point i to point $i + 1$ is defined to be:

$$\begin{bmatrix} x_p \\ y_p \end{bmatrix} = \frac{\theta}{\sqrt{(x_{i+1} - x_i)^2 + (y_{i+1} - y_i)^2}} \begin{bmatrix} x_{i+1} - x_i \\ y_{i+1} - y_i \end{bmatrix} + \begin{bmatrix} x_i \\ y_i \end{bmatrix} \tag{6.52}$$

The angle of the path is given by

$$\gamma_p = \arctan\left(\frac{\frac{\partial x_p}{\partial \theta}}{\frac{\partial y_p}{\partial \theta}}\right) = \arctan\left(\frac{1}{\sqrt{(x_{i+1} - x_i)^2 + (y_{i+1} - y_i)^2}} \frac{x_{i+1} - x_i}{y_{i+1} - y_i}\right) \tag{6.53}$$

A point i is defined to be reached when the barycenter is sufficiently close to it, determined by the radius in the circle of acceptance for the given point:

$$(x_i - x_b^n)^2 + (y_i - y_b^n)^2 \leq R_i^2 \tag{6.54}$$

This method has the drawback that a too small circle of acceptance may cause the USVs to have a too large cross-track error when passing the waypoint. Thus, the switching criterion is never satisfied and the USVs will continue driving on the

line defined by the two waypoints. This problem can be circumvented by choosing a switching rule which solely depends on the along-track distance of the USVs with respect to point i:

$$\sqrt{(x_{i+1} - x_i)^2 + (y_{i+1} - y_i)^2} - |x_{p,i}^e| \leq R_{switch} \tag{6.55}$$

6.3.2 Collision avoidance trajectory generation

When the criteria in (5.12) are satisfied, the system activates collision avoidance mode and the path is updated accordingly. For this project, two different path update approaches are suggested.

6.3.2.1 Suggestion 1

A first suggestion, used in the experiments in Chapter 9, was to start a new path from the current barycenter point and follow the constant avoidance angle given by the collision avoidance algorithm. The updated path starts to ensure zero path following errors in the moment of entrance to the collision avoidance mode. The path is updated to be

$$\begin{bmatrix} x_p \\ y_p \end{bmatrix} = (\theta - \theta_{entrance}) \begin{bmatrix} \cos(\gamma_{ca}) \\ \sin(\gamma_{ca}) \end{bmatrix} + \begin{bmatrix} x_b^n \\ y_b^n \end{bmatrix} \tag{6.56}$$

γ_{ca} is the constant avoidance angle provided by the algorithm in Chapter 5, θ is the path parameter and $\theta_{entrance}$ is the value of θ when entering the collision avoidance mode. The $\theta_{entrance}$ value is used to make sure that the new desired path starts at the barycenter without resetting θ. When the barycenter is following the constant avoidance angle path, the path parameter θ will continue to grow due to the θ update law in (6.29). θ will grow with the along-track error in the last term of the update law. Therefore, θ will wait for the USVs to adjust their courses, and the desired path coordinate will continue to follow the path when the barycenter adjusts to the new course. When all obstacles are out of the collision cones, the vessels can get back to following the original path in (6.52) (see left part of Figure 6.2). Note that the path is

now further ahead than when the vessels entered collision avoidance mode, since we let θ continue growing. Assuming that the barycenter reaches the constant avoidance angle path with small task errors, θ have increased to move the current path coordinate point ahead with a length equal to the length of the constant avoidance angle path. Since this path is a turn away from the original path, the desired path coordinate will be ahead of the barycenter when exiting collision avoidance. This is because the along-track distance on the waypoint path with the current θ value is further ahead than the projection of the constant avoidance angle path on the original path. Thus, a turn back to the point where the barycenter left off is not needed, and the barycenter will continue moving forward in the along-track direction of the orignal path while converging towards it.

6.3.2.2 Suggestion 2

The path update in the first suggestion causes discontinuities in the transitions of the collision avoidance mode. In particular, when exiting the collision avoidance mode, the constant avoidance angle path has diverged from the waypoint path. Hence, large path following erros might occur. Moreover, despite starting the path in the barycenter when entering collision avoidance mode, the course discrepancy from the path reference will cause increasing path following errors once the path is updated in the first iteration. Therefore, a second suggestion is to start the constant avoidance angle path where the path was last updated:

$$\begin{bmatrix} x_p \\ y_p \end{bmatrix} = \theta \begin{bmatrix} \cos(\gamma_{ca}) \\ \sin(\gamma_{ca}) \end{bmatrix} + \begin{bmatrix} x_{p,entrance} \\ y_{p,entrance} \end{bmatrix} \tag{6.57}$$

This ensures that the the path is continuous in the transitions to and from collision avoidance mode. Also note that the $(\theta - \theta_{entrance})$ term is replaced with θ because θ is now instead set to zero at the beginning of the collision avoidance maneuver.

When exiting collision avoidance mode and getting back to waypoint tracking, the first update rule suggested to preserve the θ value. Now, instead of getting back to the path between the last and the next waypoint, a new path is generated from the point

where collision avoidance mode was exited to the next waypoint. Figure 6.2 shows the two different approaches.

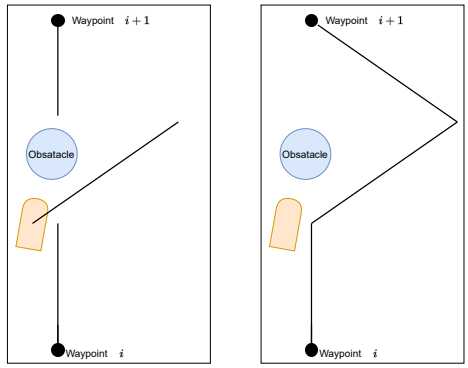

Figure 6.2: Suggestions of path update methods in the collision avoidance mode transitions. Left: The first suggestion used in experiments. Right: The second suggestion to be used with inscribed circles in simulations.

Despite having a continuous path and keeping path following errors low in the collision avoidance transitions, one problem arises when using the second path update suggestion. For mine sweeping, it is of interest that the mine sweep system covers the whole path between waypoints. Obviously, this is impossible with obstacles present, but as soon as the a collision is prevented, the USVs should get back to the desired path as soon as possible. The second path update suggestion instead creates a new path to the next waypoint. If the distance between two waypoints is large, the USVs will therefore follow a path which was not predefined. However, this issue could be circumvented by adding more waypoints to the predefined path, such that the line segments from exiting collision avoidance to the next waypoint is as small as possible.

6.3.3 Inscribed circles

Although the generated path is continuous for every point, the path is non-smooth in the transitions of the collision avoidance mode. Smoothness of the path was assumed in its definition, such that the time differentiated path following errors in (6.31) and (6.40)

are well defined. This is important, as they are used in Proposition 4.3 for ensuring task UGAS and error convergence in the path following task. Moreover, the discontinuities lead to steps in the heading references. We suggest using a variant of inscribed circles when the heading reference is changed, based on the method described in Fossen (2011). But instead of letting waypoint positions determine the inscribed circle radius, we set a fixed radius for every turn. This radius could be adjusted depending on the system dynamics to accommodate for maneuvering limitations. Hence, we can control the turning radius directly to ensure a safe mine sweep operation.

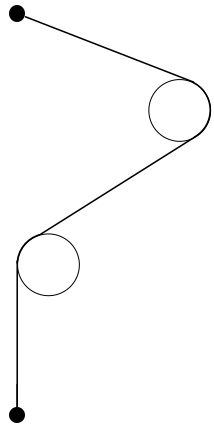

Figure 6.3: Path updates with inscribed circles.

The inscribed circles method is illustrated in Figure 6.3. The path is equal to the path update suggestion to the right in Figure 6.2, but with modifications in the turning maneuver. When a new heading reference is provided, the inscribed circle center is defined to be

$$\begin{bmatrix} x_c \\ y_c \end{bmatrix} = \begin{bmatrix} x_p \\ y_p \end{bmatrix} + R_c \begin{bmatrix} \cos(\gamma_c) \\ \sin(\gamma_c) \end{bmatrix} \tag{6.58a}$$

$$\gamma_c = \gamma_p + \frac{\pi}{2}\text{sgn}(\gamma_{new} - \gamma_p) \tag{6.58b}$$

R_c is the inscribed circle radius set based on the turning capabilities of the USVs when dragging the mine sweep system. γ_c is the path angle from the current path point $[x_p, y_p]^T$ to the circle center. The circle center is perpendicular to the path, and it is located on a side determined by the turning direction. A left turn would put the circle center to the left of the path, and a right turn would put it to the right. γ_{new} denotes the new angle path angle after turning. It will be the constant avoidance angle when entering collision avoidance mode, and the angle from the path to the next waypoint when entering normal path following without obstacles. Starting from the current path position, the circular path is parameterized to be

$$\begin{bmatrix} x_p \\ y_p \end{bmatrix} = \begin{bmatrix} x_c \\ y_c \end{bmatrix} + R_c \begin{bmatrix} \cos(\xi_c) \\ \sin(\xi_c) \end{bmatrix} \tag{6.59a}$$

$$\xi_c = \gamma_{p,entrance} + \text{sgn}(\gamma_{new} - \gamma_{p,entrance})(-\frac{\pi}{2} + \theta f_c) \tag{6.59b}$$

The turning angle ξ_c is determined by the path angle $\gamma_{p,entrance}$ when entering the inscribed circle path following. Then, the turning direction is found by comparing the path angle value prior to the turn and the new desired path angle value. θ is reset in the beginning of the turn such that the path is continuous, and f_c is the update frequency of the circular path following. As for the inscribed circle radius R_c, this is a parameter that can be tuned based on the USV system dynamics. The circular path following continues until the path angle is identical to the straight line path following value. In practice, the circular path following exits when this deviation is sufficiently small:

$$|\gamma_p - \gamma_{new}| < \epsilon_c \tag{6.60}$$

ϵ_c is a small constant set in advance.

An issue worth addressing with this approach is the following: The desired path value at the end of the turning maneuver will be different from what it was in the beginning. For the collision avoidance, the constant avoidance angle will necessarily be greater when the USVs have followed a circular path starting towards the obstacle.

Similarly for the waypoint path following after a collision avoidance maneuver. Consequently, care is taken to continuously update the new angle γ_{new} which the USVs are turning towards. For the collision avoidance task, this is particularly beneficial as we can guarantee collision avoidance given that the inscribed circle radius is large enough and that the barycenter follows the path with an upper bound on the task error perturbations. This will be elaborated in the subsequent chapter.

Chapter 7

Mathematical analysis

This chapter will prove collision avoidance with one obstacle and is restricted to one USV only. The analysis follows along the lines of Wiig et al. (2020) and Haraldsen et al. (2021) on the vessel model of Frigg and Oding. Additions to the analysis include COLREGs compliant turning maneuvers as well as the use of a heading controller with a reference model instead of a course controller with a bump function.

7.1 Collision avoidance with one obstacle for one USV

For the analysis, we assume that the actuators produce no force in the sway direction. This simplifies the model in (3.8) to

$$\dot{x} = u\cos\psi - v\sin\psi \tag{7.1a}$$

$$\dot{y} = u\sin\psi + v\cos\psi \tag{7.1b}$$

$$\dot{\psi} = r \tag{7.1c}$$

$$\dot{u} = F_u(u, v, r) + \frac{\tau_u}{m} \tag{7.1d}$$

$$\dot{v} = F_v(u, v, r) \tag{7.1e}$$

$$\dot{r} = F_r(v, r) + \frac{\tau_r}{I_z} \tag{7.1f}$$

Moreover, the following assumptions are made on the coefficients in F_u, F_v and F_r:

Assumption 7.1:

$$Y_r = N_v = X_{uuu} = Y_{vvv} = N_{rrr} = 0, \left\{Y_v, Y_{|v|v}, Y_{vvv}\right\} \in \mathbb{R}_{<0} \tag{7.2}$$

Remark: The numerical values in Appendix A shows that these assumptions are met for the model coefficients.

Hence, the function values are:

$$F_u(u, v, r) = vr + \frac{X_u u + X_{|u|u}|u|u}{m} \tag{7.3a}$$

$$F_v(u, v, r) = -ur + \frac{Y_v v + Y_{|v|v}|v|v}{m} \tag{7.3b}$$

$$F_r(v, r) = \frac{N_r r + N_{|r|r}|r|r}{I_z} \tag{7.3c}$$

Assumption 7.2:

The desired forward speed of the USV u_d is constant.

Remark: This assumption is used for simplifying derivations in the subsequent proofs. Moreover, the constant avoidance angle does not provide any reference speed, only a course. Hence, the forward speed can be controlled independently and is therefore chosen to be constant.

First, a lower bound of the distance to a static obstacle is derived when the USV is following the CAA course reference.

Lemma 7.1:

The obstacle speed from (3.20) is $u_o = 0$ and let the extra safety angle for the extended vision cone in Section 5.1 be within the interval $\alpha_o \in \left(0, \frac{\pi}{2}\right)$. Let the USV follow the path given by the course reference from the collision avoidance law in (5.10) with some speed $U_b > 0$ when $t \geq t_1$. If $d_{ob}(t_1) \geq 0$, the USV will converge to a circle C with the center at the obstacle center and radius $R_C = \frac{R_o}{\cos(\alpha_o)}$. When the USV starts

outside C at t_1, the distance between the USV and the obstacle d_{ob} is lower bounded by

$$d_{ob}(t) \geq d_{min} = \frac{R_o}{\cos(\alpha_o)} - R_o, \forall t \geq t_1 \tag{7.4}$$

Proof. The course reference $\chi_{dca}^{n(j)}$ keeps the constant avoidance angle α_o to the tangent j from the USV to the obstacle. The time derivative of d_{ob} is

$$\dot{d}_{ob} = -U_b \cos(\gamma_t + \alpha_o) \tag{7.5}$$

This can be verified geometrically in Figure 5.5. γ_t is the angle from the line between the USV and the obstacle center to the line from the USV that tangents the obstacle on edge j:

$$\gamma_t = \arcsin\left(\frac{R_o}{R_o + d_{ob}}\right), d_{ob} \geq 0. \tag{7.6}$$

The derivative of d_{ob} yields the following cases for the distance:

$$d_{ob}(t) \begin{cases} < d_{min} \implies \gamma_t + \alpha_o > \frac{\pi}{2} \implies & \dot{d}_{ob} > 0 \\ = d_{min} \implies \gamma_t + \alpha_o = \frac{\pi}{2} \implies & \dot{d}_{ob} = 0 \\ > d_{min} \implies \gamma_t + \alpha_o < \frac{\pi}{2} \implies & \dot{d}_{ob} < 0 \end{cases} \tag{7.7}$$

Hence, d_{ob} will converge to the circle with radius d_{min} given by (7.4) regardless of the initial distance $d_{ob} > 0$.

□

This lemma was also derived in Wiig et al. (2020) and Haraldsen et al. (2021) and is used for finding a lower bound of the obstacle distance when the USV starts at $d_{ob} > d_{min}$, given that the course reference is perfectly followed.

Next, an upper bound for the sway velocity is found.

Lemma 7.2: Assume that

$$|r_d(v_{sup})| < \frac{|Y_v|}{mu_d} v_{sup} \tag{7.8}$$

and let $v(t_0) < v_{sup}$. Then,

$$v(t) < v_{sup}, \forall t \geq t_0 \tag{7.9}$$

Proof. Consider the Lyapunov function candidate $V(v) = \frac{1}{2}v^2$ for vessel i (subscripts are omitted for brevity). Using Assumption 7.1 and (7.8), the time derivative of V along the solutions of (7.1e) is

$$\begin{aligned}
\dot{V} = \dot{v}v &= F_v(u_d, v, r_d)v \\
&= -u_d v r_d + \frac{Y_v v^2 + Y_{|v|v}|v|v^2}{m} \\
&= -u_d v r_d + \frac{Y_v}{m}v^2 + \frac{Y_{|v|v}}{m}|v|v^2 \\
&\leq u_d|v||r_d| - \frac{|Y_v|}{m}v^2 - \frac{\left|Y_{|v|v}\right|}{m}|v|v^2 \\
&\leq -\frac{\left|Y_{|v|v}\right|}{m}|v|v^2 < 0
\end{aligned} \tag{7.10}$$

Now, define the set

$$\Omega_v \triangleq \left\{ v \in \mathbb{R} \,|\, V \leq \frac{1}{2}v_{sup}^2 \right\} \tag{7.11}$$

This is a level set of V with the boundary $v = v_{sup}$. (7.8) ensures that $\dot{V} \leq 0$ on this boundary, implying that Ω_v is positively invariant. Hence, $|v(t_0)| < v_{sup} \implies |v(t)| < v_{sup} \forall t \geq t_0$.

□

Lemma 7.3: Consider a vehicle with the dynamic model (7.1), governed by the yaw rate and surge controller in (4.1) and the heading controller in (4.6). The vehicle enters collision avoidance mode at $t = t_1$, from where the desired heading is following the following the reference provided by (5.10). Assume that the vehicle course satisfies $\chi(t_2) = \chi_{dca}^{n(j)}(t_2)$ at $t = t_2 \geq t_1 + t_d$. Then, set $\sigma \in (0, 1)$ and assume that the distance from the vehicle to the obstacle satisfies $t_{ob}(t) > d_{safe} \forall t \geq t_1$. If all assumptions hold, the heading control saturation r_{fp} from (4.7) satisfies

$$r_{fp} \leq \sigma F_{kd} \tag{7.12}$$

where F_{kd} is defined as

$$F_{kd} = \frac{|Y_v| v_{sup}}{m u_d} - \frac{u_o}{U_{b,sup}^3 m}(|Y_v| v_{sup}^2 + |Y_{|v|v}||v_{sup}| v_{sup}^2) \tag{7.13}$$

The safety distance is lower bounded by

$$d_{safe} \geq \frac{(U_{b,sup} + u_o)^2}{U_{b,sup}} \frac{1}{(1-\sigma)F_{kd}} \tag{7.14}$$

Finally, the sway speed satisfies

$$|v(t_0)| < v_{sup} \implies |v(t)| < v_{sup} \forall t \geq t_0 \tag{7.15}$$

Proof. The proof follows along the lines of Lemma 3 in Wiig et al. (2020), but differs since we use a heading controller instead of a course controller in this project. Differentiating $\chi_{dca}^{n(j)}$ with respect to time yields

$$\dot{\psi}_{dca}^{n(j)} = \dot{\psi}_{\alpha_o}^{(j)} + \dot{\gamma}_{ca}^{(j)} \tag{7.16}$$

$\gamma_{ca}^{(j)}$ is the relative velocity compensation angle, and its time derivative is found by differentiating (5.7) (see **??** for derivation):

$$\dot{\gamma}_{ca}^{(j)} = \frac{u_o \left(U_b \dot{\psi}_{\alpha_o}^{(j)} \cos\left(\gamma_{vo}^{(j)}\right) - \dot{U}_b \sin\left(\gamma_{vo}^{(j)}\right)\right)}{U_b \sqrt{U_b^2 - u_o^2 \sin^2\left(\gamma_{vo}^{(j)}\right)}} \tag{7.17}$$

The total vehicle acceleration is found by using (7.1e) and exploiting that $\dot{u} = \dot{u}_d = 0$ by Assumption 7.2:

$$\dot{U}_b = \dot{\sqrt{u_d^2 + v^2}} = \frac{2u_d\dot{u}_d + 2v\dot{v}}{2\sqrt{u_d^2 + v^2}} = \frac{v\dot{v}}{\sqrt{u_d^2 + v^2}} = v\frac{-u_d r_d + \frac{Y_v}{m}v + \frac{Y_{|v|v}}{m}|v|v}{U_b} \tag{7.18}$$

The angle $\psi_{\alpha_o}^{(j)}$ is decomposed into (see Figure 5.5)

$$\psi_{\alpha_o}^{(j)} = \gamma_o \pm \gamma_t \pm \alpha_o \tag{7.19}$$

Since α_o is constant, the derivative becomes

$$\dot{\psi}_{\alpha_o}^{(j)} = \dot{\gamma}_o \pm \dot{\gamma}_t \tag{7.20}$$

$\dot{\gamma}_o$ is found geometrically as

$$\dot{\gamma}_o = \frac{u_o \sin(\psi_o - \gamma_o) - U_b \sin(\psi_f - \gamma_o)}{R_o + d_{ob}} \tag{7.21}$$

and $\dot{\gamma}_t$ is found to be

$$\dot{\gamma}_t = -\dot{d}_{ob}\frac{R_o}{(R_o + d_{ob})\sqrt{(R_o + d_{ob})^2 - R_o^2}} \tag{7.22}$$

with

$$\dot{d}_{ob} = u_o \cos(\psi_o - \gamma_o) - U_b \cos(\psi_f - \gamma_o) \tag{7.23}$$

Combining (7.21)-(7.23) yields

$$\begin{aligned}\dot{\psi}_{\alpha_o}^{(j)} =& \frac{U_b \sin(\gamma_o - \psi_f) - u_o \sin(\gamma_o - \psi_o)}{R_o + d_{ob}} \\ &\pm R_o \frac{U_b \cos(\gamma_o - \psi_f) - u_o \cos(\gamma_o - \psi_o)}{(R_o + d_{ob})\sqrt{d_{ob}(2R_o + d_{ob})}}\end{aligned} \tag{7.24}$$

Now, the the full expression of $\dot{\psi}_{fcda}^{(j)}$ is

$$\begin{aligned}\dot{\psi}_{dca}^{(j)} =& \frac{U_b \sin\left(\gamma_o - \psi_f\right) - u_o \sin\left(\gamma_o - \psi_o\right)}{R_o + d_{ob}} \\ & \pm R_o \frac{U_b \cos\left(\gamma_o - \psi_f\right) - u_o \cos\left(\gamma_o - \psi_o\right)}{(R_o + d_{ob})\sqrt{d_{ob}(2R_o + d_{ob})}} \\ & + \frac{u_o \left(U_b \dot{\psi}_{\alpha_o}^{(j)} \cos\left(\gamma_{vo}^{(j)}\right) - v \frac{-u_d r_d + \frac{Y_v}{m} v + \frac{Y_{|v|v}}{m} |v| v}{U_b} \sin\left(\gamma_{vo}^{(j)}\right)\right)}{U_b \sqrt{U_b^2 - u_o^2 \sin^2\left(\gamma_{vo}^{(j)}\right)}}\end{aligned} \tag{7.25}$$

When the vehicle is in collision avoidance mode, r_d is found through (4.6), which is dependent on $\dot{\psi}_d$, which is $\dot{\psi}_{dca}^{(j)}$ in the collision avoidance mode. Hence, an expression of r_d is obtained by inserting (7.25) into the control law (4.6) and rearranging the terms:

$$r_d \triangleq \frac{F_{num}}{F_{den}} \tag{7.26}$$

with

$$\begin{aligned}F_{num} \triangleq & \frac{U_b \sin\left(\gamma_o - \psi_f\right) - u_o \sin\left(\gamma_o - \psi_o\right)}{R_o + d_{ob}} \\ & \pm R_o \frac{U_b \cos\left(\gamma_o - \psi_f\right) - u_o \cos\left(\gamma_o - \psi_o\right)}{(R_o + d_{ob})\sqrt{d_{ob}(2R_o + d_{ob})}} \\ & + \frac{u_o \left(U_b \dot{\psi}_{\alpha_o}^{(j)} \cos\left(\gamma_{vo}^{(j)}\right) - \frac{\frac{Y_v}{m} v^2 + \frac{Y_{|v|v}}{m} |v| v^2}{U_b} \sin\left(\gamma_{vo}^{(j)}\right)\right)}{U_b \sqrt{U_b^2 - u_o^2 \sin^2\left(\gamma_{vo}^{(j)}\right)}} \\ & - \text{sat}(k_f \tilde{\psi}_b^n)\end{aligned} \tag{7.27}$$

and

$$F_{den} \triangleq 1 - \frac{u_o u_d v}{U_b^2 \sqrt{U_b^2 - u_o^2 \sin^2(\gamma_{vo})}} \tag{7.28}$$

(7.28) is well defined by assumption 5.1 with equation (5.5). For r_d to be well defined, we also require that $F_{den} > 0$ such that it never crosses 0. A lower bound for

(7.28) is obtained by minimizing F_{den} with respect to $\gamma_{vo}^{(j)}$:

$$F_{den} > 1 - \frac{u_{o,max} u_d |v|}{U_b^2 \sqrt{U_b^2 - u_{o,max}^2}} := F_{den,inf}(v) \tag{7.29}$$

Now, note the following:

$$\begin{aligned} F_{den,inf}(v) &= 1 - \frac{u_{o,max} u_d |v|}{U_b^2 \sqrt{v^2 + \underbrace{u_d^2 - u_{o,max}^2}_{>0}}} \\ &> 1 - \frac{u_{o,max} u_d |v|}{U_b^2 \sqrt{v^2}} = 1 - \frac{u_{o,max} u_d}{U_b^2} \\ &= 1 - \underbrace{\frac{u_{o,max} u_d}{u_d^2 + v^2}}_{<1} > 0 \end{aligned} \tag{7.30}$$

When $d_{ob} \geq d_{safe}$, an upper bound can be found for $|F_{num}| < F_{num,sup}$:

$$F_{num,sup} = \frac{u_o}{U_{b,sup}^3 m} (|Y_v| v_{sup}^2 + |Y_{|v|v}||v_{sup}| v_{sup}^2) + \frac{(U_{b,sup} + u_o)^2)}{d_{safe} U_{b,sup}} + r_{fp} \tag{7.31}$$

Since (7.29) and (7.31) are even in v and v_{sup}, respectively, the following bound can be defined for (7.26):

$$|r_d(\pm v_{sup}) < \frac{F_{num,sup}}{F_{den,inf}(v_{sup})}| \tag{7.32}$$

Inserting this into (7.8) from Lemma 2 yields the following bound for d_{safe} and r_{fp}, with F_{kd} from (7.13):

$$\frac{(U_{b,sup} + u_o)^2}{d_{safe} U_{b,sup}} + r_{fp} \leq F_{kd} \tag{7.33}$$

Inserting the parameter σ from (7.12) into this, we obtain

$$\frac{(U_{b,sup} + u_o)^2}{d_{safe} U_{b,sup}} + r_{fp} \leq \sigma F_{kd} + (1 - \sigma) F_{kd} \tag{7.34}$$

Now, (7.33) is satisfied due to (7.12) and (7.14). Furthermore, the upper bound of $|v| < v_{sup}$ is ensured by Lemma 2, which concludes the proof.

□

Lemma 7.4:

The USV is modeled by (7.1) and governed by the controllers in (4.1) and (4.6). The control scheme of the USV enters collision avoidance mode at time t_1. From then, the constant avoidance angle will be set as the reference path angle. The USV speed satisfies $U_b < U_{b,sup}$ and the the switching distance satisfies

$$d_{switch} = u_{o,max} t_\epsilon + d_{safe} + d_{turn} + d_\delta \tag{7.35}$$

where t_ϵ is the maximum amount of time the heading controller will use to make the USV converge to within ϵ rad of $\chi_{dca}^{n(j)}$:

$$t_\epsilon = t_\delta + \frac{\pi}{r_{fp}} - \frac{1}{k_f} - \frac{2 \ln\left(\frac{k_f \epsilon}{r_{fp}}\right)}{k_f}, \epsilon \in \left(0, \psi_{fp}^n\right] \tag{7.36}$$

Furthemore,

$$d_{turn} = \frac{U_{b,sup}}{\min(r_{fp}, k_f \pi)} \tag{7.37}$$

defines an upper bound for the distance covered by the USV in the $\psi(t_1)$ direction while performing a π rad turn. d_δ represents

$$d_\delta = U_{b,sup} t_\delta \tag{7.38}$$

The lower bound of the distance between the USV and the obstacle is therefore defined to be d_{safe} before the USV will converge to within ϵ rad of $\chi_{dca}^{n(j)}$.

Proof. This proof will consider the worst case scenario, which is scenario when the USV

is on collision course with the obstacle on the edge of the relative velocity compensated extended vision cone which is the opposite edge of the desired COLREGs turning direction edge. Here, the USV will first take action to turn towards the obstacle before turning out of collision course. Despite the obstacle is not meeting the USV on reciprocal courses, they are treated as if they were to be conservative. The obstacle is defined to be of infinite size such that the obstacle tangent angle is $\gamma_t = \frac{\pi}{2}$. The USV and obstacle are moving at their maximum speeds $U_b = U_{b,sup}$ and $u_o = u_{o,max}$.

When the system enters collision avoidance mode at time t_1, the USV turns towards $\chi_{dca}^{n(j)}$. This causes a step in the desired yaw rate, such that the reference model in (4.3) is smoothing the change of reference. This is done at t_δ time. The maximum course error $|\tilde{\chi}|$ at $t_1 + t_\delta$ is π due to the mapping into the interval $(-\pi, \pi]$. The convergence time is $\frac{\pi}{r_{fp}} - \frac{1}{k_f}$ from $|\tilde{\chi}| = \pi$ to $|\tilde{\chi}| = \frac{r_{fp}}{k_f}$ by the definition of the heading controller in (4.6). This is positive due to Assumption 4.1. As the yaw rate controller is UGES, the convergence time from $|\tilde{\chi}| = \frac{r_{fp}}{k_f}$ to $|\tilde{\chi}| < \epsilon$ is $\frac{2\ln\left(\frac{k_f \epsilon}{r_{fp}}\right)}{k_f}$. The constant 2 in this comes from that the vehicle has to turn from one turn to the other. Hence, the total time before reaching $|\tilde{\chi}| < \epsilon$ is t_ϵ from (7.36). Thus,the upper bound for the obstacle distance covered towards the USV is $u_{o,max} t_\epsilon$.

During the smoothing process of the reference filter of t_δ time, the USV travels towards the obstacle covered by an upper bound distance d_δ. Then, the USV will move towards the obstacle for during the whole turn of π rad. As the USV move closer, the relative velocity compensated extended vision cone edge $\chi_{dca}^{n(j)}$ will move away from the USV course χ^n, and a lower bound can be set for the turning rate by setting $\dot{\psi}_{bd}^n$. The worst case scenario is to turn completely around away from the obstacle. Then, Assumption 4.1 makes sure that the upper bound for the distance covered by the USV towards the obstacle during the turn is d_{turn} in (7.37).

Then, when the switching distance in (7.35) is satisfied, the distance between the USV and the obstacle will be lower bounded by d_{safe} when the USV has reached the edge $\chi_{dca}^{n(j)}$ within ϵ rad.

□

This proof shows that even with a maximum obstacle speed towards the USV

traveling at maximum speed, the obstacle distance is still lower bounded within the moment the USV reach the constant avoidance angle course $\chi_{dca}^{n(j)}$. Figure 7.1 visualizes the proof.

A situation which may lead the obstacle even closer to the barycenter is in the crossing stand-on scenario where the obstacle is not obeying COLREGs. Here, the barycenter is turning the fastest way out such that the constant 2 is removed from (7.36):

$$t_\epsilon = t_\delta + \frac{\pi}{r_{fp}} - \frac{1}{k_f} - \frac{\ln\left(\frac{k_f \epsilon}{r_{fp}}\right)}{k_f}, \epsilon \in \left(0, \psi_{fp}^n\right] \tag{7.39}$$

The rest of the proof follows the derived equations trivially with $d_{critical}$ instead of d_{ca} for entering collision avoidance mode.

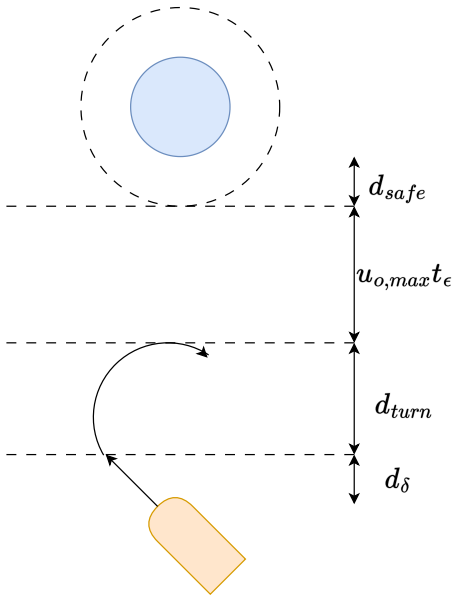

Figure 7.1: Lemma 7.4 illustration.

Now, the constant avoidance angle algorithm will be combined with a LOS guidance

law for one USV. Without loss of generality, the USV is assumed to follow a straight line along the x-axis. Thus, the guidance law is the following

$$\chi_{los}^{n} = \arctan\left(\frac{-y^{n}}{\Delta}\right) \tag{7.40}$$

where Δ is the lookahead distance term. This guidance law will be combined with Lemma 7.1-7.4 to guarantee collision avoidance under the mentioned assumptions in the thesis.

Theorem 1:

Let the constant avoidance angle safety margin angle be in the interval

$$\alpha_o \in \left[\arccos\left(\frac{R_o}{R_o + d_{safe}}\right) + \epsilon, \frac{\pi}{2}\right) \tag{7.41}$$

and let the switching distance satisfy (7.35) from Lemma 7.4. Moreover, the saturation level in the heading controller r_{fp} from (4.8) is set to satisfy (7.12) with (7.13). Let the lookahead distance for the LOS guidance law satisfy

$$\Delta > \frac{mu_d U_{b,sup}}{|Y_v| v_{sup} - mu_d r_{fp}} \tag{7.42}$$

The initial sway velocity is upper bounded by $|v(t_0)| < v_{sup}$. The USV modeled in (7.1) governed by the controllers in (4.1) and (4.6), controlled by the LOS guidance law (7.40) and the collision avoidance law (5.10) will then converge to a straight path along the x-axis until it encounters an obstacle modeled by (3.20). The USV will then safely prevent a collision with the obstacle and will converge to the path along the x-axis after passing the obstacle. For the whole encounter sequence, it is ensured that

$$d_{ob}(t) \geq d_{safe} > 0 \forall t \geq t_0 \tag{7.43}$$

Proof. The desired turning rate of the LOS guidance law is found by differentiating (7.40) with respect to time:

$$\dot{\chi}_{los}^{n} = -\frac{\Delta \dot{y}^{n}}{\Delta^2 + (y^{n})^2} \tag{7.44}$$

This is upper bounded by

$$|\dot{\chi}^n_{los}| \leq \frac{U_{b,sup}}{\Delta} \tag{7.45}$$

Inserting this into the heading controller (4.6) yields the maximum desired heading rate

$$|r_{los}| \leq \frac{U_{b,sup}}{\Delta} + r_{fp} \tag{7.46}$$

Applying (7.8) Lemma 7.2 for finding an upper bound on the desired yaw rate, the following minimum limit for the lookahead distance is obtained:

$$\Delta > \frac{mu_d U_{b,sup}}{|Y_v| v_{sup} - mu_d r_{fp}} \tag{7.47}$$

Setting Δ higher than this threshold with $|v(t_0)| < v_{sup}$ implies that $|v(t)| < v_{sup}$ until time t_2 when the USV enters collision avoidance mode. Lemma 7.3 is then used to get

$$|v(t)| v_{sup} \forall t \geq t_0 \tag{7.48}$$

The USV speed is then bounded by $U_b < U_{b,sup}$. At t_1, the conditions for entering collision avoidance mode are fulfilled. Lemma 7.4 ensures that there is a time $t_2 > t_1$ with $d_{0b}(t_2) \geq d_{safe}$ and $|\chi^n(t_2) - \chi^n_{dca}(t_2)| \leq \epsilon$. Since the reference model for the heading provides a smooth reference, the heading deviation has a locally exponentially stable equilibrium at $\tilde{\chi}^n = 0$ when using the heading controller (4.6). Thus, the following is ensured:

$$|\chi^n(t) - \chi^n_{dca}(t)| \leq \epsilon, \forall t \in [t_2, t_3] \tag{7.49}$$

t_3 is the time when the USV is exiting collision avoidance mode.

For relative velocity compensation, define a coordinate frame O with an origin moving with the obstacle velocity $\boldsymbol{\nu}_o$. The USV velocity is then within ϵ rad of $\boldsymbol{\nu}^{n(j)}_{\alpha_o}$ from (5.1). In this expression, $u_{\alpha_o} > 0$ by its definition, such that Lemma 7.1 ensures

the following:

$$d_{ob}(t) \geq d_{safe}, \forall t \in [t_2, t_3] \tag{7.50}$$

Hence, (7.43) is satisfied. Lemma 7.1 states that the USV is circling around the obstacle when the constant avoidance angle is followed. Therefore, there will be a time t_3 where the desired course reference χ^n_{los} is outside of the relative velocity compensated extended vision cone. Then, the USV exits collision avoidance mode and converges to the x-axis.

□

Chapter 8

Simulations

In this chapter, the performance of the constant avoidance angle algorithm integration into the null-space-based behavioral control scheme is demonstrated. The purpose is to validate the theoretical findings.

The first part shows the performance in the ideal case when the controller is implemented in the Python wrapped C++ simulator. Here, all the USV and obstacle states are available synchronously for every time step in the explicit Euler update scheme. This allows us to implement the control scheme centralized, also because the the actuator inputs can be set centralized. The heading, surge and yaw rate controllers from Chapter 4 are used, such that the whole control hierarchy is implemented. For this ideal case, only a scenario with a static obstacle is shown.

After the ideal case is presented, a thorough demonstration of the performance of the controller implemented in the high-fidelity Robot Operating System (ROS) simulator is given. ROS is a framework with tools for simulation, control and other functionality mainly for robotics applications. The ROS simulator already had autopilots for forward speed and heading. This made parts of the implementation simpler, as none of the controllers in Chapter 4 were needed. The two USVs ran as two separate nodes in ROS, since they were connected to the simulator via different IP addresses. The USVs shared state information between them via radio signals. Therefore, the

control scheme was distributed identically and independently on each USV. The radio communication had a greater delay than direct measurements from the ownship, such that the ownship state updates came more frequently than the state updates from the other USV. To make sure that both USVs shared information about the obstacles, the obstacle information was made on one of the USVs and transmitted to the other. Thus, one USV would always have a slight delay on the obstacle observations. Moreover, the simulator added noise on the USV states both in position and velocity. All this caused small disturbances on the controller, providing a more realistic behavior than in the ideal case. The control scheme was implemented identically and distributed over the two USVs, based on the assumption that each USV get approximately equal input from the measurements. The simulations were performed on static and dynamic obstacles. All the COLREGs scenarios are demonstrated for completeness.

The controllers were tuned almost equally for both simulators. Tuning parameters which were different will be stated in Section 8.1. For the waypoint path following, the USVs were instructed to drive from the initial barycenter position to $[x, y] = [1500, 1500]$ meters, i.e driving northeastwards. For the NSB scheme, the inter-vessel collision avoidance limit d_o in (6.13) was set to 20 meters with a penalty $\Lambda_o = 0.1$. The activation limit was never reached, and consequently this functionality was never activated. For the formation task, $\boldsymbol{\sigma}^p_{f,d} = [0, \pm 20]^T$, implying a constant cross-track distance of 20 meters from the USV to the barycenter. This implies 40 meters between the USVs in the cross-track direction. The weights in (6.18) were set to be $\boldsymbol{\Lambda}^p_f = [0.01, 0.1]^T$, leading to a greater effort into keeping the cross-track distance between the vessels to the desired value. For the path following, the constant in the lookahead equation (6.34) $\mu = 10000$ such that the lookahead distance was lower bounded by 100 meters. Recall from Section 3.2 that the curve fitting model was optimal around 10 knots, or 5.14 meters per second. Therefore, the desired path following speed was 5 meters per second. k_θ in the θ update law in (6.29) was 1. The inscribed circle radius R_c was set to 125 meters to accommodate for the maneuvering limitations in the mine sweep scenarios. The frequency of the parametrized circular path was set to $f_c = 0.01$. For the CAA algorithm, every obstacle radius was set to be 5 meters. The safety angle α_o introduced in Section 5.1 was set to $\frac{\pi}{8}$, and for the critical mode it was

set to $\frac{7\pi}{24}$, i.e. a $\frac{\pi}{6}$ addition. The distances d_{ca} from (5.12) and $d_{critical}$ from(5.26) were 300 and 150 meters, respectively, in addition to the desired distance between the USVs of 40 meters plus their respective radii of 5 meters.

8.1 Ideal case

In the ideal case, the inscribed circle radius was set to 150 meters with a frequency of 0.005. $d_ca = 250$ meters, such that the collision avoidance mode was entered later than for the ROS simulator.

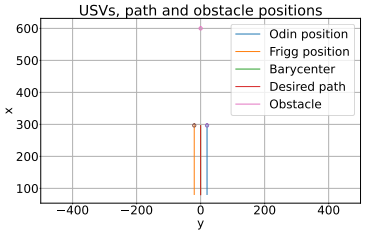

(a) Before collision avoidance mode.

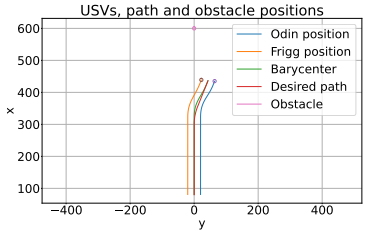

(b) After entering collision avoidance mode.

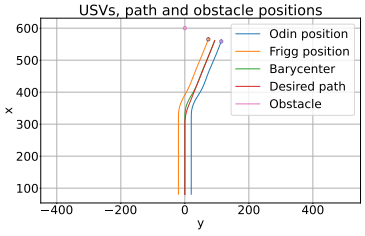

(c) Closest to the barycenter.

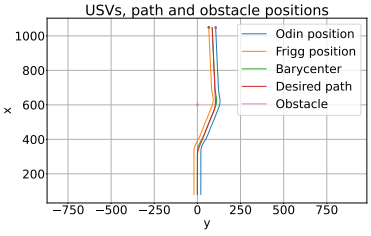

(d) After the encounter.

Figure 8.1: Time series of the static obstacle encounter in the ideal case.

The obstacle was located 600 meters straight ahead of the barycenter. Figure 8.1 shows the time series of the encounter. Figure 8.1a shows how the USVs follow the path perfectly without any perturbations, as the formation and path following errors are precisely zero in the initial conditions. Figure 8.1b shows how the USVs manage to perform a turn away from collision with the obstacle. The collision avoidance mode is

entered and the path is updated accordingly. Here, the way out of the collision cone is identical for port and starboard turns, and the control scheme chooses a starboard turn. Figure 8.1c shows the moment when the USVs are closest to the obstacle. Figure 8.1d shows the end of the encounter, where the USVs return to waypoint path following after passing the obstacle.

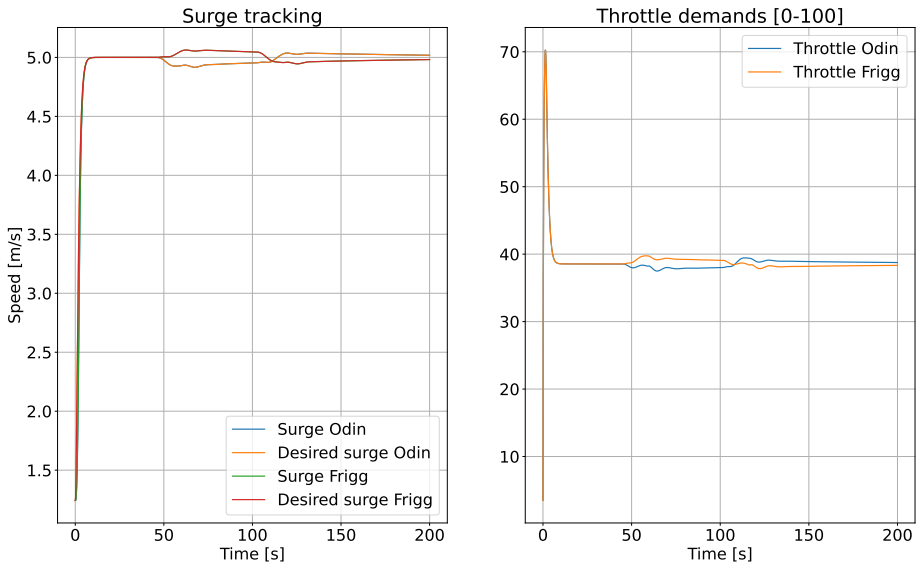

Figure 8.2: Surge and throttle demands in the ideal case.

Figure 8.2 shows the performance of the surge controller in (4.1). Here, the surge velocity reference was passed through the reference model in Section 4.3, such that a step from 0 to 5 meters per second was replaced with a smooth curve. Note that the USVs were not set to keep this speed individually, but rather corporate such that the barycenter speed was constant at 5 meters per second. This explains why the outer USV in a turn maintained a higher speed for these periods. The controller was tuned such that the USVs kept some margin to the actuator constraints. For the throttle

demand, this was from 0 to 100. The plots of the throttle demands shows that the demands were lower than 75.

Figure 8.3 shows the corresponding behavior for the yaw rate. Here, the references were more dynamic, as these are given from the heading controller. The actuator constraints of a steering angle interval from −27 to 27 degrees were respected as the steering angle never reached 5 degrees.

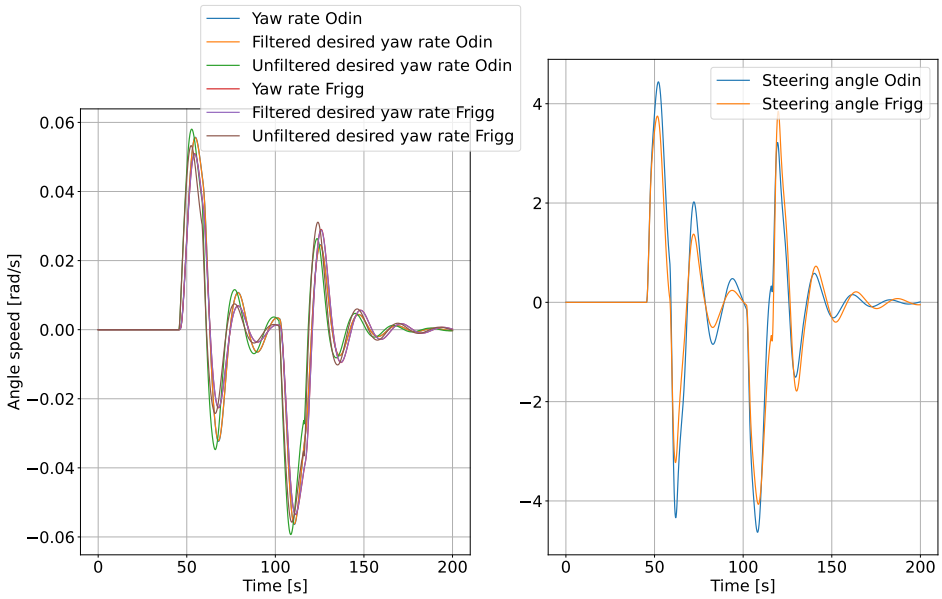

Figure 8.3: Yaw rate and steering demands in the ideal case.

Figure 8.4 shows the performance of the heading controller. The filtered signals kept a smaller magnitude and a delay in the signals. Note that the real headings had a larger magnitude than even the unfiltered references in the turns, which could have been prevented with smaller proportional gains on the controller at the cost of a slower tracking.

In Figure 8.5, the path following errors and formation distances are shown. The

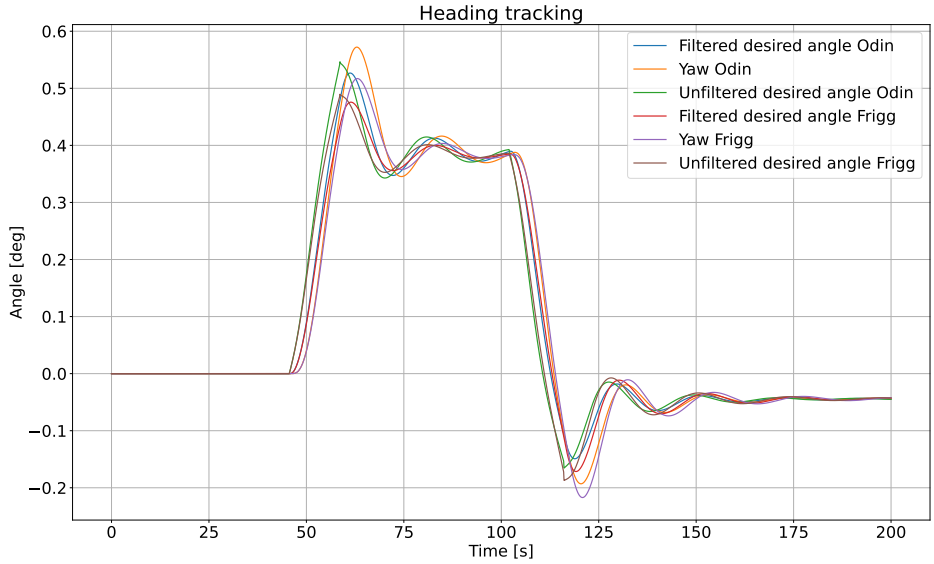

Figure 8.4: Heading tracking in the ideal case.

path following errors increases during the turns, despite the continuous heading reference in the inscribed circles approach. After the turns, the errors converge back to zero. The along-track errors quickly goes back to zero in the straight line following segments, as the update law of the path parameter θ in (6.29) increases less when the course angles perturb from their references. The cross-track error oscillates on the way back to zero. This effect could be alleviated by increasing the constant term in the lookahead distance in (6.34) at the cost of a slower convergence. The formation errors experience a less than linear growth in the turning. The reason why the growth is less than linear is because of the damping from the formation task, as it strives to counteract the perturbations from the desired formation values. In the straight line segments, the deviations converge to zero, yet at a slower rate than the period if simulation.

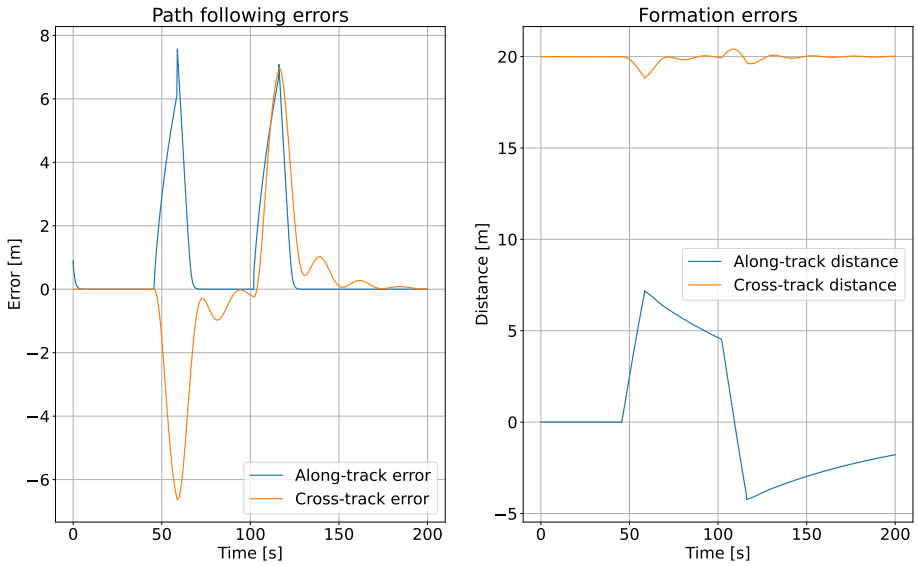

Figure 8.5: NSB performance in the ideal case.

8.2 ROS simulations

From now on, a presentation of the controller will be given in the ROS simulator. First, the static obstacle scenario will be shown, before the performance in all our selected COLREGs scenarios will be presented.

8.2.1 Static obstacles

The first and simplest scenario shows an encounter with a static obstacle. The obstacle was located at $[x, y] = [300, 300]$ such that the barycenter would drive straight through it without collision avoidance enabled. Figure 8.6 shows the time series. In Figure 8.6a, the barycenter is following a straight line towards the next waypoint. Then in Figure 8.6b, the obstacle is detected to be within the distance of collision avoidance

activation. Also, the barycenter is on collision course with the obstacle. The obstacle is static, and therefore the turning direction is chosen freely. The required turning angle out of the collision cone is equal for port and starboard turns, since the obstacle is on the middle of the path. When this turning difference out of the collision cone is small, the USVs always choose the starboard turn. This is because the algorithm is distributed, and small deviations in measurements could make the USVs choose a different turning direction, which is not desirable. The turning maneuver is ensured to be continuous because of the inscribed circle path following in the transition. However, note that some small deviations in the path following are still observed due to steps in the path curvature. The curvature steps could have been smoothed with a more complex model in the turning transitions than the inscribed circles, at the cost of a more complex solution for trajectory generation without only straight line and circular segments. Moreover, the path following task could be improved by increasing the inscribed circle radius and adjusting the frequency of the parameterized path accordingly. However, this would lead the barycenter closer to the obstacle during the turn. Therefore, if one would increase the inscribed circle radius and still maintain the minimum obstacle distance, one could increase the collision avoidance activation distance d_{ca}. Figure 8.6c shows the moment when the barycenter is closest to the obstacle. Note that this moment is at the end of the turning maneuver, just when the constant avoidance angle is reached and the barycenter can follow a straight line. Consequently, increasing the inscribed circle radius would make this point closer to the obstacle. Figure 8.6d shows the whole encounter. When the CPA dependent hysteresis time has passed, the USVs turn back to steering towards the next waypoint.

Figure 8.7 shows the desired path angle and the actual heading of the barycenter. The approach with inscribed circles for the curved path following ensures that no steps in the heading occur. However, the heading is not continuous in its derivative. This could be obtained by e.g. second order reference model at the cost of an increased complexity and no circular path following. Therefore, in order to keep the analysis intuitive, this approach was chosen. Some oscillations around the reference angle are present. These could get smaller amplitudes by increasing μ in the lookahead expression (6.34) at the cost of slower converge of the path following errors. When the

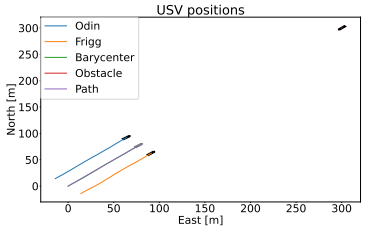

(a) Before collision avoidance mode.

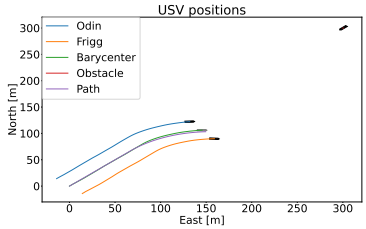

(b) After entering collision avoidance mode.

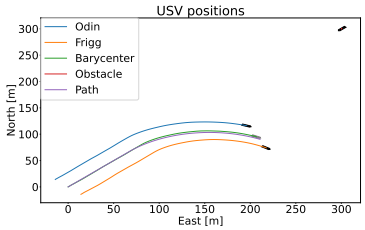

(c) Closest to the barycenter.

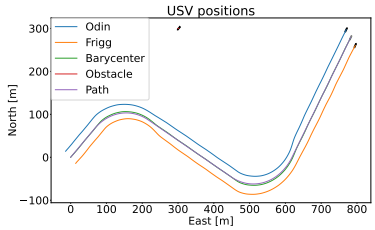

(d) After the encounter.

Figure 8.6: Time series of the static obstacle encounter.

USVs exited the collision avoidance mode to continue the waypoint path following, the desired path angle was necessarily smaller than the first 45 degree heading since the waypoint was not longer located precisely northeastwards anymore. The potential issue of not returning to the original path was addressed and discussed in Section 6.3.2.

Figure 8.8 shows the heading tracking for Odin and Frigg individually. Note that these deviate during the turning. During the first turn to reach the constant avoidance angle in collision avoidance mode, Frigg performs a sharper turn than Odin. This is because Frigg is closest to the inscribed circle center. Thus, the required turning rate is greater since the turning radius is smaller. When turning back to the waypoint path following, Odin has the highest turning rate for the same reason. Note that the headings approach each other during the straight line path following segments, such that they eventually align around the barycenter.

Figure 8.9 shows the speed tracking for Odin and Frigg. The desired speed quickly approaches a value around 5 meters per second. During the first turn, Odin maintaints

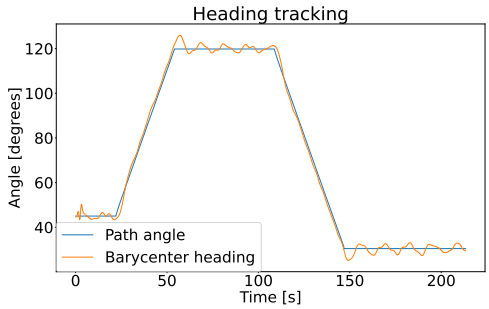

Figure 8.7: Barycenter tracking of the desired path angle.

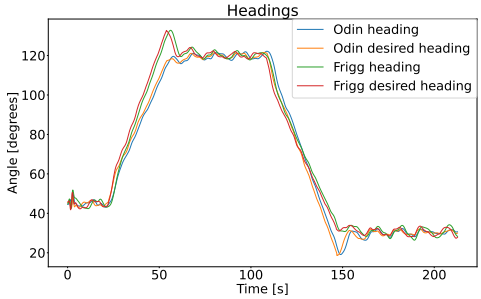

Figure 8.8: Real and desired headings for Frigg and Odin.

a higher speed than Frigg since it is farthest away from the inscribed circles center. For the second turn, the behavior is opposite. In the straight line following segments, the speeds are approaching each other, yet at a slow pace.

The maintained speed and heading differences after the turns are performed can also be interpreted in the context of the task accomplishment in NSB. Consider Figure 8.10, which consists of the path following errors and the formation distances. The path following errors in Figure 8.10a increases during the turns. The along-track error decreases quickly after the turn, as the path parameter θ is dependent of speed and course errors, such that it will grow at a slower rate when the barycenter is behind. The cross-track error is approaching zero at a slower rate, caused by the lookahead

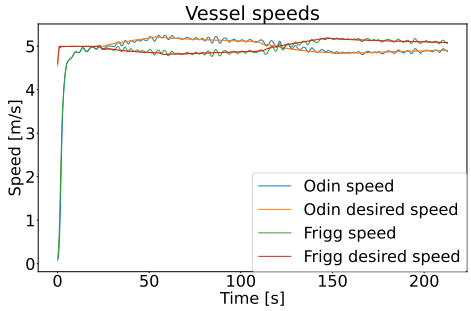

Figure 8.9: Real and desired speeds for Frigg and Odin.

distance defined dependent of a constant term as well as the path following errors. The formation errors in Figure 8.10b shows an increasing deviation during the turns. The rate of change is less than linear since the USVs strive to maintain their desired formation, and hence they contribute with a velocity reference working against the perturbations away from their equilibrium. During the straight line segments, they approach their desired values. The USVs did not reach their desired values precisely before the simulation ended, but the convergence rate could be increased by increasing the penalties in Λ_f^p. The plot shows that the along-track error has the slowest convergence. However, increasing these penalties too much could cause the task errors to be underdamped, leading to oscillations around the correct formation values. The chosen tuning was found to be satisfactory after experimentation with these effects. As the formation and path following errors are decreasing in the straight path following segments, the vessel speeds and headings for Frigg and Odin are approaching each other since they are approaching the equilibrium for all the task variables.

Lastly, Figure 8.11 shows the distance from the obstacle center to the barycenter. It is always above 200 meters, and obtains its lowest value when the constant avoidance angle is reached. After the obstacle is passed, the time since entering collision avoidance mode has exceeded the hysteresis time, such that the USVs can head towards the next waypoint. Consequently, the distance decreases yet again, but it does not go lower than 400 meters. The obstacle is always on a safe distance from the USVs.

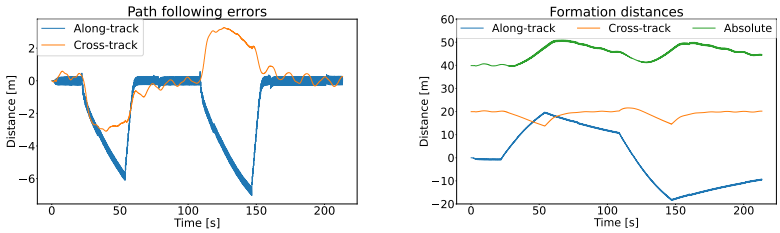

(a) Path following errors.

(b) Formation distances.

Figure 8.10: NSB performance for a static obstacle.

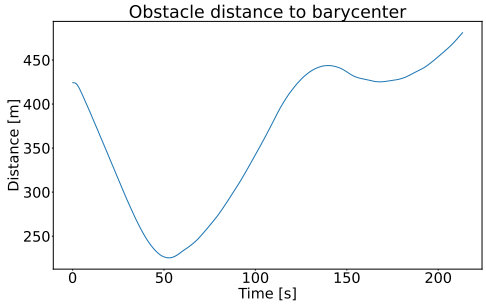

Figure 8.11: Distance from obstacle to barycenter.

8.2.2 Dynamic obstacles: COLREGs scenarios

This section demonstrates the performance of the control scheme in the following COLREGs scenarios: Crossing: Give-way, Crossing: Stand-on, Head-on and Overtaking. The dynamic obstacle always kept a constant forward velocity $u_o = 3$ meters per second and was positioned to be on collision course with the USVs.

8.2.2.1 Crossing: Give-way

Figure 8.12 is the time series of the crossing scenario where the obstacle is coming from the starboard side of the vehicles. Consequently, the USVs are in a crossing situation where they are obliged to give way to the obstacle and cross behind it. Figure 8.12a is

captured the moment before entering the collision avoidance mode, and Figure 8.12b is some time after action is taken to prevent a collision with the obstacle. The USVs correctly classify the give-way scenario and perform a starboard turn accordingly. Figure 8.12c is captured the moment where the barycenter is closest to the obstacle, and Figure 8.12d is after the collision avoidance mode is exited such that the USVs return to waypoint path following.

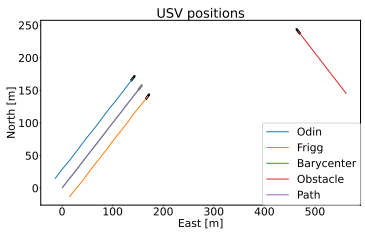

(a) Before collision avoidance mode.

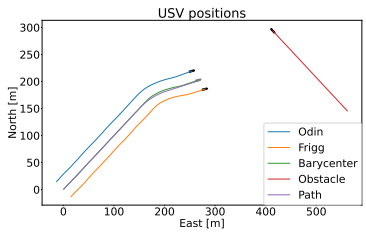

(b) After entering collision avoidance mode.

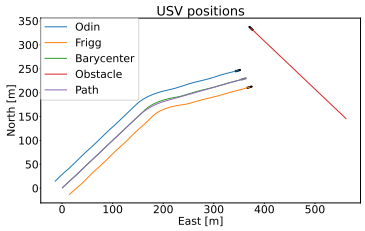

(c) Closest to the barycenter.

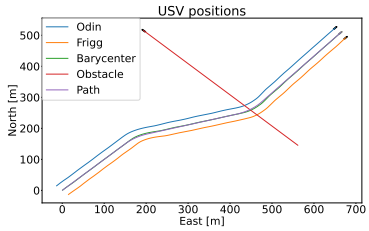

(d) After the encounter.

Figure 8.12: Time series of the crossing give way scenario.

Figure 8.13 shows the NSB task performance during the encounter. On the left, Figure 8.13a shows the path following errors. Two spikes are observed at two occasions; when entering and exiting collision avoidance mode. These are the points were the heading reference goes from being stationary to linear growth, such that a heading reference discontinuity occurs. The spike magnitudes could be decreased by increasing the inscribed circle radius such that the proportionality constant for the linear growth of the heading reference would be smaller. The formation distances in Figure 8.13b shows that the along-track formation distance deviates linearly from zero during the

turning maneuvers, but goes back toward zero in the periods where the USVs follow a straight line. The cross-track distance deviates less from its desired value of 25 meters due to the higher penalty on the cross-track distance in Λ_f^p. The absolute distance between the vessels remains between 40 and 50 meters, such that the inter-vessel collision avoidance task is never active. Some small oscillations are observed because the formation task has no damping terms. Consequently, the formation distances can be interpreted as being controlled by a pure proportional controller. The oscillations can be damped by putting less weight on the Λ_f^p diagonal at the cost of a slower formation task accomplishment.

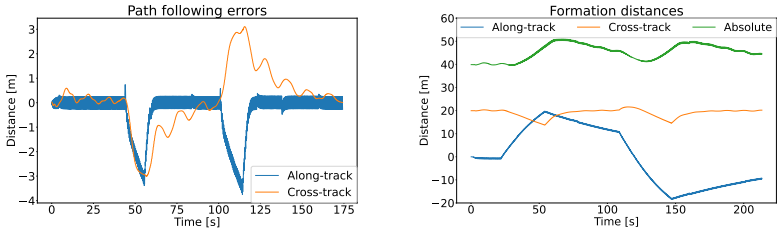

(a) Path following errors.

(b) Formation distances.

Figure 8.13: NSB task parameters for the crossing give way scenario.

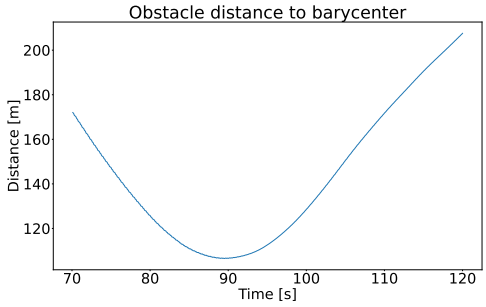

Figure 8.14: Distance from obstacle to barycenter for the crossing give way scenario.

The obstacle distance to the barycenter for the time when it is the closest is shown

in Figure 8.14. The obstacle is always on a greater distance than 70 meters. After the barycenter has passed the obstacle, the distance increases. Note that the growth is slightly slowed down at around 120 seconds when the barycenter exits collision avoidance mode.

8.2.2.2 Overtake

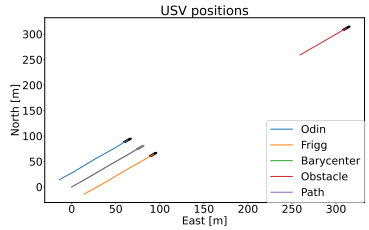

(a) Before collision avoidance mode.

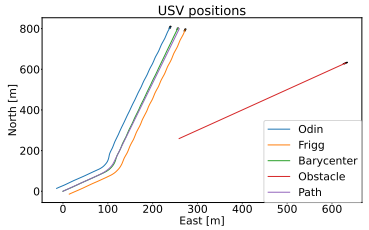

(b) After entering collision avoidance mode.

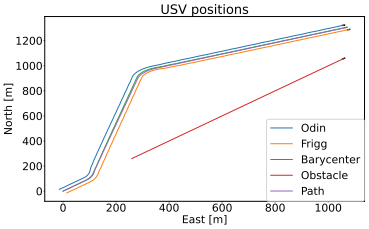

(c) Closest to the barycenter.

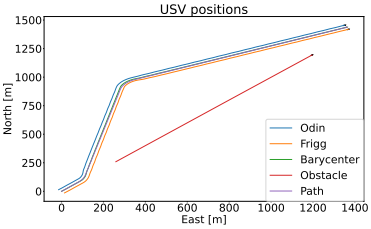

(d) After the encounter.

Figure 8.15: Time series of the overtake scenario.

Figure 8.15 shows the time series of the overtake scenario. In Figure 8.15a, the USVs are about to start maneuvering away from the obstacle as they have almost entered collision avoidance mode. Figure 8.15b shows some time after steering away from the obstacle, and Figure 8.15c shows the closest point of approach. Note that this point is after the USVs have left the collision avoidance mode. This is due to the small speed difference between the barycenter and the obstacle, which leads to a long estimated time to the closest point of approach, and consequently a long time

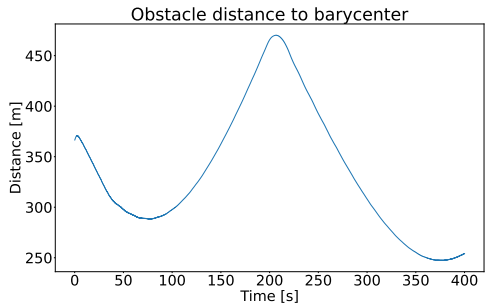

Figure 8.16: Distance from obstacle to barycenter for the overtaking scenario.

discrepancy between the estimated and real time to the CPA. Figure 8.15d shows the end of the time series when the barycenter has passed the obstacle and started to approach the next waypoint.

Figure 8.16 shows the distance between the obstacle and the USVs. The distance is above 250 meters at all times, and the closest point is right before the end of the simulation. The distance continues to increase after the closest point is reached, which is also at the point where the USVs have passed the obstacle.

The safety margin angle α_o was equal for all simulations. For the overtaking scenario, this resulted in a large turn. Despite that this large turn ensured a safe minimum distance, it may be seen as unnecessary to drive this far around. Possible solutions to this issue would be to e.g. have a COLREGs situation dependent α_o, or making α_o minimum obstacle distance dependent, which we will see in Section 8.2.3. Furthermore, the hysteresis time would in the optimal case be over in the moment of passing the obstacle. An alternative approach to making the hysteresis CPA dependent could be let it be dependent on the along-track distance to the obstacle course for the overtaking scenario.

8.2.2.3 Head-on

The head-on scenario is plotted in Figure 8.17. Figure 8.17a shows the moment before entering collision avoidance mode, and Figure 8.17b shows the beginning of the turning

maneuver. The USVs perform a starboard turn in accordance with the COLREGs after correctly classifying the head-on situation. Figure 8.17c shows the closest point of approach, and Figure 8.17d shows the whole series after the USVs have returned to waypoint path following.

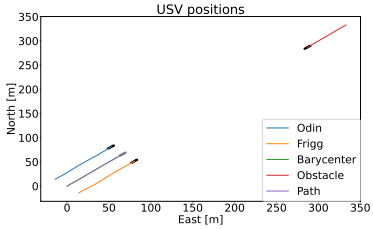

(a) Before collision avoidance mode.

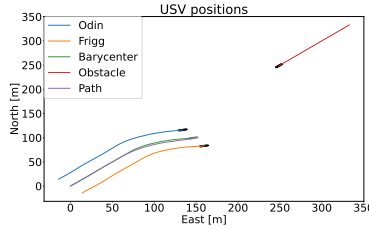

(b) After entering collision avoidance mode.

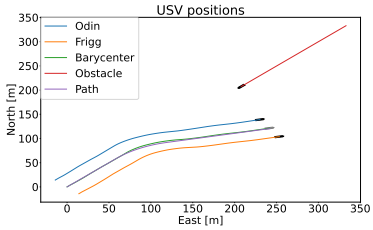

(c) Closest to the barycenter.

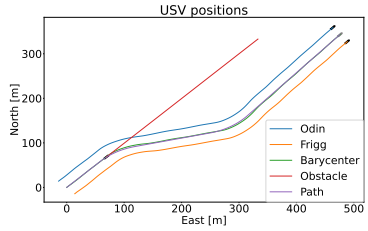

(d) After the encounter.

Figure 8.17: Time series of the head-on scenario.

Figure 8.18 shows the development of the obstacle distance to the barycenter, which is above 90 meters. Note that this is the minimum distance of all the COLREGs scenarios so far, as the USVs were driving on reciprocal courses with the obstacle. Since the safety margins are defined in the angle space, the distance in meters will be the smallest in this scenario because the USVs and the obstacle are passing each other on almost reciprocal courses. Moreover, the hysteresis time is over after the USVs have passed the obstacle and they are driving on almost reciprocal courses away from each other. Therefore, the negative contribution to the obstacle distance after the hysteresis time is less distinct compared to the previous examples.

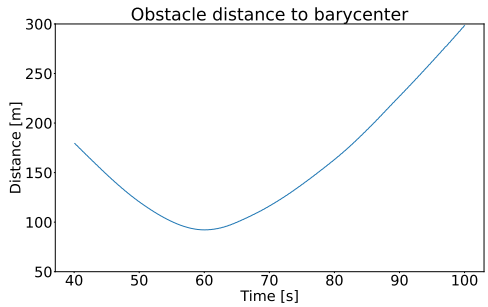

Figure 8.18: Distance from obstacle to barycenter for the head-on scenario.

8.2.2.4 Crossing: Stand-on

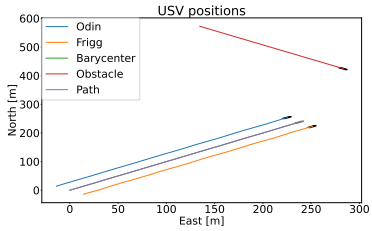

(a) Before collision avoidance mode.

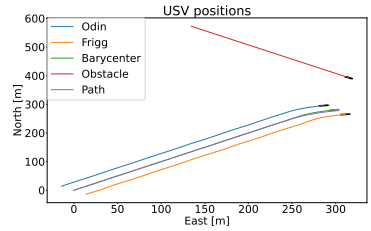

(b) After entering collision avoidance mode.

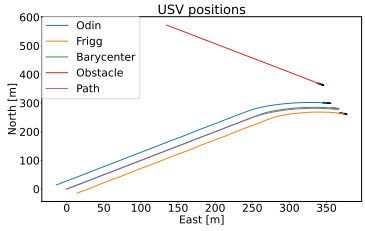

(c) Closest to the barycenter.

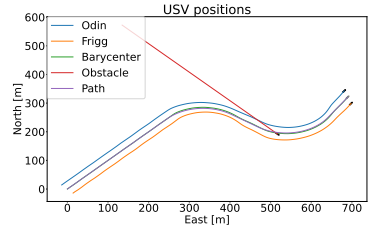

(d) After the encounter.

Figure 8.19: Time series of the crossing stand-on scenario.

The last COLREGs scenario considered is the crossing from port scenario. Here, the

convention is to maintain the course and speed for the other boat to cross behind safely. This behavior is not of particular interest as it implies that no action is taken. Therefore, the obstacle is set to follow a constant velocity throughout the simulation, which implies not following COLREGs. This will trigger the critical mode in the collision avoidance algorithm when the obstacles and the USVs still are on collision course at a sufficiently small distance. Figure 8.19 shows the whole time series. Figure 8.19a shows that the USVs have followed expected behavior, which is to keep the same velocity. However, since the obstacle has not taken action to avoid the USVs, they enter the critical mode in Figure 8.19b. Here, an extra safety angle is added to ensure that the USVs perform a large enough turn when they are this close to the obstacle. The shortest way out is found to be a starboard turn in this example, which is seen in Figure 8.19c and Figure 8.19d, when they are the closest to the obstacle and when they return to waypoint path following. Crossing in front of the obstacle may not seem to be the safest option. An alternative approach could be to perform a port turn in this scenario. However, this could cause an unnecessary large turn towards the obstacle if the course difference between the barycenter and the obstacle would have been smaller (i.e. closer to the edge of being classified as an overtaking scenario). Hence, the minimum distance would have been smaller. And since the critical mode is activated, we chose to maximize the minimum distance to the obstacle and therefore turn the shortest way out of the collision cone. An extra constant is added to the CPA estimation of the hysteresis due to the larger turns and closer obstacle distances. The USVs end up driving ahead of the obstacle for some time before getting out off its way and prevent the collision successfully.

Figure 8.20 shows the obstacle distance to the barycenter, which is above 80 meters. The extra hysteresis time makes sure that negative contribution to the distance from returning to waypoint path following comes with some time margin after the real CPA, which is visible in the plot.

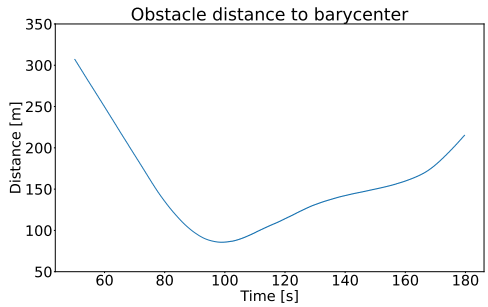

Figure 8.20: Distance from obstacle to barycenter for the crossing stand-on scenario.

8.2.3 Tuning of minimum distance: Dynamic obstacle

A last simulation is presented to validate the minimum distance tuning of the safety angle α_o in Section 5.5. The give-way crossing scenario was repeated where the tuning was set to be identical, with the exception that the minimum obstacle distance was defined explicitly instead of defining α_o in the heading space. The angle is instead found from (5.31), with d_{CPA} calculated and updated throughout the turning maneuver and the minimum distance between the obstacle and the barycenter $\delta = 150$. A demonstration of the behavior of the USVs is omitted in this part, as it was similar to the previous give-way scenario but with a different turning angle.

Figure 8.21 shows the distance between the obstacle and the barycenter around the closest point of approach. The minimum distance was 150.27 meters, which is 4.73 meters less than the expected 155 meters after adding the obstacle radius 5.

To explain the discrepancy from the expected minimum distance, consider the path following error development in Figure 8.22. In the moment of the minimum distance at 81.5 seconds through the simulation, the cross-track path following error was found to be -1.36 meter. As the error in this direction is perpendicular to the path and straight towards the obstacle, the path following error contributes to explain the discrepancy. Furthermore, the controller in the simulations was set to start straight line following of the constant avoidance angle as long as the deviation was less than 0.5 degrees ($\frac{\pi}{360}$), which could cause the USVs to come closer to the obstacle.

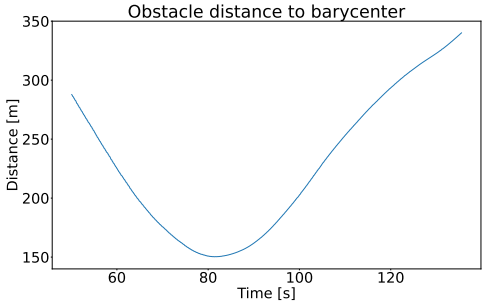

Figure 8.21: Distance from obstacle to barycenter for the give-way scenario with minimum distance tuned α_o.

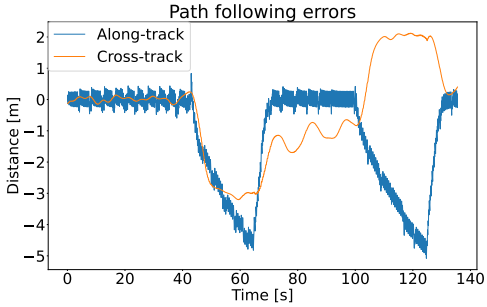

Figure 8.22: Path following errors for the give-way scenario with minimum distance tuned α_o.

Chapter 9

Experiments

This chapter presents the results from testing the control scheme from Chapter 5 and Chapter 6. The experiments were performed on the testing site of FFI in Horten with the vessels Frigg and Odin. The control scheme implementation was almost identical to the one in the ROS simulator. Differences between the simulations and the experiments will be stated when they are relevant.

The experiments were limited to straight line following with collision avoidance with one obstacle only. Inscribed circles were added after the experiments, such that the first path update suggestion during collision avoidance mode transition was used (see the left of Figure 6.2). The desired path following speed was $5m/s$. Three COLREGs scenarios were tested: Crossing give-way, head-on and overtake. Crossing stand-on was not included as the COLREGs convention is to perform no maneuvers at all. Triggering the critical mode was not done since it would lead to critically small distances between the vessels. Therefore, this scenario was shown in the simulations instead. The next sections show the performance of the control scheme with a real vessel named Nøkken, with a radius smaller than 5 meters.

A complete map with an overview of the environment was provided by FFI. Radar and lidar are used for detection of other surface vehicles as well as IMU and GPS for determining the USV's position, speed and heading. Position and speed of obstacles are

provided in real time. In this project, we assume we can trust the provided information about the vehicle and its surroundings.

The NSB scheme used the following tuning parameters: d_o in (6.13) was set to be 20 meters, such that the task only would be active when the absolute distance between Frigg and Odin was less than 20 meters. In the subsequent chapters one can observe that the distance was always above this limit, and therefore the system did not leverage this functionality. The desired cross-track distance from the vessels to the barycenter d_f in (6.17a) was set to 20 meters, such that the task would strive to maintain a 40 meters cross-track distance between the vessels. $\Lambda_f^p = \text{diag}(0.01, 0.1)$ from (6.18), implying a greater penalty for cross-track deviations in the formation driving. μ from (6.34) was set to 10000. Finally, $k_\theta = 1$ from the theta update law in (6.29).

The CAA algorithm used the following parameters: The obstacle radius R_o was set to 5. The collision avoidance mode activation distance $d_{ca} = 240$ meters from (5.12), and the safety angle α_o presented in Section 5.1 was set to $\frac{\pi}{8}$. Furthermore, $\epsilon_{overtake}$ from (5.25) was set to zero to avoid disagreements about the turning direction for Odin and Frigg caused by delays or noisy measurements.

For all plots in the waterplane, the vessels are scaled equally to Odin and Frigg with their respective headings in the capture moment. The obstacle boat is scaled equally

9.1 Crossing: Give-way

In the crossing scenario, the obstacle vessel started approximately 500 meters north and 300 meters east relative to the barycenter start position. It drove with a speed of approximately 3 meters per second in the westward direction. Figure 9.1 shows a time series of the encounter. Figure 9.1a shows the vessels in path following mode before triggering the collision avoidance mode conditions. The desired path starts near the barycenter, and the barycenter converges steadily towards it. In Figure 9.1b, the USVs have detected the obstacle, and find the constant avoidance angle. The encounter is correctly classified as a crossing give-way situation, such that the turning

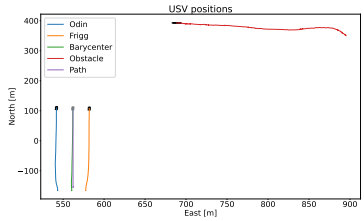

(a) Before entering collision avoidance mode.

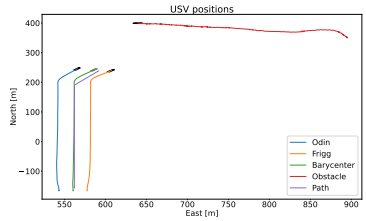

(b) After entering collision avoidance mode.

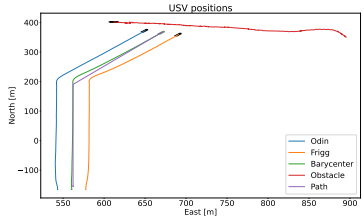

(c) Closest to the barycenter.

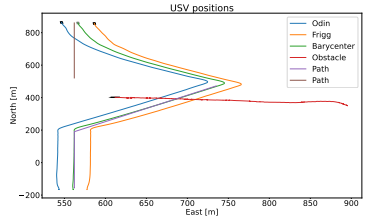

(d) After the encounter.

Figure 9.1: Time series of the crossing give-way scenario.

direcetion will be starboard. The updated path starts in the barycenter. The step change in heading reference causes the barycenter to diverge slightly from the path, as the barycenter was originally following the path straight north. After some time, the barycenter manages to converge to the constant avoidance angle path in Figure 9.1c, which is also the point where the barycenter is closest to the obstacle. Figure 9.1d shows the whole encounter. Notice that the USVs track the original path when the hysteresis time is over with some margin after the along-track component of the USVs have passed the obstacle. From here, the USVs slowly converge to the path again.

Figure 9.2a shows the path following errors. The error starts as non-zero due to the discrepancy between the path and the barycenter to begin with. However, both the errors converge to zero. Around time 85 seconds, when the USVs first enter collision avoidance mode, a small negative bump in the cross-track error is observed. Notice that the bump increases gradually from zero because the new constant avoidance

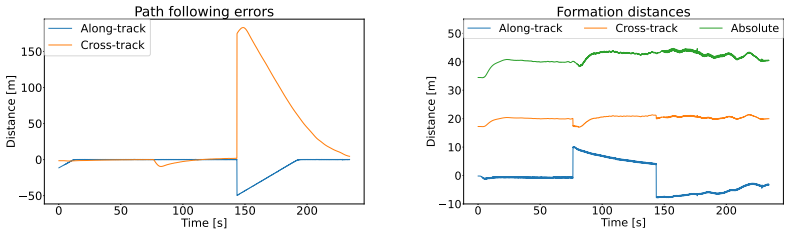

(a) Path following errors.

(b) Formation distances.

Figure 9.2: NSB performance for the crossing give-way scenario.

angle path starts in the barycenter. The bump occurs due to the deviation between the constant avoidance angle and the barycenter course from following the original path. The cross-track error converges steadily back to zero after adjusting the course. The along-track error remains low. This is because of the path parameter θ update law in (6.29): The update is dependent on the course discrepancy between the path and the barycenter course, such that only contribution from the USV speed is the component in the positive along-track direction. Consequently, the path parameter "waits" for the USV courses to adjust. When the collision avoidance mode is exited around time 145 seconds, large amplitude changes are visible for both along-track and cross-track errors. This is caused by the discontinuity of the path, which was also the motivation behind the second path update suggestion in Section 6.3.2.2 with the inscribed circles in 6.3.3. The cross-track error first increases after the step since the barycenter is driving away from the path before adjusting the course. The along-track error decreases linearly due to the mentioned path parameter update law. At the end of the experiment, the along-track error has converged, whereas the cross-track error has almost converged. The convergence speed could be increased by decreasing μ from (6.34), at the cost of more oscillations around the path.

Figure 9.2b shows different interpretations of the distances between the USVs. The absolute distance between the USVs is shown to be around 40 meters, and never below 30. Hence, the USVs are always on a safe distance, and no inter-vessel collision avoidance maneuvers are needed. The along-track and cross-track distances from the

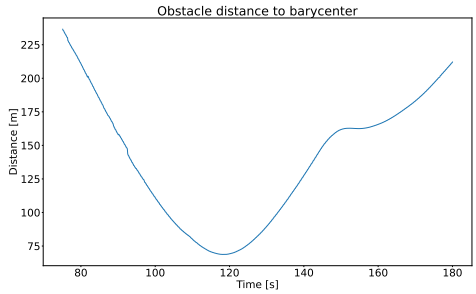

Figure 9.3: Distance from obstacle to barycenter for the crossing give-way scenario.

USVs to the barycenter changes when the USVs enter and exit collision avoidance mode. Notice that the cross-track distance adjusts faster than the along-track distance due to the increased penalty on the cross-track distance. The cross-track distance converges to the desired value fast, whereas the along-track distance does not manage to converge before exiting collision avoidance mode and before the experiment ended. However, one can notice that it slowly adjusts towards the desired value.

Finally, consider Figure 9.3. This illustrates the distance from the obstacle to the barycenter in the time frame where they are the closest. The closest point of approach is above 70 meters, which implies that it is above 50 meters from the closest USV. From this point, the distance increases until the hysteresis time is over. Then, a slight decrease is observed before increasing again, caused by the USVs returning to follow the original path and therefore moving closer to the obstacle again. The plot shows that the hysteresis is set long enough for the USVs not to approach the obstacle again at the closest point, such that it always is on a safe distance.

9.2 Head-on

For the head-on scenario, the obstacle boat was instructed to start approximately 500 meters north of the barycenter and drive with a speed of approximately 3 meters per second southwards. Figure 9.4 shows the whole sequence: Path following before

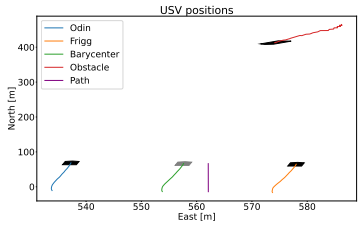

(a) Before entering collision avoidance mode.

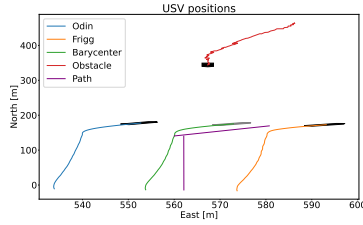

(b) After entering collision avoidance mode.

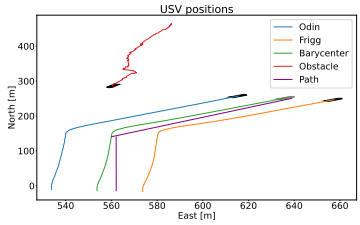

(c) Closest to the barycenter.

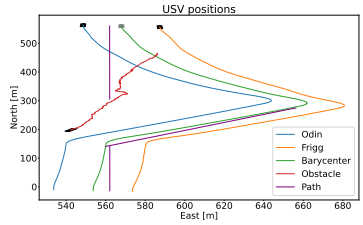

(d) After the encounter.

Figure 9.4: Time series of the head-on scenario.

entering collision avoidance mode, turning in collision avoidance mode, closest point of approach and going back to path following mode. Note that in the very beginning in Figure 9.4a, the USVs drive some meters in the wrong direction, caused by the fact that they started in with a small heading discrepancy. The barycenter approaches the path before getting the constant avoidance angle path update shown in Figure 9.4a, where it approaches the updated path. The COLREGs situation is correctly classified to be a head-on situation, leading to a starboard maneuver. The closest point of approach shown in Figure 9.4c validates that both USVs manage to pass the obstacle at a safe distance. The hysteresis proves to be sufficiently large, as the USVs go back to the original path following after passing the obstacle in Figure 9.4d.

Note that the obstacle is not driving straight south because the driver adapted the course in the beginning such that it could face the USVs as straight as possible. Furtermore, some chattering behavior was noticed in the obstacle position during

the turning maneuver of the USVs. This is because of a bug in the processing of the measurements, where the relative position between the obstacle and the USV was calculated before updating the heading of the boats. This did not affect the behavior of the USVs during the experiments.

The NSB task errors are shown in Figure 9.5. The path following errors in Figure 9.5a shows that the barycenter goes towards the path at first. When collision avoidance mode is entered, both errors jump to zero since the new path starts at the barycenter position. Then, the cross-track error increases as the barycenter course is different to the updated path angle. After some time, it converges back to zero, before a massive increase when the USVs exit collision avoidance mode. Note that the magnitude is lower than in the crossing scenario, as the constant avoidance angle is smaller since the USVs now do not need to compensate for westwards movement. Also, the hysteresis time was shorter when the obstacle moved towards the USVs. The absolute distance in Figure 9.5b is again above 30 meters, and the cross-track and along-track formation distances from one USV to the barycenter are converging towards their desired values, where the cross-track distance is faster because of the higher penalty.

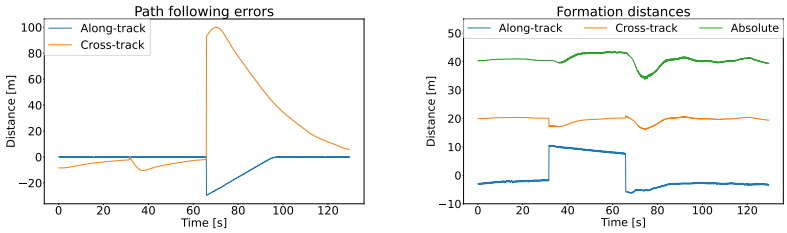

(a) Path following errors.

(b) Formation distances.

Figure 9.5: NSB performance for the head-on scenario.

Finally, the distance from the obstacle to the barycenter is shown in Figure 9.6. The distance is always above 80 meters, meaning that the distance to the closest USV from the obstacle is lower bounded by 60 meters. The collision avoidance mode exit after around 75 seconds is visible by the lower rate of increase of the distance. Again, the hysteresis ended after the closest point of approach, such that the obstacle always

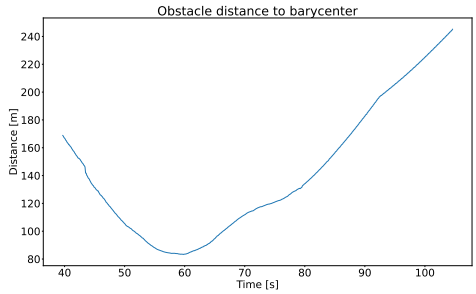

Figure 9.6: Distance from obstacle to barycenter for the head-on scenario.

is at a safe distance from the USVs.

9.3 Overtaking

For the last test scenario, the obstacle boat started approximately 300 meters north of the barycenter and was instructed to drive 3 meters per second northwards. Consider the time series in Figure 9.7. The original path following is shown in Figure 9.7a, before activating collision avoidance mode and turning accordingly in Figure 9.7b. The small relative velocity between the barycenter and the obstacle results in a new heading reference. Hence, a small turn is required given the CAA tuning variables. This issue could be circumvented by increasing the safety angle α_o. However, the turning angle was smaller than $\frac{\pi}{8}$, caused by not adding the sign logic to the (5.7), such that (5.4) was used. This error was found after the experiments and led to a too small path angle. Among the three scenarios, this was the only one that triggered the condition causing the two equations to be different. Consequently, the relative velocity compensation was added with the wrong sign. This was fixed before the simulations, but not for the experiments. Except this too small turn, the algorithm was working as expected throughout the time series. But since the distance from the obstacle to the closest USV was considered to be too close in Figure 9.7c, the drivers took control over the vessels shown in Figure 9.7d. The collision avoidance mode was still active in this scenario,

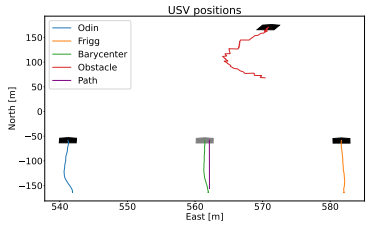

(a) Before entering collision avoidance mode.

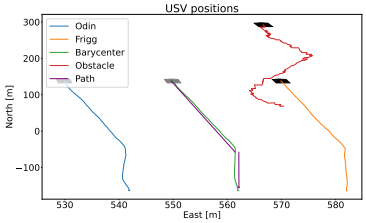

(b) After entering collision avoidance mode.

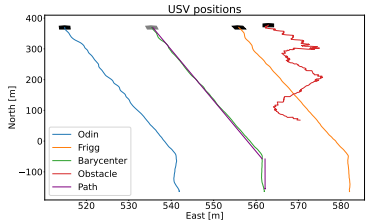

(c) Closest to the barycenter.

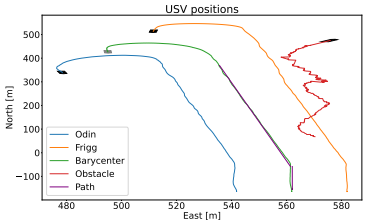

(d) After the encounter.

Figure 9.7: Time series of the overtake scenario.

such that going back to the original path following was not tested.

The path following errors for the scenario are plotted in Figure 9.8a. The maximum error in the time series is much smaller since the USVs did not get to exit collision avoidance mode. The cross-track error has some low-frequency oscillations around zero, which is also visible in the plots in Figure 9.7. The oscillations could be smaller by increasing ν in the lookahead distance expression. Regarding the formation distances in Figure 9.8b, the steps in the along-track and cross-track distances are much smaller than before because of the smaller constant avoidance angle than before.

The distance plot is less interesting in this scenario since it was cancelled midway, but is shown for completeness in Figure 9.9.

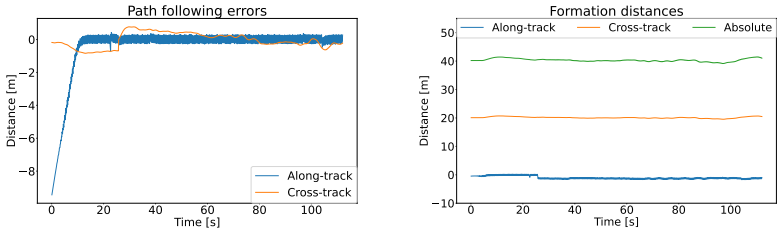

(a) Path following errors.

(b) Formation distances.

Figure 9.8: NSB performace for the overtake scenario.

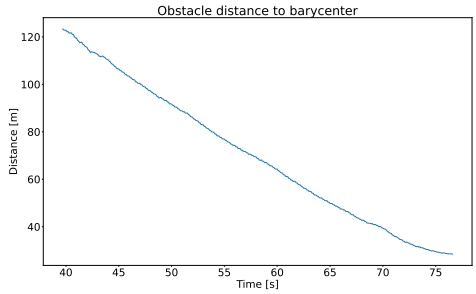

Figure 9.9: Distance from obstacle to barycenter for the overtake scenario.

Chapter 10

Conclusions and future work

In this thesis, COLREGs compliant collision avoidance for two unmanned underactuated surface vehicles with maneuvering limitations has been studied. A literature study of various collision avoidance methods was performed before dynamic models of the vehicles, water jets and obstacles were presented. Then, heading, yaw rate and surge controllers were implemented for controlling the vehicles individually for giving appropriate acutation demands.

The constant avoidance angle method based on the work of Wiig et al. (2020) was chosen and extended to include COLREGs compliance, hysteresis and minimum obstacle distance considerations. This was integrated into the null-space-based behavioral control scheme by incorporating it into a path following task, which was run together with inter-vessel collision avoidance and formation driving. This approach ensured that the UGES, USGES and UGAS properties found in Eek et al. (2020) of the task errors persisted from the formation and path following tasks. When entering the collision avoidance mode, the path was updated to follow the constant avoidance angle instead of the predefined waypoint generated trajectory. Two different approaches were suggested for updating the path. The first approach updated the path parameter continuously through the collision avoidance maneuver such that it could return to the waypoint based path once the obstacle encounter was over. The second approach

ensured a continuous path in all points by making a straight path to the next waypoint from the current path coordinates when the collision avoidance was over. To account for maneuvering limitations, a fixed-radius inscribed circles approach was suggested to ensure a smooth path for the second path update suggestion.

A mathematical analysis of the constant avoidance angle with our dynamic vessel was performed, where collision avoidance could be guaranteed given that the switching distance to the collision avoidance mode was kept above a certain threshold. This guarantee was first shown for one vessel, before it was extended to hold for two vessels in formation, given an upper bound on the task error perturbations.

The simulation study showed that the USVs followed the expected behavior in all our selected COLREGs scenarios and maintained a safe distance to the dynamic obstacle. The tuning of the safety angle in the minimum distance space was also validated for one of the scenarios with a small discrepancy between the real and expected minimum distance to the obstacle. The fixed-radius inscribed circle ensured small path following errors and a prevented steps in the formation errors in turning maneuvers. The approach accounted well for the maneuvering limitations of mine sweep tasks, where a large turning radius is required. The approach also had the advantage of tuning flexibility for the turning radius.

Real-world collision avoidance experiments were performed, where the first suggestion of the trajectory generation in collision avoidance mode was used. All our selected COLREGs scenarios were tested, with the stand-on with critical mode as an exception for safety reasons. The USVs obeyed COLREGs and the give-way and head-on scenarios were considered successes. The overtaking scenario ended up being to close due to a sign error which was fixed ahead of the final simulations.

10.1 Future work

A first suggestion to future work would be to repeat the experiments with the inscribed circles trajectory generation in the heading reference transitions to compare the two suggestions for path updates. Moreover, the overtake should be repeated since it was considered a failed run because of the sign error for relative velocity compensation.

Also, experiments with the second path update suggestion with inscribed circles algorithm could be performed. Finally, functionality validation of the control scheme with mine sweeps could be done in experiments.

Furthermore, a more detailed implementation with analysis could be performed for the multiple obstacle scenario. Since the project concerns COLREGs compliance, edge case handling would be needed for the cases when obstacles are in scenarios of conflicting expected behavior from the vehicle.

The mathematical analysis in this thesis was restricted to one vehicle only. A natural next step would be to extend the analysis to concern two vessels in the NSB scheme. Here, an upper bound for the NSB task erros could be derived before following along the lines of the analysis for one USV. Lemma 7.1 can trivially be extended to concern the barycenter, and 7.4 can be extended with the upper bounds on the task errors.

In the project, the water jet model was linked together, leaving the vessels underactuated. Also, the reverse buckets were kept fully raised at all times. Hence, we were not leveraging the flexibility of the water jets. Usage of some of the water jets capabilities could be explored in more detail. Also, a more complex curve fitting algorithm could have been used to obtain improved model accuracy. Also, forces from wind, waves and currents were not considered. This could be included, and hence the controllers could be more advanced. Here, adaptive controllers and sliding mode could be studied.

According to the analysis in Eek et al. (2020), the lookahead term does not necessarily have to be dependent on the cross-track-error, and other choices of lookahead distance may lead to faster convergence. As a suggestion, a path curvature dependent lookahead distance could reduce the path following errors during turns, by decreasing the lookahead distance during turns for a more aggressive tracking in the cross-track direction.

Finally, different collision avoidance integration methods could be explored. We integrated it into the barycenter path following task, but a thorough analysis could be performed of integrating the collision avoidance into the control scheme as a dedicated task. As explained in Chapter 6, this should not break the existing formation and path following task stability and task error convergence. Other collision avoidance methods

could also be investigated, where a comparative analysis could be performed.

Appendix A

Numerical USV model values

Numerical values of the parameters in the displacement model of Odin and Frigg, provided by FFI:

Parameters	Values	Parameters	Values
m	4900.14	Y_{r_b}	0.0
I_z	20928.0	N_{v_b}	0.0
$X_{\dot{u_b}}$	0.0	N_{r_b}	1281.0
$Y_{\dot{v_b}}$	0.0	$X_{\|u_b\|u_b}$	-143.0
$Y_{\dot{r_b}}$	0.0	$Y_{\|v_b\|v_b}$	-4000.0
$N_{\dot{v_b}}$	0.0	$N_{\|r_b\|r_b}$	-100000.44
$N_{\dot{r_b}}$	0.0	$X_{u_b u_b u_b}$	0.0
X_{u_b}	-50.0	$Y_{v_b v_b v_b}$	0.0
Y_{v_b}	-2000.0	$N_{r_b r_b r_b}$	0.0

$l_{x,starboard} = l_{x,port} = -3.82m$
$l_{y,starboard} = -l_{y,port} = 0.475m$
The numerical values of a_0, a_1, a_2, b_0, b_1 and b_2 are not given on request by FFI.

References

Ames, A. D., Coogan, S., Egerstedt, M., Notomista, G., Sreenath, K. and Tabuada, P. (2019). Control barrier functions: Theory and applications, *2019 18th European Control Conference (ECC)*, pp. 3420–3431.

Antonelli, G., Arrichiello, F. and Chiaverini, S. (2008). Stability analysis for the null-space-based behavioral control for multi-robot systems, *2008 47th IEEE Conference on Decision and Control*, pp. 2463–2468.

Arrichiello, F., Chiaverini, S. and Fossen, T. I. (2006). Formation control of underactuated surface vessels using the null-space-based behavioral control, *2006 IEEE/RSJ International Conference on Intelligent Robots and Systems*, pp. 5942–5947.

Belleter, D., Maghenem, M. A., Paliotta, C. and Pettersen, K. Y. (2019). Observer based path following for underactuated marine vessels in the presence of ocean currents: A global approach, *Automatica* **100**: 123–134.
URL: *https://www.sciencedirect.com/science/article/pii/S0005109818305405*

Chakravarthy, A. and Ghose, D. (1998). Obstacle avoidance in a dynamic environment: a collision cone approach, *IEEE Transactions on Systems, Man, and Cybernetics - Part A: Systems and Humans* **28**(5): 562–574.

Chiaverini, S. (1997). Singularity-robust task-priority redundancy resolution for real-time kinematic control of robot manipulators, *IEEE Transactions on Robotics and Automation* **13**(3): 398–410.

Cockcroft, A. N. and Lameijer, J. N. F. (2011). *A Guide to the Collision Avoidance Rules*, Elsevier Butterworth Heinemann.

Eek, A., Pettersen, K. Y., Ruud, E. L. M. and Krogstad, T. R. (2020). Formation path following control of underactuated usvs – with proofs.
URL: *https://arxiv.org/abs/2011.05021*

Eriksen, B.-O. H., Breivik, M., Pettersen, K. Y. and Wiig, M. S. (2016). A modified dynamic window algorithm for horizontal collision avoidance for auvs, *2016 IEEE Conference on Control Applications (CCA)*, pp. 499–506.

Eriksen, B.-O. H., Breivik, M., Wilthil, E. F., Flåten, A. L. and Brekke, E. F. (2019). The branching-course model predictive control algorithm for maritime collision avoidance, *Journal of Field Robotics* **36**(7): 1222–1249.
URL: *https://onlinelibrary.wiley.com/doi/abs/10.1002/rob.21900*

FFI (2020).
URL: *https://www.ffi.no/aktuelt/nyheter/forsvaret-tester-nytt-norsk-minesveip*

Fiorini, P. and Shiller, Z. (1998). Motion planning in dynamic environments using velocity obstacles, *The International Journal of Robotics Research* **17**(7): 760–772.
URL: *https://doi.org/10.1177/027836499801700706*

Forsvarsmateriell (2017).
URL: *https://www.fma.no/aktuelt-og-media/2017/ubemannet-fremtid-for-sjoforsvaret*

Fossen, T. I. (2011). *Handbook of Marine Craft Hydrodynamics and Motion Control*, John Wiley & Sons, Ltd.

Fox, D., Burgard, W. and Thrun, S. (1997). The dynamic window approach to collision avoidance, *IEEE Robotics Automation Magazine* **4**(1): 23–33.

Haraldsen, A., Wiig, M. S. and Pettersen, K. Y. (2021). Reactive collision avoidance for underactuated surface vehicles using the collision cone concept, *2021 IEEE Conference on Control Technology and Applications (CCTA)*, pp. 619–626.

ICRC (2016).
URL: *https://ihl-databases.icrc.org/ihl/full/GCI-commentary*

Johansen, T. A., Perez, T. and Cristofaro, A. (2016). Ship collision avoidance and colregs compliance using simulation-based control behavior selection with predictive hazard assessment, *IEEE Transactions on Intelligent Transportation Systems* **17**(12): 3407–3422.

Khalil, H. K. (2013). *Nonlinear Systems*, Pearson Education Limited.

Khatib, O. (1986). Real-time obstacle avoidance for manipulators and mobile robots, *The International Journal of Robotics Research* **5**(1): 90–98.
URL: *https://doi.org/10.1177/027836498600500106*

Kuwata, Y., Wolf, M. T., Zarzhitsky, D. and Huntsberger, T. L. (2011). Safe maritime navigation with colregs using velocity obstacles, *2011 IEEE/RSJ International Conference on Intelligent Robots and Systems*, pp. 4728–4734.

Matouš, J., Pettersen, K. Y. and Paliotta, C. (2021). Formation path following control of underactuated auvs – with proofs.
URL: *https://arxiv.org/abs/2111.03455*

Matouš, J., Pettersen, K. Y., Varagnolo, D. and Paliotta, C. (2023). Singularity-free formation path following of underactuated auvs: Extended version.

Midtgaard, Øivind and Nakjem, Morten (2016). Unmanned systems for stand-off underwater minehunting, pp. 1–8.

Naval News Staff (2021).
URL: *https://www.navalnews.com/naval-news/2021/04/patria-to-deliver-acoustic-minesweeping-systems-to-royal-norwegian-navy*

Pettersen, K. Y. (2017). Lyapunov sufficient conditions for uniform semiglobal exponential stability, *Automatica* **78**: 97–102.
URL: *https://www.sciencedirect.com/science/article/pii/S0005109816304964*

Royal Navy (2021).
URL: *https://www.royalnavy.mod.uk/news-and-latest-activity/news/2021/january/29/210129-autonomous-minesweeper*

Singletary, A., Klingebiel, K., Bourne, J., Browning, A., Tokumaru, P. and Ames, A. (2020). Comparative analysis of control barrier functions and artificial potential fields for obstacle avoidance.
URL: *https://arxiv.org/abs/2010.09819*

Thyri, E. H., Basso, E. A., Breivik, M., Pettersen, K. Y., Skjetne, R. and Lekkas, A. M. (2020). Reactive collision avoidance for asvs based on control barrier functions, *2020 IEEE Conference on Control Technology and Applications (CCTA)*, pp. 380–387.

VG: Einar Otto Stangvik, Oda Leraan Skjetne, Tom Byermoen, Endre Alsaker-Nøstdahl, Harald Vikøyr (2022).
URL: *https://www.vg.no/spesial/2018/helge-ingstad-ulykken/*

Wiig, M. S., Pettersen, K. Y. and Krogstad, T. R. (2020). Collision avoidance for underactuated marine vehicles using the constant avoidance angle algorithm, *IEEE Transactions on Control Systems Technology* **28**(3): 951–966.